ACTIVE CONTROL OF SEPARATION INDUCED DISTORTION IN A SCALED TACTICAL AIRCRAFT INLET

by

ZACHARY WARFIELD

B.S. Mechanical Engineering
University of Notre Dame, 1998

Submitted to the Department of Aeronautics and Astronautics
in partial fulfillment of the requirements for the degree of

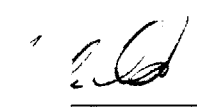## MASTER OF SCIENCE IN AERONAUTICS AND ASTRONAUTICS

at the

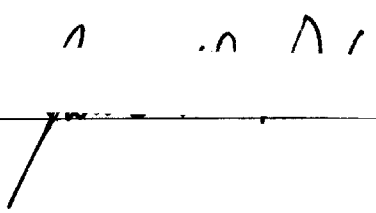## MASSACHUSETTS INSTITUTE OF TECHNOLOGY

September 2001

© Zachary Warfield, 2001. All rights reserved.

The author hereby grants to MIT the permission to reproduce
and to distribute publicly paper and electronic
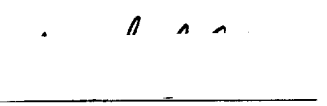copies of this thesis document in whole or in part

Author: _____
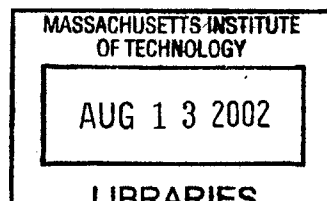
Zachary Warfield
Department of Aeronautics and Astronautics
July 24, 2001

Certified by: _____

Dr. James Paduano
Principal Researcher
Thesis Supervisor

Accepted by: _____

Wallace E. Vander Velde
Professor of Aeronautics and Astronautics
Chair, Committee on Graduate Students

1

ACTIVE CONTROL OF SEPARATION INDUCED DISTORTION IN A SCALED TACTICAL AIRCRAFT INLET

by

Zachary Warfield

Submitted to the Department of Aeronautics and Astronautics
on July 24, 2001 in Partial Fulfillment of the
Requirements for the Degree of Master of Science in
Aeronautics and Astronautics

ABSTRACT

A one-sixth-scale tactical aircraft inlet was outfitted with actuators and sensors to study active control of inlet separation. The inlet duct was serpentine shaped, which introduces adverse pressure gradients that cause separation. The separated flow induces distortion (non-axisymmetric total pressure profiles) with significant steady and unsteady components. Actuation consisted of four injector-valve assemblies, located downstream of the inlet, capable of modulating airflow in a *50-500 Hz* bandwidth. Sensing consisted of steady and unsteady total pressure transducers at the aerodynamic interface plane (AIP) and hot-film heat flux sensors at the separation point in the inlet.

The first set of experiments focused on characterizing the flow within the inlet. The experiments included tests to visualize the steady component of inlet flow using oil-film surface visualization techniques, test to determine the steady-state pressure recovery profile at the AIP, and tests to correlate unsteady measurements between the separation point and AIP. Flow visualization results illustrate that the separated region in the inlet behaves like a textbook "owl-face" separation. An adverse pressure gradient causes flow reversal and subsequently vortices shed from the separation point. Pressure recovery data indicates that a large total pressure deficit exists in the upper quadrant of the AIP. This deficit is associated with losses in the separated flow. Correlation analyses between the separation point and the AIP sensors indicate a strong coherence between unsteadiness at these locations. Based on the results of these analyses, it appears that the separation point vortices shed in an alternating (left-right) pattern and are the source of AIP distortion.

To reduce flow unsteadiness at the separation point and the AIP, a series of narrow-bandwidth feedback control experiments were performed. These experiments involved measuring unsteady quantities at the separation point and AIP, passing these signals through a resonator filter to generate a command signal for the actuators, and applying actuation to the system via the downstream injectors. The results of these experiments indicate that feedback control is successful at locally canceling the measured quantity via superposition of acoustic waves at the feedback sensor location. It is also of interest to study the effect of feedback control on vortex shedding unsteadiness, and on the propagation of these vortices through the inlet. However, results to date have not shown that narrow band feedback couples to these dynamics in a beneficial way.

Thesis Supervisor: Dr. James Paduano
Title: Principle Researcher

ACKNOWLEDGEMENTS

First and foremost, I would like to acknowledge Dr. Jim Paduano for giving me the opportunity to participate in this research project. Aside from offering his technical expertise, I am in debt to Dr. Paduano for helping me focus on my research, thus making the timely completion of this thesis possible. I am also thankful to Prof. Ian Waitz for giving me much needed guidance during my first months at MIT. I am very thankful to Northrop Grumman and NASA Glenn for providing the UCAV inlet, instrumentation, and actuators necessary to perform my series of experiments.

Thanks to my family (my Mom and Paul, my Dad and Cindy, Grandma, Justin, Hannah, Aunt Pat and Uncle Harry, Aunt Cookie and Uncle Eddie, Sean and Heather, Duffy and Nissa, Eric and Susan, Kyle and Bridget, Harry, Sarah, Kylea, Khloe and Andrew) for always supporting me. I wish I could have made it home to Frederick more often, but MIT was a time consuming endeavor.

Many thanks to Dr. Gerald Guenette for sharing his technical and experimental experience by answering every question that came to my mind. Thanks to Michael Brear for lending his expertise to our research and for convincing me to take a few weeks off when (if) I graduate. Thanks to Jimmy Letendre and Jack Costa for teaching me how to weld, solder, plumb, and every other skill that was needed to get our rig running. Thanks to Victor Dubrowski for sharing his insightful philosophies along with his machining tips. Thanks to Prof. Epstein and Bill Ames for letting us run the De-Laval, even though it disturbed everyone in the building. Thanks to Lori Martinez for always letting me know when there were leftovers, and for not yelling at me when I kept asking for keys.

Thanks to all my peers at the GTL for making the work/research environment so enjoyable. I wish I could stick around to finish the summer softball season with Shuler, Dan ("Captain"), Spad, CP, Raff-dog, and the rest, but I am sure they will pick up a better player in free agency. Special thanks to the BDT team of Bret, Jameel, and Will for lending me tools and advice during the months we co-existed in the BDT experiment area. Thanks to my officemates Taek, Simon and Laurent for sharing in the thesis writing pains during our waning months together. Thanks to Steve Braddom for building the heat flux sensors, understanding the data acquisition system, and explaining to me how the military really works. Thank you Jeremy and Dave for showing me the ropes at MIT and for not laughing when I went on my philosophical/political rants. I would also like to thank my future wife for not meeting me at MIT... I don't think I would have graduated on time if you did.

Thanks to the good people at Nick's Roast Beef in Davis Square for supplying at least 50% of my diet in the form of their cheeseburger subs. Thanks also to Kateri Lafond for baking me cookies and providing me with invaluable fashion tips. Lastly, I must thank my roommates Jon Steele, Timm Fair and Alex Bruni (A-Rod) for convincing me to move to Boston and giving me a place to live. It may not have been like it was at ND, but I enjoyed every minute of my time at 72 Baystate Av., Apt. #2. Hey Timm, you know what...?

TABLE OF CONTENTS

LIST OF TABLES

LIST OF FIGURES

13

14

NOMENCLATURE

ACRONYMS:

MAFC	Micro Adaptive Flow Control
MIT	Massachusetts Institute of Technology
GTL	Gas Turbine Laboratory
NASA	National Aeronautics and Space Administration
DARPA	Defense Advanced Research Programs Administration
UCAV	Uninhabited Combat Air Vehicle
RMS	Root Mean Square
AIP	Aerodynamic Interface Plane
PR	Pressure Recovery
MIMO	Multiple Input Multiple Output
SISO	Single Input Single Output
IC	Instrument Can
SDIU	Scan-valve Digital Interface Unit
MFF	Mass Flow Factor
CFD	Computational Fluid Dynamics
PSD	Power Spectral Density

ROMAN:

L	Length
M	Mach number
$\dot{m}$	Mass flow rate
P	Pressure
R	Universal Gas Constant
A	Area; Magnitude Bulk Parameter
T	Temperature, Transmission Matrix
a	Speed of Sound
V	Velocity
u	Time average x component of velocity
R	Universal Gas Constant
Z	Impedance

GREEK:

ψ, Ψ	Non-dimensional Pressure
ϕ, Φ	Non-dimensional Velocity
γ	Ratio of specific heats
ρ	Density
Λ	Location Bulk Parameter
Θ	Extent Bulk Parameter
τ	Time Delay
θ	Angular Distance
ω	Angular Velocity
δ	Perturbation Operator

SUBSCRIPTS:

A	Axial
out	Exit condition
in	Inlet condition
S	Static
∞	Ambient
T	Total
Act	Actuator Duct
BM	Bell-mouth
Diff	Diffuser
SR	Sensor Ring
IC	Instrument Can
Plug	Throttle Plug
AD	Acoustic Duct
Thrt	Throttle
LP	Lumped Plenum
Comp	Compressor
REF	Reference
I	Injection
BP	Bulk Parameter
HF	Hot-film

1 INTRODUCTION

1.1 BACKGROUND AND MOTIVATION

The propulsive systems of most tactical military aircraft include some form of inlet to condition the airflow before it reaches the compressor. The purpose of the inlet is to ensure that the airflow delivered to the compressor is adequate for successful compressor operation. This relationship between inlet flow and the compression system is outlined in AIR-1419: Inlet Total-Pressure-Distortion Considerations for Gas-Turbine Engines [21] and ARP-1420: Gas Turbine Engine Inlet Flow Distortion Guidelines [12]. These documents discuss acceptable levels of distortion delivered by inlets and the effect of this inlet distortion on compressor performance.

The overall purpose of this thesis is to study and control the behavior of distortion unsteadiness in a tactical aircraft inlet. The research that constitutes this thesis describes a portion of a joint research project between the Massachusetts Institute of Technology (MIT), Caltech, NASA Glenn and Northrop Grumman. The aircraft inlet that serves as the test section for this project is part of a Northrop Grumman uninhabited combat air vehicle (UCAV) prototype. Due to certain design requirements such as radar signature, UCAV performance depends heavily on the inlet design. The radar signature requirement implies that these aircraft must be able to fly without detection from radar. Therefore, the compressor blades must not be visible (via radar) from the exterior of the vehicle. This requirement leads to the curved (S-shaped) inlet design shown in Figure 2.3. The bi-product of a curved inlet is potentially poor flow properties at the Aerodynamic Interface Plane (AIP) or increased inlet length. In order to curve the flow without causing loss of pressure recovery, the inlet must be relatively long. Conversely, if inlet length is decreased then the flow properties suffer. Therefore, inlet length and the quality of the inlet flow are traded when designing these types of inlets.

The length of the propulsion system in the UAV often dictates its size and consequently the mass of the vehicle. Therefore, a reduction in inlet length results in either increased payload capacity or

increased fuel efficiency. Similarly, an improvement in the flow properties (pressure recovery and unsteadiness) at the AIP increases the propulsive efficiency of the system. Improved propulsive efficiency leads to higher vehicle thrust or better maneuverability. Additionally, reduction of distortion at the compressor face may lead to lower stall margins, thus improving the designed capabilities of the propulsion system. As mentioned earlier reduction of inlet length and the quality of the flow properties are inversely related. Therefore, realizing the performance benefits associated with both of these improvements requires an enabling technology. This project attempts to improve both pressure recovery and steady and unsteady distortion caused by the short, curved inlet geometry. The approach used to improve these conditions will be to apply active flow control at both the compressor face and the separation point.

1.2   PRIOR RESEARCH IN ACTIVE FLOW CONTROL

The flow structure in the UCAV inlet consists of a region of separated flow caused by the inlet's curved profile. The energy losses associated with boundary layer separation account for the poor flow properties at the AIP. Mohamad Gad-el-Hak's 1991 article titled "Separation Control: Review" [27] gives a comprehensive description of flow separation and previous techniques for control. This article identifies that both steady and unsteady separation exists in three-dimensional flows such as the UCAV inlet. Gad-el-Hak's article presents a review of the methods used to control the steady separation. These methods include shaping the inlet geometry to eliminate adverse pressure gradients and changing the velocity profile at the wall by withdrawing near wall fluid through slots or by wall heat transfer. These methods are classified as steady because the mechanism used to control the separation is constant. More recently, a joint venture by Lockheed Martin and NASA Glenn involved research into new methods of steady separation control. In a paper presented at the 22nd International Congress of the Aeronautical Sciences [26], a technique using 36 co-rotating microvane vortex generators is shown to have positive effects on the pressure recovery and spatial distortion. These results demonstrate the effectiveness of suppressing *steady* separation via *steady* control in high Mach number flows ($M = 0.60$).

In addition to the work by Lockheed Martin and NASA Glenn, research has been performed to control *steady* separation via *unsteady* control. This research, performed at the United Technologies Research Center, uses "directed synthetic jets" [28] located at the separation point. These jets periodically excite the leading edge of separation using oscillating slot flow. In McCormick's article

[28] it was shown that directed synthetic jets can fully suppress steady separation of subsonic flows ($M = 0.05$).

The overall goal of this research project is to eliminate or reduce *both* the *steady* and *unsteady* effects of separation in the UCAV inlet. The experiments mentioned above describe methods for controlling *steady* separation, however, very few results are known pertaining to the control of unsteady separation. In fact, a study by Kwong and Dowling [23] concluded that steady injection could cause unsteady oscillations in the flow to become larger. This research attempts to examine methods for controlling unsteady separation, while at the same time reducing steady separation. The mechanism proposed to mitigate unsteady separation is an actuation system located at the compressor face. Prior research at MIT uses compressor face actuation to stabilize and control rotating stall [5,6,10]. However, the potential effect of such actuation (downstream of the separation point) on separation unsteadiness is unknown. In particular, the physical mechanism by which active control influences the upstream flow field has not been explained. However, research by Cho [25], aimed at reducing inlet distortion using downstream speakers, indicates that it is physically possible to alter inlet flows using global (acoustic) rather than local actuation. Research by Kwong and Dowling [23] support this by showing that feedback control of unsteady blowing successfully reduces unsteadiness in conical and rectangular diffusers.

This thesis focuses on the use of unsteady feedback control to reduce separation unsteadiness in a tactical aircraft inlet. The feedback control techniques in this thesis are similar to those employed by Kwong and Dowling. The main difference is that this research attempts to control separation unsteadiness from downstream of the inlet separation point. Other differences include; the fact that the test section in this research is an industrially designed three-dimensional inlet, the Mach number in the UCAV inlet is high ($M \sim 0.60$), and the frequency bandwidth of the unsteadiness is high (200-$500\ Hz$).

1.3   RESEARCH OBJECTIVES

The objective of this research is to determine if flow control using actuators at the compressor face can improve the flow properties of a UCAV inlet. More specifically, the goal is to experimentally determine if the introduction of planar acoustic waves downstream of the inlet can be used to reduce unsteadiness caused by flow separation. Both open loop and closed loop means of actuation are

tested. However, the main focus is on feedback control approaches. Given this goal, this thesis concentrates on two areas of research: characterizing inlet unsteadiness and feedback control experiments designed to suppress this unsteadiness.

1.4 THESIS OVERVIEW

The remainder of this thesis focuses on four topics: MIT's experimental setup, acoustic modeling of the UCAV inlet test section, characterization of the flow in the test section, and active control of flow unsteadiness. Since this research is experimentally based, Chapter 2 provides a detailed description of the experimental setup used to test flow control in the Northrop Grumman UCAV. Chapter 3 addresses the acoustic modeling of the inlet test section. The 1-D acoustic model developed in this chapter is used to gain understanding of the acoustics in the test section. Switching back to the experiments, Chapter 4 discusses the series of experiments performed to characterize the flow properties in the UCAV inlet. This chapter includes flow visualization of the separated region, characterization of the separation unsteadiness, development of bulk parameters to quantify unsteadiness at the AIP, and the experimental construction of transfer functions between the actuators and sensors. Chapter 5 concentrates on feedback control of unsteadiness in the inlet from downstream actuators. This chapter includes experimental results from simplified control laws, as well as a theoretical development of more complex control systems. Finally Chapter 6 provides a summary of the experimental results and conclusions.

2 EXPERIMENTAL SETUP

This thesis focuses on a series of active control experiments performed on the unsteady flow in a UCAV inlet. The experimental setup, located at the MIT Gas Turbine Laboratory (GTL), consists of various subsystems. The test section, shown in Figure 2.1, is a combination of components from Northrop Grumman and NASA Glenn, as well as parts designed and fabricated at MIT. The test section consists of a bellmouth, a one-sixth-scale Northrop Grumman UCAV inlet diffuser, an instrument can (IC), an actuator duct, a throttle plug, and when needed a sensor ring (not shown in Figure 2.1). Aside from the test section, the experimental setup consists of various subsystems to support the active flow experiments. These subsystems include the De-Laval internal airflow system, amplifiers, the control law hardware system, air supply plumbing, power supplies, and signal processing instrumentation. Although all of these subsystems are crucial to the experiments, this chapter focuses only on the test section components and the data acquisition systems. Other elements of the experiment are briefly reviewed here and are discussed in more detail in Appendix A.

To perform high Mach number experiments ($M \sim 0.65$) on the scaled UCAV inlet, a downstream suction source must pull air through the inlet at rates in the range of 2.5-3.7 lb/s. The turbomachinery used to create this suction supply is the De-Laval compressor located in the basement of the GTL. The flow path is an open loop system; air is drawn into the UCAV inlet via the bell-mouth, flows through the De-Laval compressor, and is expelled through an exhaust pipe located on the roof of the GTL. Section A.3 contains a detailed description on how to operate the De-Laval turbomachinery and the operating conditions for this series of experiments.
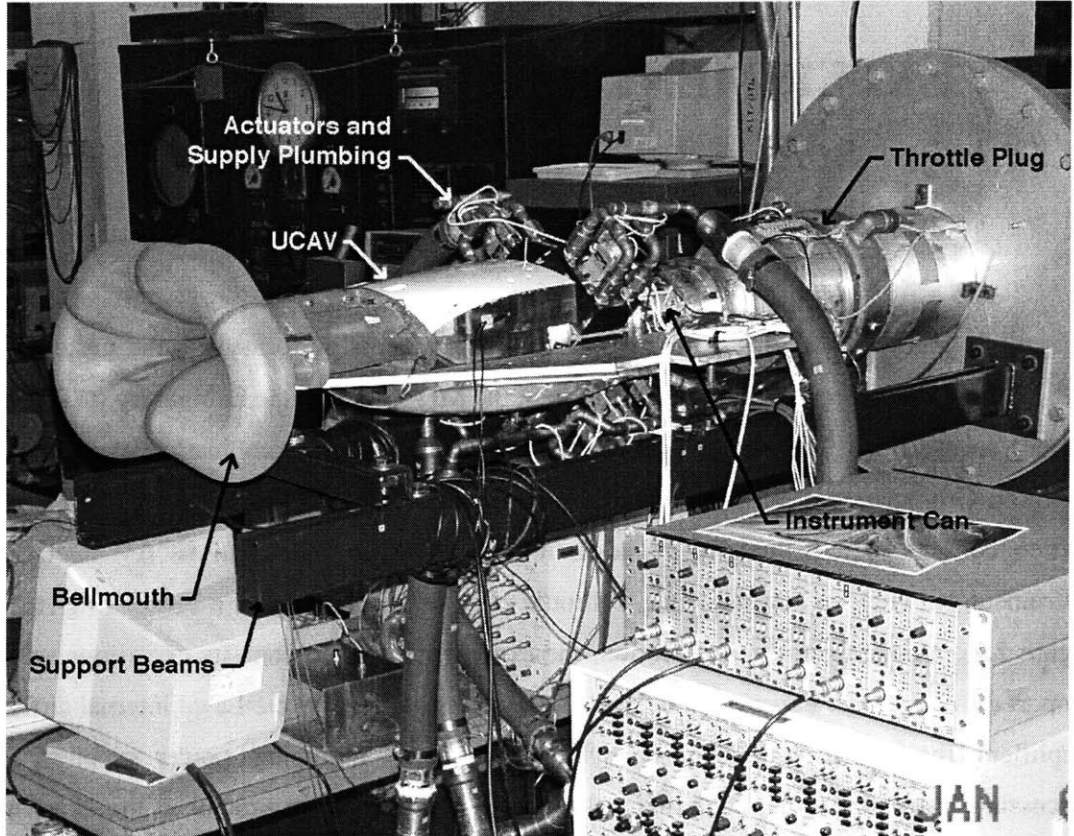
Figure 2.1 – Experimental Test Section

Due to the high cost and fragility of the test section components, the method used to mount the test section to the De-Laval ducting determined the overall layout (see Figure 2.1). A throttle plug attaches to a suction supply duct via an adapter plate designed specifically for this experimental setup. Two cantilevered beams bolted to this adapter plate support the throttle plug, the UCAV wing-plate and the interface between the actuator duct and instrument can. This support structure configuration isolates the experimental setup from the ground, thus minimizing shear and bending stresses at the component interfaces. The cantilevered support also allows for easy access to all of the components within the test section. This feature proved to be very valuable during configuration changes and when plumbing the actuator air supply.

Depending on the purpose of the experiment being performed, the configuration of the sensor ring, actuator duct and IC may vary within the test section. For example, the experiments performed to characterize the AIP unsteady total pressure used the unsteady IC as the AIP measurement source, while feedback flow control experiments require the use of the sensor ring in place of the IC. Figure

2.2 shows the configuration used for the unsteady flow characterization experiments. Table 2.1 lists the configurations used for the various experiments.

Component Configuration	Experiment Description	Dates
Bellmouth, Diffuser, Steady IC, Throttle Plug	Measurement of the steady pressure profile at the AIP.	11/9/00 – 11/21/00
Bellmouth, Diffuser, Steady IC, Throttle Plug	1st Flow Visualization Experiment	11/27/00
Bellmouth, Diffuser, Sensor Ring, Steady IC, Throttle Plug	Unsteady flow characterization using sensor ring (static and total pressure).	11/30/00 – 12/22/00
Bellmouth, Diffuser, Sensor Ring, Actuator Duct, Steady IC, Throttle Plug	Test effects of constant actuation on AIP pressure recovery. Measure unsteady response at AIP using sensor ring (total and static pressure).	1/9/01 – 2/12/01
Bellmouth, Diffuser, Sensor Ring*, Actuator Duct*, Throttle Plug	2nd Flow Visualization Experiment. Starred (*) components used to replace displaced length of IC.	3/8/01 – 3/12/01
Bell-mouth, Diffuser, Unsteady IC, Actuator Duct, Throttle Plug	Unsteady flow characterization using unsteady instrument can. These experiments include unsteady AIP movies and building of transfer functions.	3/23/01 – 5/24/01
Bell-mouth, Diffuser, Sensor Ring, Actuator Duct, Throttle Plug	Feedback Control Experiments	6/27/01 – 7/17/01

Table 2.1 - Experiment Phase Description and Timeline

27
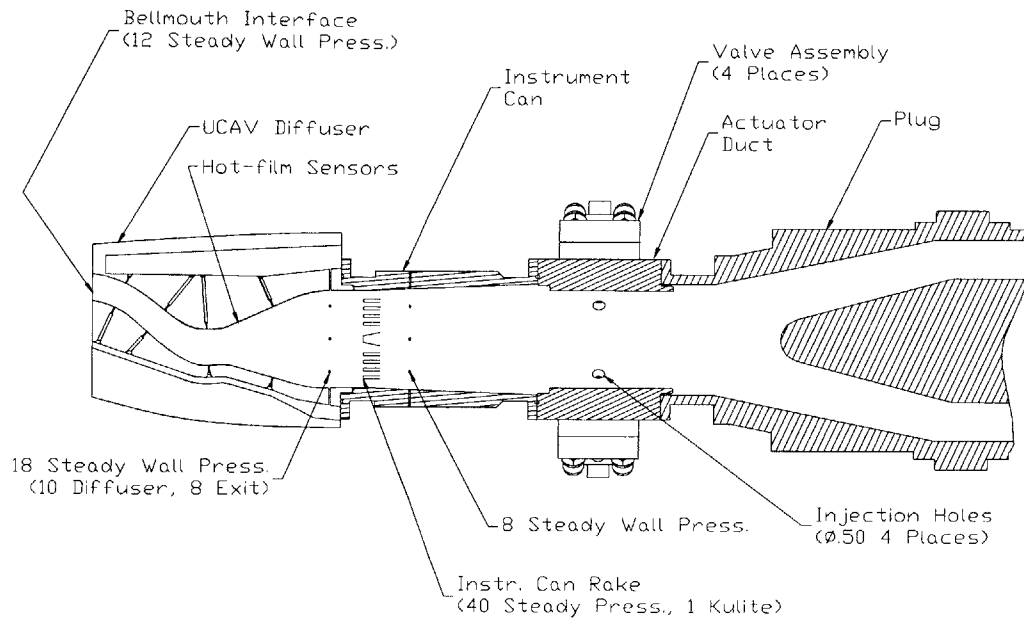
Figure 2.2 – Typical Configuration of the Test Section (Sensor Ring not shown)

The following sections describe the components that constitute the experimental test section. This chapter also discusses the systems used to acquire data and monitor the operation of the experimental setup. Lastly, this chapter describes the various calibrations required to set the experimental conditions and record data.

2.1 UCAV DIFFUSER

The tactical aircraft inlet used in the active flow control experiments at MIT is the inlet from a Northrop Grumman UCAV prototype, shown in Figure 2.3. This inlet, chosen because of the potential benefits that flow control technology offers, is S-shaped with a length to diameter ratio of approximately 2.6. The inlet is part of a one-sixth-scale wind tunnel model of an entire UCAV vehicle fabricated out of epoxy resin via stereo-lithography. Along with the UCAV vehicle, Northrop Grumman also furnished MIT with an epoxy resin bellmouth. The bellmouth is used to simulate flow into the inlet diffuser during cruise conditions. The UCAV inlet is equipped with eighteen static wall pressure taps; eight evenly spaced circumferentially at the AIP, six along the axial centerline of the inlet and two taps on each side of the inlet. The bellmouth, shown in Figure 2.1, is equipped with ten static wall pressure taps located around the exit of the bell-shaped section. These taps prove useful in calibrating the bellmouth mass flow, described in Section 2.6.2.

28

The UCAV supplied to MIT contains the first generation of inlet designs for Northrop's UCAV vehicle. The geometry of the inlet is not optimal for AIP pressure recovery. In fact, later versions of the Northrop UCAV design demonstrate improved pressure recovery properties compared to this inlet. However, the non-optimal design is a better test subject to demonstrate the benefits of active flow control because of its poor flow characteristics.
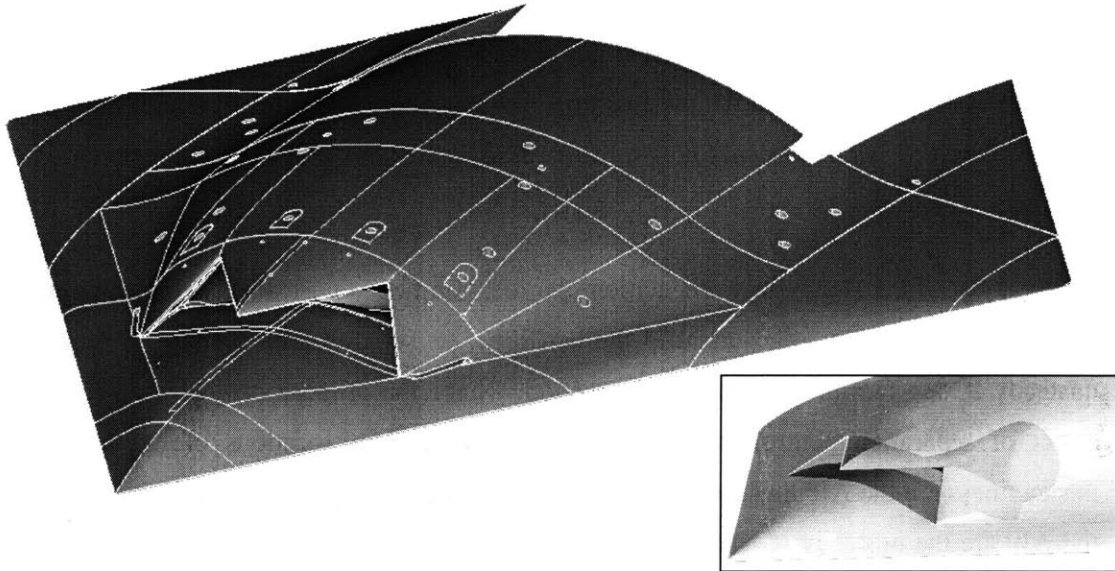
Figure 2.3 – Pro/E Rendering of Northrop Grumman UCAV

2.2 INSTRUMENTATION

The instrumentation used in the UCAV inlet experiments can be classified into two categories, instrumentation for steady measurements and instrumentation for unsteady measurements. The steady instrumentation includes forty total pressure probes located in a steady IC and numerous wall static pressure taps located in the diffuser and bellmouth. The unsteady instrumentation includes hot-film sensors located in the region of flow separation, forty total pressure probes in an unsteady IC[1]

---

[1] Both instrument cans have the same mounting interfaces, so either the steady or unsteady IC can be used during an experiment.

and up to eight pressure probes located in the sensor ring. See Figure 2.2 for the locations of these sensors.

2.2.1   UNSTEADY INSTRUMENTATION

Since this research pertains to high Mach number flows, with high levels of unsteadiness, the instrumentation used to measure the inlet flow must capture time varying perturbations in the flow. Due to the limited bandwidth of the actuators, the characteristic frequencies of interest for this research are less than *1 kHz*. To guarantee accuracy in the measurement and logging of unsteady data, the instrumentation and data acquisition systems were chosen to operate at rates greater than *5 kHz*. Therefore, signal-processing problems associated with aliasing at relevant frequencies are avoided.

Unlike most of the steady instrumentation, the location of the unsteady instrumentation is not fixed within the test section. Placement of the hot-films, sensor ring probes and to a limited degree the unsteady IC are flexible within the test section. Since the purpose of this research is to study the effect of separation control on distortion, the two obvious locations of interest for measuring unsteadiness are the AIP and the separation point. The devices used to measure unsteady pressure at the AIP are the unsteady IC and the sensor ring, while hot-film sensors measure unsteadiness at the separation point. In some configurations, specifically those employing both the IC and the sensor ring, a third location for taking unsteady measurements possible. As previously discussed in Table 2.1, the IC can be used to characterize the unsteady flow while the sensor ring is used for feedback control. Chapters 4 and 5 discuss reasons for each variant of the experimental configuration. The following sections briefly describe each unsteady component.

2.2.1.1   SENSOR RING

The sensor ring provides great flexibility within the test section for measuring unsteady data. The original purpose of the sensor ring was to supplement the unsteady IC by allowing the placement of additional unsteady sensors at various locations in the setup. However, during the course of the experiments the sensor ring became not only a supplement to, but also a substitute for the unsteady IC. The axial length of the sensor ring is short, *1.3 in.*, to minimize its impact on the layout the test section. The reduced length of the sensor ring and lack of mounting flanges (see Figure B.4) enables its placement between any of the components in the test section. Since the sensor ring contains no

mounting flanges, it relies on a compression fit between its two mating components. For instance, in the configuration shown in Figure 2.4, telescoping bolts from the UCAV to the actuator duct flange supply the mating force to support the sensor ring.

The sensor ring features eight evenly spaced, radial probe holes. Each hole is designed to accommodate a *1/8-inch* diameter probe supported by a *1/8"* NPT fitting. The three types of probes used in the sensor ring are total pressure, static pressure and hot-wire. The hot-wire data proved irrelevant for this thesis; therefore no further discussion of the hot-wire setup is necessary. The total and static pressure probes, both fabricated at MIT of *1/8-inch* steel tubing (see Figure B.1), connect to 5-psi unsteady pressure transducers (Kulites). These transducers can accurately measure unsteady total pressure perturbations in a frequency range of up to 10 kHz. The static pressure probes mount flush with the inner duct wall, while the total pressure probes can be manually traversed in the radial direction from the center of the sensor ring to within *1/2-inch* of the duct wall. The sensor ring can also be rotated about its axis of symmetry to accommodate any circumferential configuration of the probes. See Figure 2.4 for a typical sensor ring configuration.

Due to the length of the pressure probes (*3.5 in.* for the total and *2.5 in.* for the static) acoustic modes generated in the probes appear in the *3000-5000 Hz* range. This source of measurement error is acceptable for this research because the frequencies of interest in these experiments are less than *1000 Hz*. However, future research may require higher frequency measurements, in which case the sensor ring will be ineffective.
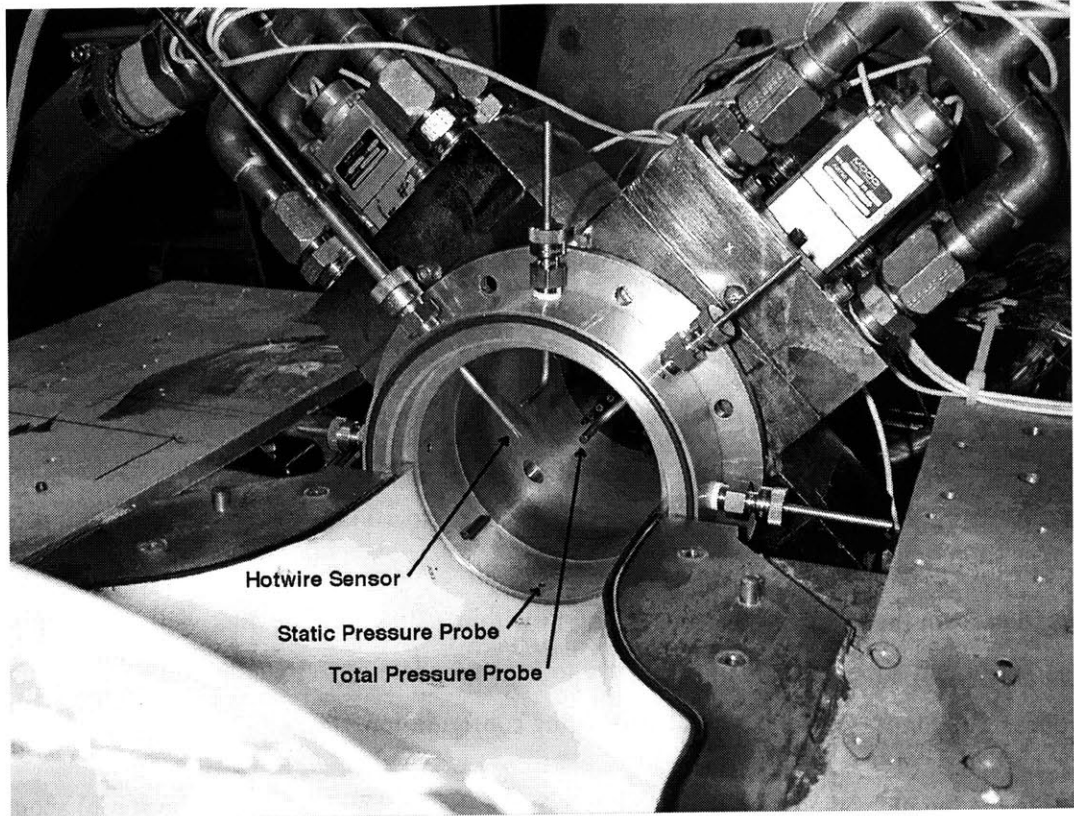
Figure 2.4 – Sensor Ring

2.2.1.2   UNSTEADY INSTRUMENT CAN

In order to measure the pressure at the AIP, Northrop Grumman designed an instrument can containing forty total pressure probes. The layout of the probes within the instrument can, shown in Figure 2.5, complies with Section 7.2.2 of ARP-1420: Gas Turbine Engine Inlet Flow Distortion Guidelines [12]. This layout locates each probe at the centroid of an equal area section of the duct. Therefore, the total pressure recovery at the AIP is simply the average of the measured total pressures at the forty probes, divided by the ambient inlet pressure.
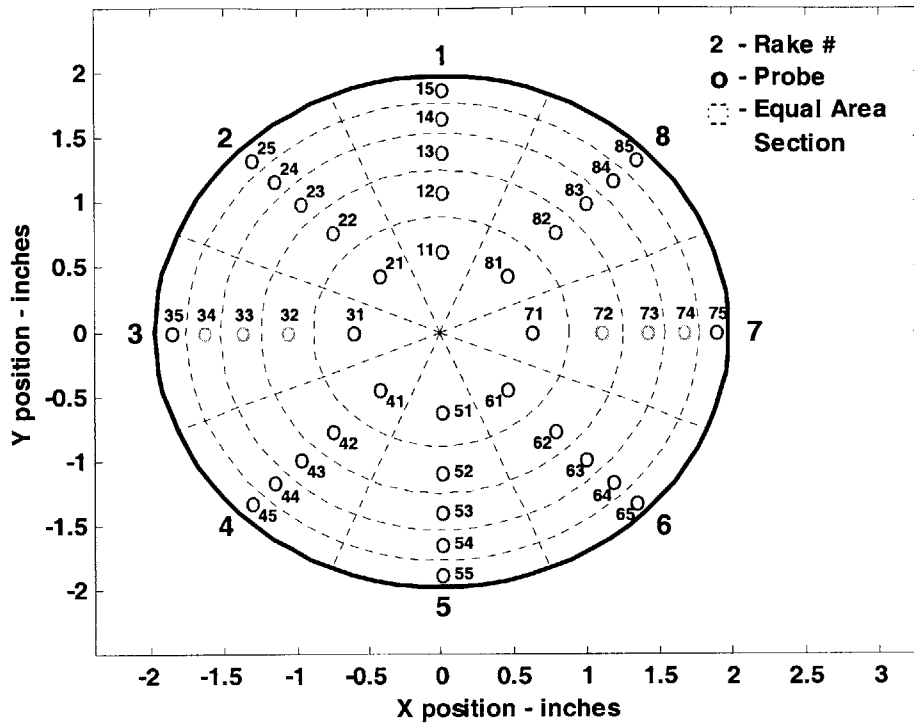
Figure 2.5 – Probe Layout of Instrument Can (View looking into IC)

Northrop Grumman provided MIT with two such instrument cans, the first equipped with steady pressure probes and the second equipped with unsteady probes. The steady IC was used to obtain pressure recovery information under various flow conditions and create color contour maps of the total pressure at the AIP. This information helped validate the experimental setup by comparing MIT experimental results to the Northrop Grumman CFD solutions and experimental data (see Chapter 4). After using the steady IC to validate the experimental setup and its operation[2], Northrop Grumman supplied MIT with the unsteady IC.

The unsteady instrument can is equipped with forty unsteady differential pressure transducers, each with the capability of measuring perturbations up to 10 kHz. The unsteady IC also contains forty

---

[2] During the initial runs of the De-Laval compressor, the threat of surge was considered too high to risk using the more expensive unsteady IC. Once a high level of confidence in the De-Laval turbomachinery and operational sequences was attained, there was no risk in using the unsteady IC.

steady pressure probes that perform the same function as the steady IC. The transducers in the unsteady IC have the capability of measuring D/C pressure levels. However, these transducers display high D/C drift rates during calibration. To eliminate this drift, the signal from the unsteady transducers is A/C coupled by the amplifiers. The steady pressure probes in the unsteady IC are then used to measure the D/C portion of the total pressure. Thus, the total pressure is the combination of the A/C coupled data from the unsteady transducers and the D/C level measured by the steady probes. Figure 2.5 shows the probe layout in the instrument can. One of the transducers in the unsteady IC, probe 23, has a scaling problem in its output. The transient output from this probe is approximately an order of magnitude less than the other probes. Unfortunately, the location of probe 23 makes it important for characterizing the AIP distortion. Therefore, the scaling error must be accounted for in the post-processing of the data by multiplying the output by a scaling factor. The appropriate scaling factor is determined by comparing the RMS values of probe 23 with those of probes 22, 82 and 83[3].

The transducers in the sensor ring and/or the unsteady IC connect to a bank of 2310 Strain Gage Conditioning Amplifiers, made by the Instruments Division of Measurements Group, Inc. These amplifiers perform the dual function of filtering the unsteady data and conditioning the output signal before it is recorded by the data acquisition system. The amplifiers condition the input signal in accordance with the calibration discussed in Section 2.6.3. The calibration of the unsteady transducers involves individually tuning each amplifier gain such that the output voltage from each amplifier has a one-to-one correspondence with the transducer pressure measurement. Therefore, the resulting calibration constant is *1 V/psi*.

The cables used to connect the IC transducers to the amplifiers were fabricated at MIT. These cables mate to the ITT strip connectors on the unsteady IC (see Figure 2.6). The cable mapping schematic from the IC transducers to the amplifiers and from the amplifiers to the data acquisition system is very important to accurately reduce the unsteady data. This mapping information must be recorded for each experiment. Likewise, the mapping of the steady pressure tubing from the IC to the steady data Scani-valve transducer ports must be recorded for each experiment. Table 2.2 is an example of the unsteady data acquisition mapping for the feedback control experiments.

---

[3] Probe 22 is used for comparison because of its relative location to probe 23. Probes 82 and 83 are used because they are located symmetrically, about the vertical center-plane, to probes 22 and 23.

Signal	Location	Cable	Amplifier	Cable	BDT A/D Channel
Total Pressure 1	Sensor Ring	White 1	2310 #9	BNC 1	Z-1
Total Pressure 2	Sensor Ring	White 2	2310 #5	BNC 2	Z-2
Total Pressure 3	Sensor Ring	White 3	2310 #6	BNC 3	Z-3
Actuator Command	Controller	-	-	BNC 4	Z-4
Bulk Parameter	Controller	-	-	BNC 5	Z-5
Actuator Position 1	Actuator Tower	-	-	BNC 16	Z-6
Actuator Position 2	Actuator Tower	-	-	BNC 17	Z-7
Actuator Position 3	Actuator Tower	-	-	BNC 18	Z-8
Actuator Position 4	Actuator Tower	-	-	BNC 19	Y-1
Hot-film 4	UCAV Inlet	BNC 15	Dantec #8	BNC 21	Y-2

Table 2.2 – Instrumentation to Data Acquisition Mapping for Feedback Control Experiments
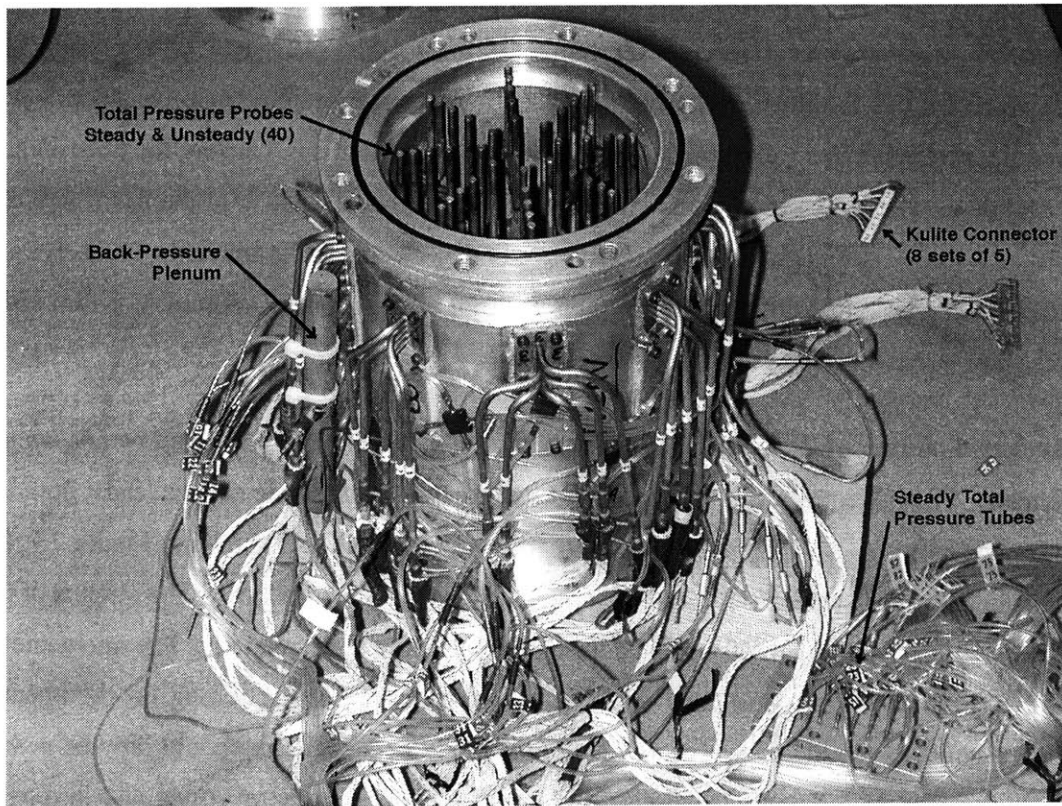
Figure 2.6 – Unsteady Pressure Instrument Can

2.2.1.3 Hot-film Sensors

In order to analyze the relationship between inlet separation and total pressure at the AIP, it is necessary to place hot-film sensors in the separated region of the inlet. Due to the limited number of hot-film sensors available, selecting the placement of these sensors is crucial. To ensure that the hot-film sensors capture the separation flow characteristics, the results of the flow visualization experiments (Section 4.1) were studied to determine the sensor locations with the greatest potential for capturing unsteady shedding events. The white "X's" in Figure 4.4 indicate where the sensors were placed based on flow visualization. Figure 2.7 shows the actual locations of the hot-film sensors on the upper inlet surface. Michael Brear [9], who has experience with this flow visualization technique, assisted in these experiments and helped in selecting the sensor locations. Steve Braddom installed the five hot-film sensors.

The hot-film sensors are SENFLEX SF9902 single element shear stress sensors. Hot-film sensors measure the instantaneous wall shear stress by relating the shear stress to the thermal dissipation through the constant temperature anemometer. In order to maintain constant temperature, the current across the film must vary to account for changes in the hot-film resistance. These changes in hot-film resistance are due to direct relationship between temperature and electrical resistivity. As the shear stress increases the thermal dissipation from the hot-film increases, causing the hot-film temperature to decrease. The temperature decrease lowers the electrical resistance of the hot-film circuitry, thus requiring more current to maintain constant voltage. Kenneth Kalumuck's Ph.D. [17] contains a detailed description of hot-film sensor theory. Table 2.3 lists the important hot-film specifications necessary to use the sensors.

The active portion of each hot-film sensor is a .004 in. wide by .057 in. long by .20 μm thick nickel element. These elements connect to .0005 in. thick by .030 in. wide copper leads; both the element and wires mount to a polyamide substrate (dark maroon color). As shown in Figure 2.7, kapton tape (translucent yellow tape) shields the wire signal leads from the inlet flow. The outputs of the hot-film sensors connect to a bank of Dantec constant temperature anemometers. The anemometers control the overheat ratio, gain and filter settings. Switching the control setting on the anemometers to "flow" activates the hot-film sensors. Note that the hot-film sensors should only be activated when the experiment is running. Otherwise, the hot-film elements may overheat and become defective. The total thickness of the hot-film sensor is important because of its potential influence on separation. If the edge associated with gluing the sensor to the surface of the inlet is greater than the boundary

layer thickness, then the hot-film will act like a trip wire for the flow. Although no rigorous calculations were performed, it is assumed that the boundary layer thickness is on the order of one millimeter. Therefore, the thickness of the sensor (*115 μm*) does not have an effect on the separation properties in the inlet.

Parameter	Value	Description
TRC	0.0235 $\Omega/°C$	Temperature Coefficient of Resistance
R_O^3	4.9 Ω	Ambient Condition Resistance for Hot-film #3
R_O^4	6.1 Ω	Ambient Condition Resistance for Hot-film #4
OH	1.5	Overheat Ratio (Ratio of Hot-film to Ambient Resistances)
y	115 μm	Total Thickness of Hot-films (including Glue and Leads)

Table 2.3 – Hot-film Specifications
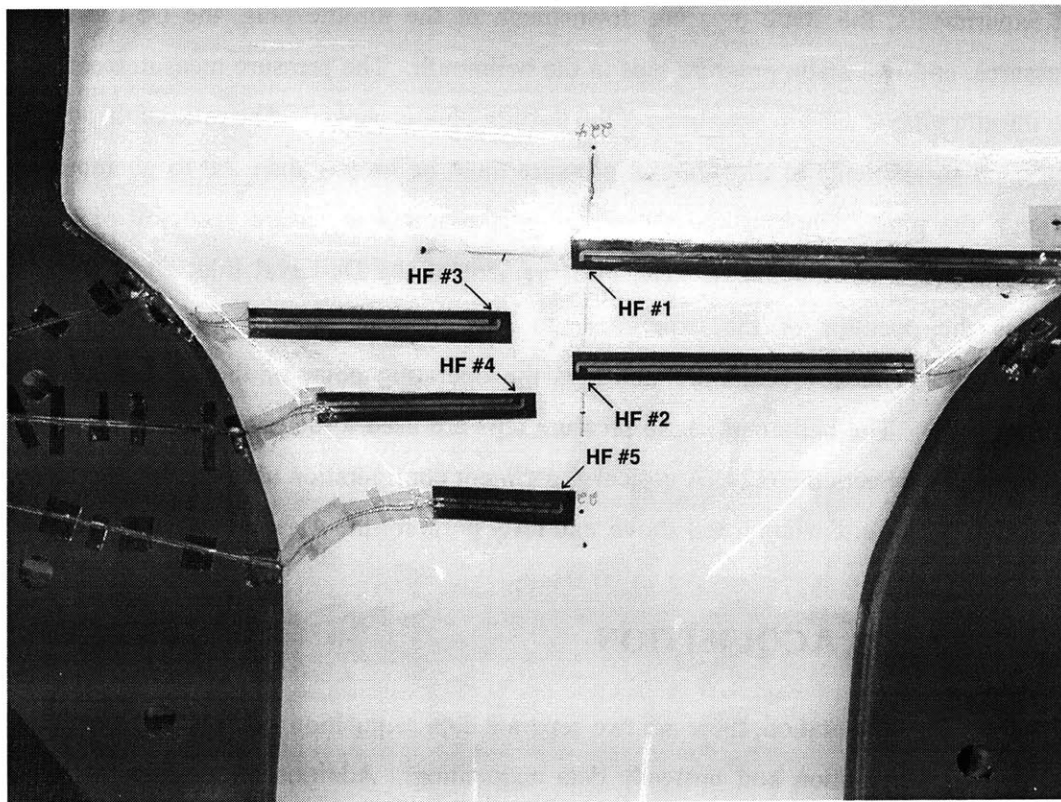
Figure 2.7 – Hot-film Sensor Location

37

2.2.2 STEADY INSTRUMENTATION

The steady instrumentation serves three purposes: providing total pressure measurements at the AIP, determining the mass flow through the test section, and identifying the operating conditions of the De-Laval compressor. A Scani-valve differential pressure transducer takes all of the steady pressure measurements. The Scani-valve has forty-eight available ports, of which one port is used to measure ambient pressure and two ports (3 and 6) are non-functional. The remaining forty-five ports are allocated to the various steady pressure probes, depending on the purpose of the experiment. The Scani-valve has two modes of operation, measuring steady pressure continuously at a single port or incrementally stepping through all forty-eight ports. For these experiments the incremental stepping mode is used.

The steady pressure probes in the experimental setup include forty total pressure probes located in both instrument can rakes, sixteen wall static pressure taps in the inlet, ten wall static pressure taps in the bellmouth, a static pressure tap downstream of the throttle plug, and two taps to measure the inlet and exit pressure of the De-Laval compressor. Only five pressure measurements are required during all experiments; the static pressure downstream of the throttle plug, the De-Laval inlet and exit pressures, and two static pressure taps in the bellmouth. The pressure measurement downstream of the throttle plug is used to determine if the throttle plug is choked. The ratio of throttle inlet pressure (assumed to ambient) to throttle exit pressure must be greater than 2.0 to guarantee choked flow through the plug. Choking the throttle plug is required to ensure accuracy of the throttle plug calibration (see Section 2.6.1). The measurement of the De-Laval inlet and exit static pressures enables the operator of the experiment to determine the pressure ratio across the De-Laval compressor. This pressure ratio indicates the operating point of the De-Laval compressor (see Appendix A). The bellmouth static pressure taps are used to determine the mass flow through the bellmouth (see Section 2.6.2). A typical experiment configuration uses the five Scani-valve ports for the pressure measurements listed above, and forty ports for the AIP pressure measurements in the IC.

2.3 DATA ACQUISITION

As for the instrumentation, there are two separate data acquisition systems in the experimental setup, steady data acquisition and unsteady data acquisition. Additionally, various aspects of the data acquisition systems are classified as being either hardware or software.

2.3.1 STEADY DATA ACQUISITION

2.3.1.1 HARDWARE

The Scan-valve Digital Interface Unit (SDIU) is responsible for controlling the Scani-valve transducer and displaying the output of the Scani-valve transducer. An executable program (see Section 2.3.1.2) running on a PC remotely controls the SDIU. The SDIU processes commands from the executable program, including homing the Scani-valve and triggering data acquisition. The SDIU performs the steady pressure data acquisition and converts the transducer analog response to absolute pressure. The PC then writes the pressure data from the SDIU to a MATLAB variable (.mat) file.

2.3.1.2 SOFTWARE

The software program used to control the SDIU is called scanmanw.exe. Dr. Jim Paduano maintains this program, which is compiled in "C" programming language. The executable program prompts the user for various input data, such as ambient pressure, ambient temperature, and plug voltage. Then, the program initializes the system by setting the Scani-valve port to its home position. Finally, the program supplies the SDIU with the steady pressure calibration coefficients and the data acquisition rate[4]. The calibration of the SDIU / Scani-valve system was performed for earlier research, thus this experimental setup inherited a fully calibrated system. A data acquisition rate of two ports per second is used for these experiments. This rate is chosen to balance total acquisition time (*24 sec*) with adequate transducer accuracy. The transducer accuracy decreases as the data acquisition rate increases.

After the initialization steps are completed, the program prompts the operator to either trigger data acquisition, consisting of a complete cycle through each of the forty-eight ports, or quit the program and save the data. Unlike the unsteady data acquisition system, the steady software stores multiple experiment runs in a single data file. For example, if an experiment consists of six different data sets, then six unsteady data files and one steady data file containing the steady data of each of the six runs.

---

[4] The Scani-valve transducer scans through the forty-eight available ports at variable step rate ranging form one to eight ports per second. The error in the transducer measurement decreases for lower step rates because of the settling time in the transducer.

Aside from commanding the SDIU and writing the data to a file, the scanmanw.exe program performs much of the steady pressure data reduction. The Scani-valve is a differential pressure transducer, and for these experiments the backpressure is atmospheric. Therefore, the pressure output of the SDIU is the difference between the measured pressure and ambient pressure. The scanmanw.exe program takes this pressure difference and computes the absolute pressure, of every port, by adding the input ambient pressure[5]. The program then calculates the bellmouth mass flow (see Section 2.6.2), the De-Laval compressor pressure ratio, and the throttle plug pressure ratio. Finally, the program uses the throttle plug pressure ratio and the throttle plug position (from a linear displacement transducer) to determine if the throttle is choked. If the plug is choked, then scanmanw.exe calculates the mass plug mass flow (see Section 2.6.1). All of these reduced quantities, along with the absolute pressure of each Scani-valve port are saved in a MATLAB variable file.

2.3.2 UNSTEADY DATA ACQUISITION

2.3.2.1 HARDWARE

To capture the data from the unsteady IC and hot-films a high-speed data acquisition system is required. The original high-speed system, consisting of two multiplexed A/D cards, proved to be unreliable. Therefore, the thoroughly tested data acquisition system from the Blow Down Turbine (BDT) is used for the A/D conversion of the unsteady response signals. The A/D converters have a variable peak-to-peak voltage setting; a setting of $\pm 5V$ is used for these experiments. The only drawback of the BDT system is the lack of available channels for recording data (maximum of sixteen). This constraint is severe because, of the eight five-probe rakes in the unsteady IC, it is only possible to record the measurements of three rakes per experiment. This limitation only affects the characterization of AIP total pressure unsteadiness. The feedback control experiments, which use the sensor ring, only require twelve high-speed channels (see Table 2.2). Despite this limitation, the BDT system provides reliable *20 kHz* data for time segments in excess of twelve seconds (well more than required).

2.3.2.2 SOFTWARE

---

[5] The ambient pressure is a user input; a Model 370 SETRA Digital Pressure Gage is used to measure the ambient pressure.

A software program called MMADCAP controls the BDT data acquisition and organizes the digital output into a data file. For each data acquisition set MMADCAP requires initialization, where the peak-to-peak voltage setting, acquisition time and acquisition rate must be specified. The units of the data written to the data file are counts, and the conversion to engineering units resides in the experiment setup file. Conversion from the raw counts data file to a useable MATLAB file is performed by the Adtektomat_z.m MATLAB code. The output of the Adektomat_z.m conversion is a MATLAB data file (e.g. data.mat) containing the raw data converted to engineering units. Dr. Jerry Guenette [8], Principle Researcher at the GTL, created and maintains these programs and the BDT data acquisition system. Any questions concerning the use of the BDT data acquisition system should be directed to Dr. Guenette.

2.3.3   SPECTRUM ANALYZER AND OSCILLOSCOPE

The previous two sections discussed the data acquisition systems used to record experimental data. This section describes the two pieces of equipment used to study the real-time unsteady behavior of the experimental system. An oscilloscope is used to examine the signals from the unsteady sensors and the actuators while the experiment is running. With respect to the actuators, it is important to view the actuator position signal to ensure that each actuator is functioning properly. It is also beneficial to use the oscilloscope to view the signals from the unsteady instrumentation to ensure that each sensor, especially the hot-film, is functional.

The spectrum analyzer is used during the single-frequency feedback control experiments (Section 5.1) to study the effectiveness of feedback control. The spectrum analyzer generates a time averaged RMS frequency profile of the parameter subject to feedback control. This real-time description of the broadband RMS allows the operator to adjust the control law during the experiment, to optimize the effects of feedback control.

2.4   ACTUATION SYSTEM

NASA Glenn supplied MIT with the four Moog actuators used in the active flow control experiments. The purpose of these actuators is to modulate high-pressure airflow through a valve that feeds an injector. Each actuator has a bandwidth of *500 Hz* and an input voltage range of *± 10 V*. Along with

the actuators, shown in Figure 2.9, NASA supplied the equipment necessary to control and monitor the actuator valve position.
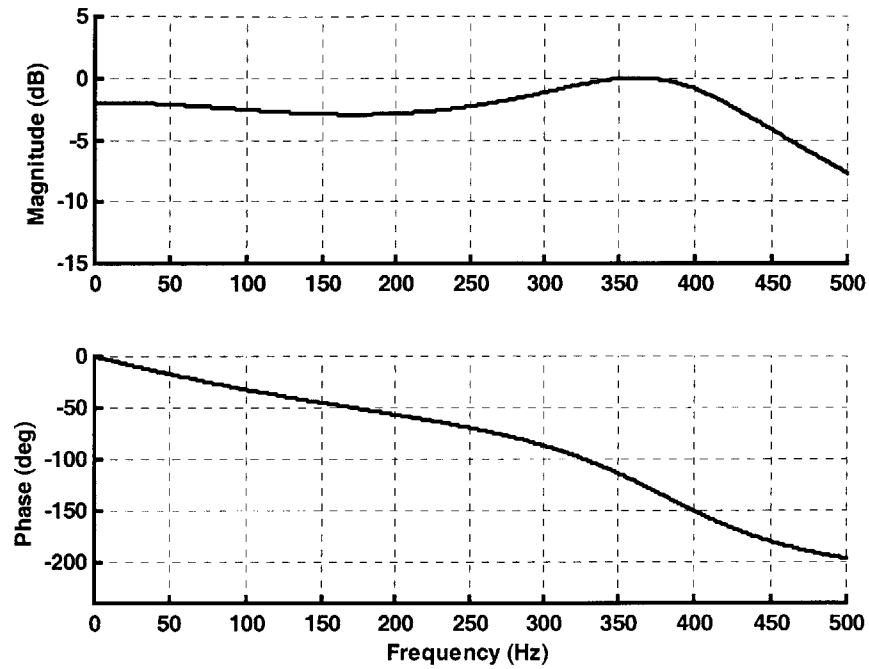
Figure 2.8 – Typical Actuator Servo Motor Transfer Function

Figure 2.8 shows the typical command voltage to position voltage transfer function for an actuator servo motor. It is important to note that this transfer function does not include the factor of ten reduction from command to position voltage. For example, a command voltage of *4 V* at *200 Hz* produces a position voltage of *0.28 V* rather than *2.8 V*. The model for the servo motor transfer function is a third order system, including one zero, three poles, and a slight time delay. Equation 2.1 and Table 2.4 describe the model used to generate the transfer function in Figure 2.8. A detailed description of the actuator dynamics, including the servo motor transfer functions for each actuator, is presented in Section 2.3.3 of Harald Weigl's Ph.D. Thesis [10].

$$TF = \frac{k \cdot (s - z_1)}{(s - p_1) \cdot (s - p_2) \cdot (s - p_3)} e^{-s\tau}$$

(2.1)

Parameter	Value	Description
s	$j \cdot \omega$	Laplace Variable
z_1	-3456 rad/s [-550 Hz]	First Zero
$p_{1,2}$	-503 ±j·2388 rad/s [-80 ±j·380 Hz]	Complex Pole Pair
p_3	-1068 rad/s [-170 Hz]	Third Pole
τ	0.00015 sec	Time Delay
k	1.472 x 10^6	Gain

Table 2.4 – Servo Motor Transfer Function Parameters
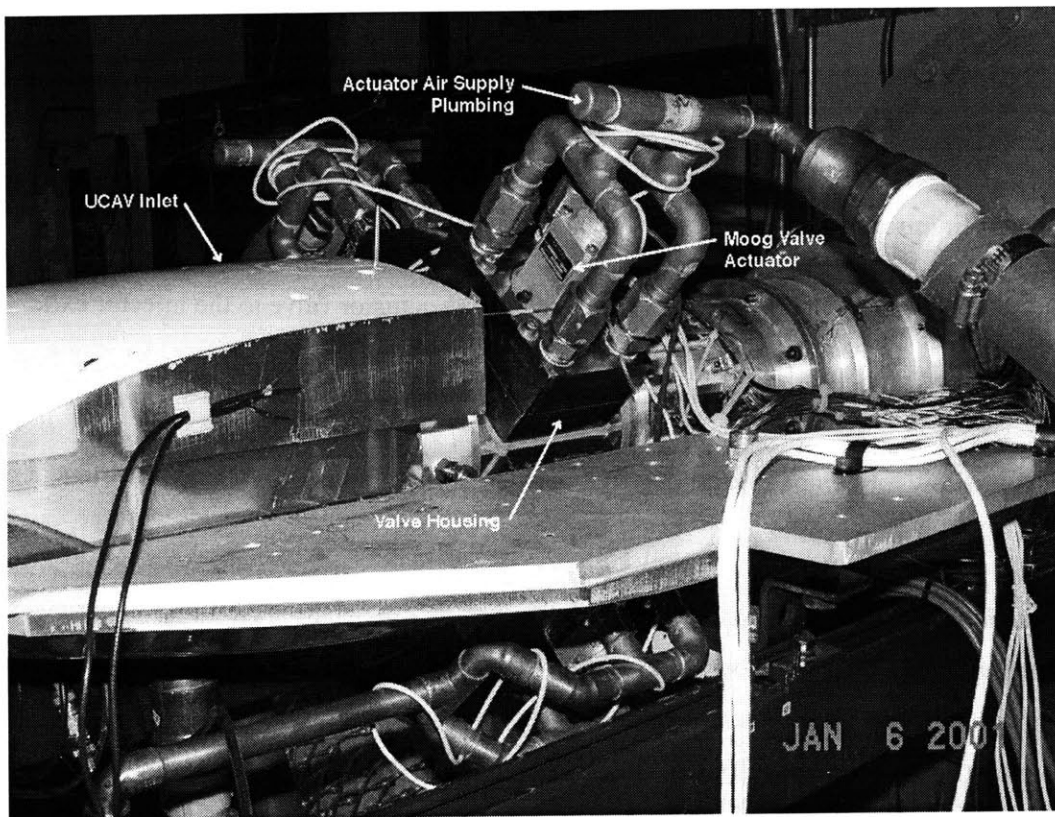
Figure 2.9 – Actuation System Assembly

The air supply for the actuators is a *100-psi* oil free air compressor. The *100-psi* air supply connects to a regulator, allowing the operator of the experiment to adjust the supply pressure feeding the actuators. Downstream of the regulator, a manifold splits the supply air into four lines, each supplying one actuator. Care was taken in plumbing the actuators to ensure that each actuator is subject to equal supply pressures. However, there is no means of determining if the supply pressures

43

are identical during an experiment. The maximum recommended supply pressure for any experiment is *40 psi*. When the supply pressures exceed *40 psi* the servo motor response deteriorates sporadically and unpredictably.

2.4.1 ACTUATOR DUCT DESIGN

The actuators sent to MIT by NASA came from a larger compressor test facility, where twelve actuators were mounted circumferentially around the compressor casing. This research pertains to a one-sixth-scale inlet; therefore, the AIP diameter is one-sixth of the full-scale compressor diameter. This presented a problem in designing the mounting scheme for the actuators and in designing the injection scheme. Because of the large mounting footprint of the actuators (*4.50* by *3.25* inches) and the reduced AIP diameter, *3.95 in.*, it is possible to mount only four actuators circumferentially around the AIP test section. The constraints that drove the actuator duct design were:

- Minimize the axial length of the actuator duct.

- Minimize the length of the flow path from the actuator valve to the injector exit.

- Provide adequate structural support for mounting the four actuators.

- Allow for compatible mating of the actuator duct to the UCAV inlet, instrument can, throttle plug and sensor ring.

Reduction of the axial length of the actuator duct is crucial because these experiments study the upstream effects of active flow control from actuators located at the compressor face. Therefore, it is important to locate the injectors as close to the AIP as possible. The actuators have a rectangular mounting footprint of *4.50* by *3.25* inches. Therefore, the shortest axial length of the actuator duct that supports the actuators and accounts for adequate mating flanges is *5.0 in.* In this configuration the narrow side of the actuator must be parallel to the axis of the actuator duct.
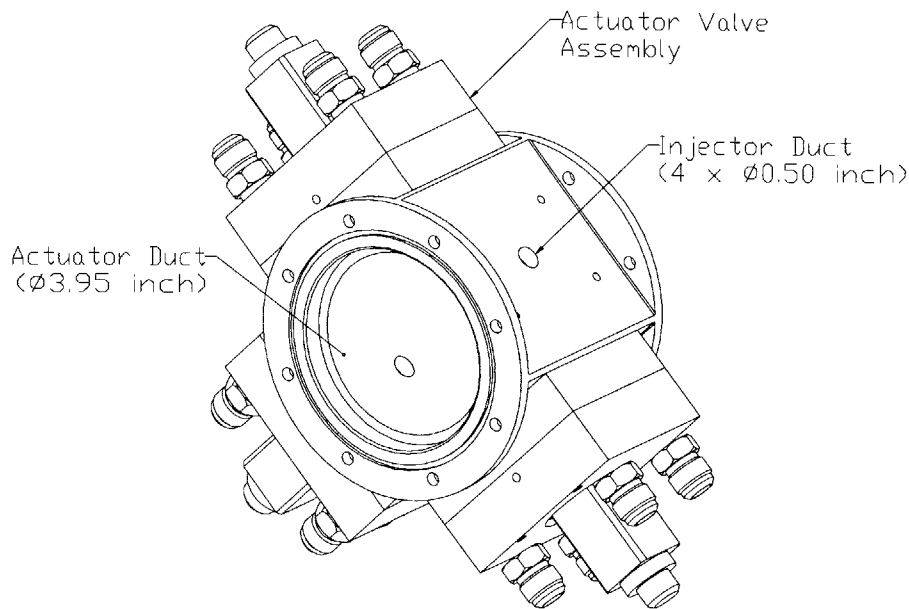
Figure 2.10 – Actuator Duct Design

The purpose of the second constraint is to eliminate or reduce the potential of acoustic modes developing in the injector ducting. Weigl's thesis [10] discusses the Helmholtz resonator effects associated with various injector duct designs. These effects acoustic modes worsen as the length of the injector ducting increases. Based on this desire to minimize injector duct length, the four actuators are located at 90° angular increments relative to one another (see Figure 2.10). Thus, the four mounting surfaces for the actuators constitute a square centered about the duct axis. The minimum side length for this square is *4.50 in.* (maximum footprint of the actuator), and the duct inner diameter is *3.95 in.* Therefore, the minimum distance from the actuator mounting-surface to the inner duct wall is *0.275 in.*, located on the plane that passes through the duct axis perpendicular to the actuator mounting-surface. Locating the injector duct along this plane makes the actuation scheme circumferentially symmetric, with the injection flow path pointing towards the center of the duct. Although the minimum duct length is *0.275 in.*, the third constraint dictates that enough material be placed between the actuator mounting-surface and the inner duct wall to ensure adequate support of the actuators. Increasing the minimum injector duct length to *0.375 in.* ensures the structural integrity of the duct in supporting the four *10 lb.* actuator valve assemblies and their respective plumbing.

The final constraint dictates the design of the mounting flanges that mate to the various components in the experimental setup. Both flanges feature a pattern of eight thru-holes matching the hole-

patterns of the UCAV inlet, IC and throttle plug (see Figure 2.10). The actuator duct also features a concentric tongue and groove arrangement similar to that of the inlet and IC. This feature allows for the proper axial alignment of the concentric components, and it aides in sealing the setup from flow leakage. Refer to Figure B.3 and Figure B.4 for the detailed fabrication drawing of the actuator duct.

The design of the injector duct was given great consideration for this series of experiments. The two parameters of the injection design are the injector area and the injection angle. Due to time constraints and fabrication costs, and to simplify the flow physics, the injection scheme for Phase 1 experiments is a straight cylindrical duct perpendicular to the airflow in the actuator duct. The purpose of this injection configuration is to introduce planar acoustic waves into the UCAV inlet. Despite this initial injection configuration, the actuator duct is designed to accommodate more complicated injection schemes. By using an injector adapter plate, such as the Coanda injector designed for the full-scale NASA experiments [4], any injection geometry is feasible. The only change required to the existing actuator duct is a modification of the current injection hole to a slot that accommodates an injector adapter plate. The last design parameter in the injection scheme is selecting the diameter of the circular injection slot. For these experiments it is desired to select one of Berndt's [4] circular injector diameters, because these geometries have been proven to work by experimentation. Based on the design specifications in Berndt's thesis, a one-half inch diameter injector is used for these experiments.

2.5   FEEDBACK CONTROL HARDWARE AND SOFTWARE

The system used to execute feedback control laws in the experimental setup consists of both hardware and software. The hardware includes a digital signal processor (DSP) board used to execute the discrete control law calculations. The DSP board contains A/D and D/A converters capable of supporting sixteen channels. Eight A/D's convert input analog signals to digital signals (counts) and eight D/A's convert output digital signals to analog signals (volts). The DSP processor continuously runs an executable file compiled in C. There are versions of the control law program for each of control law variations. The operator initiates a control law by downloading the executable file to the DSP. In most cases the operator selects the sampling frequency for the DSP. This sampling rate should correspond to the sampling rate used to design the discretized control law. Dr. Jim Paduano maintains each of these programs.

2.6 SYSTEM CALIBRATION

There are two types of calibrations required to perform experiments on the UCAV test section: calibrating the mass flow through the test section and calibrating the instrumentation used to make measurements in the test section. The primary calibration of the mass flow through the test section is an adaptation of the Northrop Grumman calibration of mass flow through the throttle plug. Section 2.6.1 describes the Northrop Grumman calibration and how it is applied to this experimental setup. A second source for determining mass flow, using bellmouth static pressure measurements, enables an alternate calculation of mass flow through the test section. This calibration is determined experimentally by comparing the bellmouth static pressure to the plug mass flow. Section 2.6.2 describes the creation and application of the bellmouth mass flow calibration.

The second type of calibration required to perform experiments on the test section is the calibration of the unsteady pressure transducers. Unlike the mass flow calibration, which was performed only once, the calibration of the pressure transducers must be performed prior to each experiment. Section 2.6.3 describes the calibration of these transducers located in either the unsteady IC or sensor ring.

2.6.1 THROTTLE PLUG MASS FLOW CALIBRATION

Calibration of the mass flow plug consists of two separate calibrations. Northrop Grumman provided the first calibration, which determines mass flow as a function of plug position. Figure 2.12 shows the polynomial calibration curve fit provided by Northrop. The ambient conditions during Northrop's calibration were standard atmospheric conditions, *14.7 psi* and *73 °F*. However, the IC was mated to the throttle plug during Northrop's calibration. Therefore, this calibration curve is only valid for experimental setups in which the throttle plug and IC mate together.

The second calibration correlates the plug position to the plug output control voltage. This calibration, first performed on October 24th, 2000, involves manually measuring the plug position for various plug voltages. Based on the October calibration, the relationship between voltage and position, shown in Figure 2.11, is linear. Several months later, recalibration of the plug indicated that the voltage drifted slightly over the four-month time interval. Section 2.6.1.1 discusses the implications of this voltage error in the mass flow determination.

47

2.6.1.1 CALCULATING MASS FLOW THROUGH THE PLUG

There are three steps in calculating the plug mass flow. First, the position of the plug is determined based on the plug voltage output. The throttle plug control system, described in Appendix A.4, traverses the plug position and displays a voltage reading corresponding to the plug position. Then, the plug position is used to determine the mass flow at the Northrop Grumman calibration ambient conditions. Finally, equation 2.2 corrects the mass flow by accounting for the ambient atmospheric conditions during the experiment. The starred (*) variables in equation 2.2 represent the mass flow, pressure and temperature at the Northrop Grumman calibration conditions, whereas the non-starred variables apply to the experiment ambient conditions.

$$\dot{m} = \dot{m}^* \left(\frac{P}{P^*} \right) \sqrt{\frac{T^*}{T}}$$

(2.2)

As previously mentioned, the slight drift in the voltage to position calibration over time causes an error in the mass flow determination. Since the measured plug voltage increased for the same position, the calculated mass flow increased for the same position. Thus, as the measured plug voltage drifts positively, the estimate of plug mass flow becomes greater than the actual mass flow. The calibration drift leads to approximately a $\pm 2\%$ error in plug mass flow.

48

On 10/24/00, X = 0.50517*V-0.27751

On 02/22/01, X = 0.50398*V-0.29231
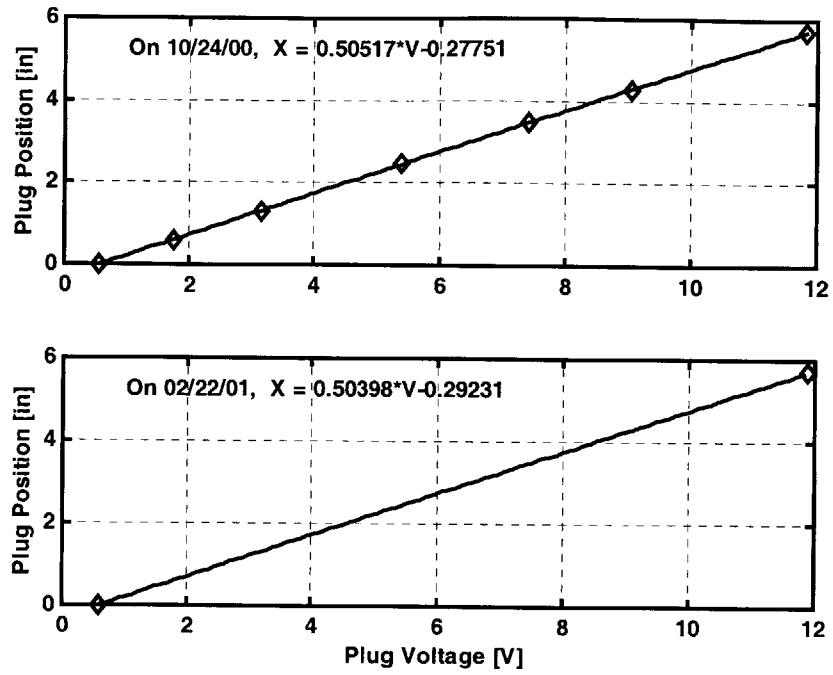
Plug Voltage [V]

Figure 2.11 – Throttle Plug Voltage to Position Calibration

$M = -0.0068X^4 + 0.049X^3 + -0.201X^2 + 1.355X + -0.016$

Plug Position [in]
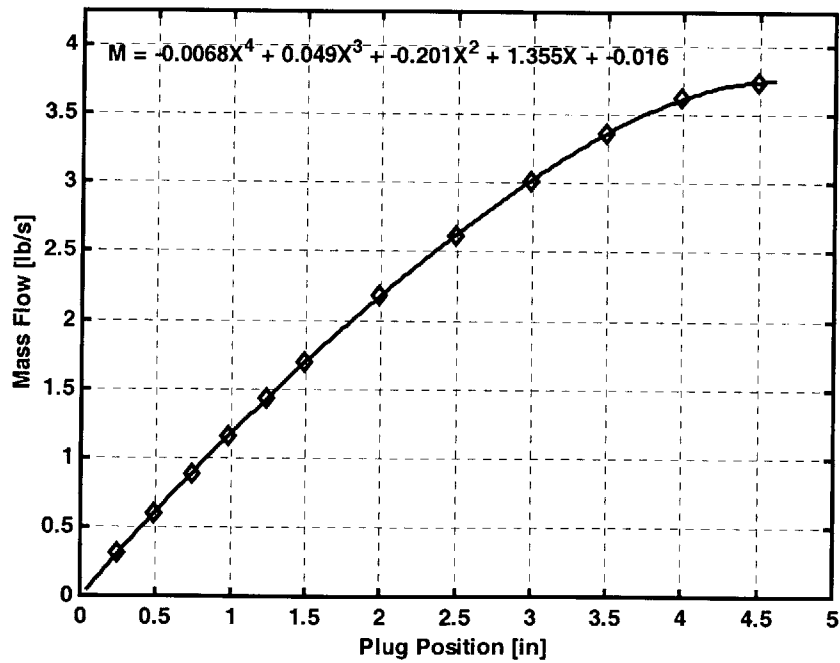
Figure 2.12 – Northrop Grumman Throttle Plug Calibration

2.6.2 BELLMOUTH MASS FLOW CALIBRATION

There were two reasons to create an alternate measure of mass flow through the test section (bellmouth). To accurately measure the mass added to the system from the actuators, the mass flows before and after the injection plane must be measured. The second reason is that many experimental configurations do not include the IC, as in the case of flow visualization. In these cases, the throttle plug calibration is not valid. The mass flow through the bellmouth is calculated from the wall static pressure at two different ports within the bellmouth. Each port has its own calibration curve, and the mass flow is the average of the mass flows predicted by the two static pressures. The calculation of bellmouth mass flow is sensitive to the ambient conditions during the experiment. Therefore, the calibration uses a corrected mass flow technique to account for variation in these ambient conditions. The corrected mass flow technique involves the following steps:

1. Non-dimensionalize the static pressure using the ambient conditions of experimental run.

2. Uses the calibration curve to determine the non-dimensional mass flow.

3. Re-dimensionalize the mass flow using the ambient conditions of experimental run.

The following derivation was performed to determine the appropriate non-dimensional representations of static pressure and mass flow necessary to perform the corrected mass flow calculations. This derivation is based on uniform incompressible flow through a frictionless duct. The derivation is not intended to determine the calibration curve; it is only used to develop the non-dimensional terms. The calibration curve was developed experimentally. Bernoulli's equation (equation 2.3) relates the local flow velocity to the difference between ambient pressure and static pressure. Equation 2.4 is found by solving Bernoulli's equation for the uniform flow velocity.

$$P_\infty = P_s + \frac{\rho}{2}u^2$$

(2.3)

$$u = \sqrt{\frac{2(P_\infty - P_s)}{\rho}}$$

(2.4)

50

The density of the air is assumed to be constant and adhere to the Ideal Gas Law (equation 2.5). Given these assumptions, the mass flow and static pressure are related by substituting equations 2.4 and 2.5 into the equation for mass flow conservation (equation 2.6).

$$\rho = \frac{P_\infty}{RT_\infty}$$

(2.5)

$$\dot{m} = \rho \cdot u \cdot A$$

(2.6)

The resulting relationship between mass flow and static pressure, equation 2.7, depends on the ambient conditions, P_∞ and T_∞, at the time of the experiment. The bellmouth area, A, and the gas constant, R, is assumed to be constant for all experiments (see Table 2.5).

$$\dot{m} = \left(\frac{AP_\infty}{\sqrt{RT_\infty}} \right) \sqrt{\frac{2\left(P_\infty - P_S\right)}{P_\infty}}$$

(2.7)

Parameter	Value	Description
T_∞^*	73 °F	Ambient Temperature during Calibration
P_∞^*	14.66 psi	Ambient Pressure during Calibration
A	20 in²	Effective Area of Bellmouth
R	53.35 $\frac{lb_f in^3}{lb_m R}$	Gas Constant for Air

Table 2.5 – Mass Flow Calibration Parameters

Re-organizing the terms in equation 2.7 yields the non-dimensional terms for static pressure (equation 2.8) and bellmouth mass flow (equation 2.9).

51

$$\Psi = \frac{P_\infty - P_S}{P_\infty}$$

<div align="right">(2.8)</div>

$$\Phi = \left(\frac{\sqrt{RT_\infty}}{AP_\infty} \right) \dot{m}$$

<div align="right">(2.9)</div>

These non-dimensional parameters are used to generate the experimental calibration curve, shown in Figure 2.13. Recording static pressures in the bellmouth at known throttle mass flows provided the data to generate the curve fits. The ambient conditions used to non-dimensionalize the calibration data are shown in Table 2.5. The curve fits, shown in Figure 2.13, were generated such that non-dimensional mass flow, Φ, is a function of non-dimensional static pressure, Ψ.

$$\Phi \approx f(\Psi)$$

<div align="right">(2.10)</div>

The procedure for calculating the corrected mass flow is to first measure static pressure and the ambient conditions. Then, non-dimensionalize the static pressure using equation 2.8. Use the calibration curve to determine the non-dimensional mass flow, Φ. Finally, re-dimensionalize the mass flow by inverting equation 2.9. The calibration is only accurate for mass flows less than $3.6\ lb/s$ due to the flow properties in the bellmouth. Figure 2.14 shows the mass flows of an independent experiment thus validating the bellmouth calibration.

Please note that the non-dimensionalization described in this section was derived from incompressible flow equations. In actuality, the flow at the bellmouth static ports in compressible ($M \sim 0.4$). For future research the bellmouth mass flow calibration should be reconstructed to include compressibility. Despite this oversight, this calibration of the bellmouth is adequate for this set of experiments because the ambient conditions varied only slightly from one experiment to the next. The mass flow corrections due to the changes in ambient conditions are small (less than 2%), therefore, errors in the correction are even less.
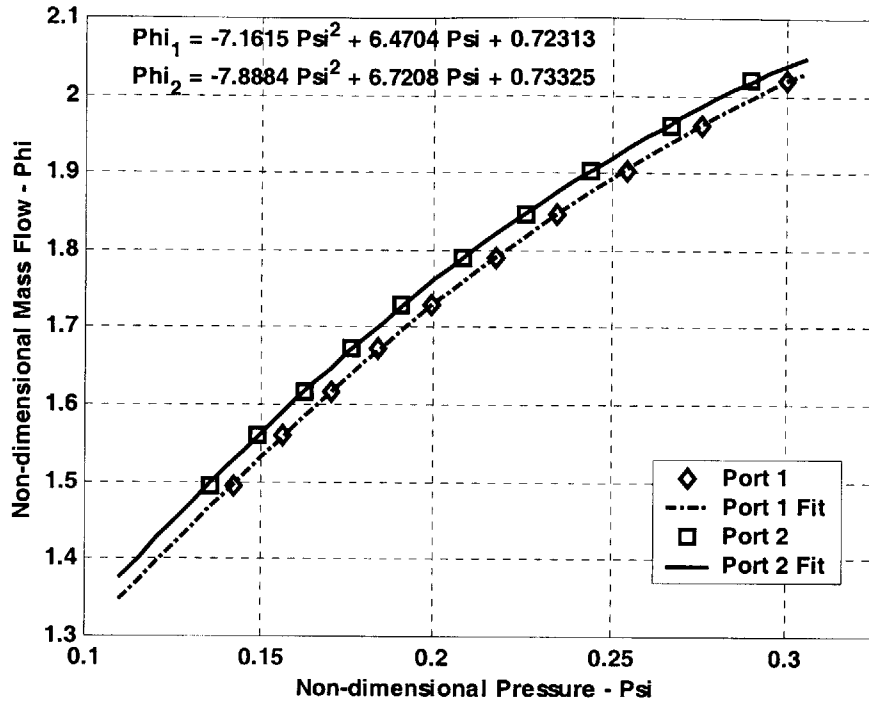
Figure 2.13 – Bellmouth Calibration
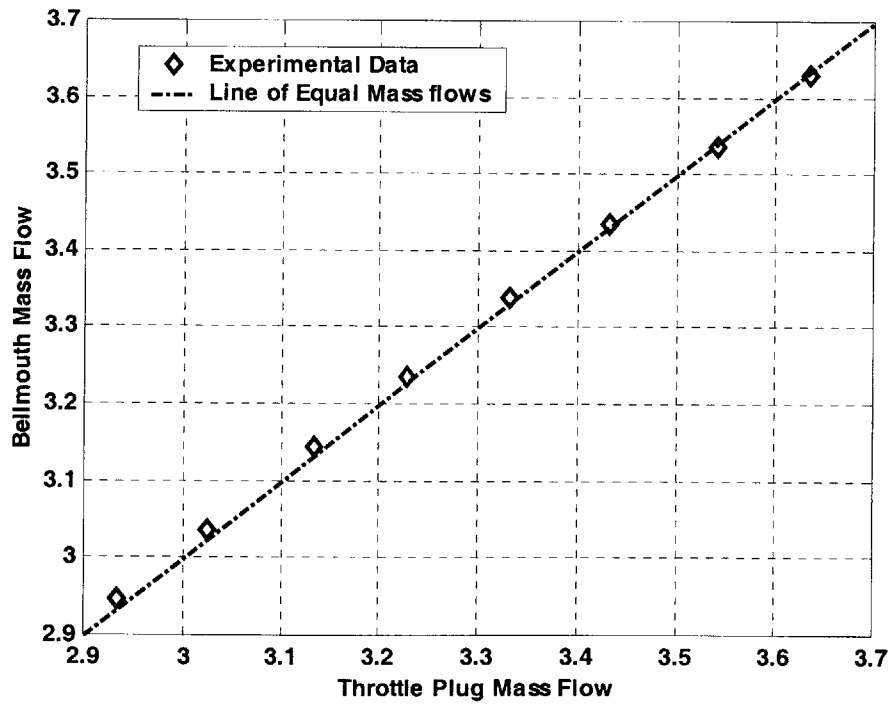
Figure 2.14 – Verification of Bellmouth Calibration

53

2.6.3 UNSTEADY TRANSDUCER CALIBRATION

The forty transducers in the unsteady instrument are not exactly identical. Aside from the varying bridge resistances, each transducer responds differently to changes in ambient pressure and temperature. For these reasons, it is necessary to calibrate each pressure transducer individually on the day of an experimental run. To simplify data reduction, the transducers are calibrated such that one psi of gage pressure at a transducer corresponds to one volt of output from its respective amplifier. This one-to-one relationship is achieved by adjusting the amplifier gain while supplying one psi of backpressure to each transducer. See Appendix A.3 for a detailed description of the calibration procedure.

3 1-D ACOUSTIC MODEL OF INLET

This chapter discusses the development, application and results of a one-dimensional (1-D) acoustic model of the UCAV inlet. The model uses a linearized transmission matrix technique to estimate the axial pressure and velocity perturbation response of the MIT experimental setup.

3.1 MODEL MOTIVATIONS AND LIMITATIONS

The primary motivation for creating a 1-D acoustic model of the experimental setup is to gain understanding of the effects of downstream planar actuation in the UCAV inlet. Calculating the transfer function between the injection flow and the pressure response at the AIP captures this effect. Modeling techniques are discussed in Section 3.2, while the derivation and results of the acoustic transfer function are discussed in Section 3.3.

Another motivation for creating a 1-D acoustic model is to use the injectors at the AIP to emulate the downstream impedance of a compression system. In order to emulate the compressor impedance in the experimental setup, the model must generate a transfer function from the AIP total pressure to the injectors. This transfer function serves as a control law by feeding back the pressure at the AIP thus determining the injection necessary to achieve emulation. Unfortunately, due to the limited timeline of this thesis, an attempt at implementing compressor emulation during an experiment is not possible. However, for future research, an outline of compressor emulation via 1-D acoustic modeling is presented in Section 3.4.

The glaring limitation of this model is that it is only a one-dimensional model, capable of modeling only the planar, axial acoustic effects in the system. Therefore, this model is incapable of capturing any of the radial or circumferential effects related to AIP distortion or separation unsteadiness. Despite these limitations, the model provides a basis for understanding the acoustics of the inlet.

3.2 MODELING TECHNIQUES

The concept of globally non-dimensionalized transmission matrices, developed by Brandon Gordon [13], is used to model the inlet acoustics. These frequency-dependent transmission matrices describe relationships between non-dimensional pressure and velocity perturbations for various propulsion system components, including acoustic ducts, compressors, throttles and plenums. Each transmission matrix captures the linearized evolution of the flow properties from the inlet to the exit of a particular component. This relationship between flow entering and exiting a component is described by equation 3.1, where ψ_1 and ϕ_1 are the exit static pressure and velocity perturbations, and ψ_0 and ϕ_0 are the inlet static pressure and velocity perturbations. T_{01} is the two-by-two transmission matrix that relates these flow properties.

$$\begin{bmatrix} \psi_1 \\ \phi_1 \end{bmatrix} = T_{01} \begin{bmatrix} \psi_0 \\ \phi_0 \end{bmatrix}$$

(3.1)

The primary advantage of using linearized transmission matrices is that simply multiplying their respective transmission matrices connects the flow properties of two components. Therefore, modeling a system of multiple components, such as a compression system, is simplified by the multiplication of the individual transmission matrices. The transmission matrices for each component derive from linearized compressible flow equations. For example, the two equations used to derive the acoustic duct transmission matrix are Euler's equation and the continuity equation. Refer to notes by Paduano [24] for the derivations of each transmission matrix. To implement the transmission-matrix technique it is assumed that the physical properties such as area, Mach number, density and speed of sound are constant over the length of the component. The transmission matrices used in the analysis of this chapter are listed below. The transmission matrix describing an acoustic duct, T_{AD}, includes a Mach number correction. This correction is not necessary in many acoustical analyses. However, since the UCAV inlet experiences high Mach number flows, this correction is necessary to accurately model the inlet. Table 3.1 provides a description of the parameters in the transmission matrices.

56

Acoustic Duct:

$$T_{AD} = e^{\left(\frac{jL^*\omega^* M}{a^*\left(1-M^2\right)}\right)} \begin{bmatrix} \cos\left(\dfrac{L^*\omega^*}{a^*\left(1-M^2\right)}\right) & -j\rho^* a^* \sin\left(\dfrac{L^*\omega^*}{a^*\left(1-M^2\right)}\right) \\ -\dfrac{j}{\rho^* a^*}\sin\left(\dfrac{L^*\omega^*}{a^*\left(1-M^2\right)}\right) & \cos\left(\dfrac{L^*\omega^*}{a^*\left(1-M^2\right)}\right) \end{bmatrix}$$

Throttle:

$$T_{Thrt} = \begin{bmatrix} 1 & -\rho^* a^* \dfrac{\partial \Psi_T}{\partial \Phi} \\ 0 & 1 \end{bmatrix}$$

Compressor:

$$T_{Comp} = \begin{bmatrix} 1 & \rho^* a^* \dfrac{\partial \Psi_C}{\partial \Phi} \\ 0 & 1 \end{bmatrix}$$

Lumped Plenum:

$$T_{LP} = \begin{bmatrix} 1 & 0 \\ \dfrac{-j\omega^* L^*}{\rho^* a^{*2} A_1^*} & \dfrac{A_0^*}{A_1^*} \end{bmatrix}$$

Parameter	Non-Dimensional	Description
L^*	$\dfrac{L}{L_{REF}}$	Non-dimensional Length
a^*	$\dfrac{a}{a_{REF}}$	Non-dimensional Speed of Sound
ρ^*	$\dfrac{\rho}{\rho_{REF}}$	Non-dimensional Air Density
ω^*	$\dfrac{\omega \cdot L_{REF}}{a_{REF}}$	Non-dimensional Angular Frequency
$A_{0,1}^*$	$\dfrac{A_{0,1}}{A_{REF}}$	Non-dimensional Plenum Inlet / Exit Area
$\dfrac{\partial \Psi_T}{\partial \Phi}$	-	Throttle Slope
$\dfrac{\partial \Psi_C}{\partial \Phi}$	-	Compressor Slope
ψ^*	$\dfrac{P}{\rho_{REF} a_{REF}^2}$	Non-dimensional Pressure
ϕ^*	$\dfrac{u}{a_{REF}}$	Non-dimensional Velocity

Table 3.1 – Transmission Matrix Parameters

3.3   ACOUSTIC MODEL OF EXPERIMENTAL SETUP

The components in the experimental setup have varying area, Mach number and density. There are also various points of interest within these components where computing the flow properties is required. For these reasons, it is necessary to partition each component into multiple segments, with each segment having its own transmission matrix. For example, the bellmouth component, the first section in Figure 3.1, is partitioned into ten segments to capture changes in Mach number and density as the bellmouth area decreases. According to equation 3.2, the transmission matrix for an entire component is the sequential product of the transmission matrices of each segment within the component.

$$T = \prod_{i=1}^{N} T_i$$

(3.2)

Figure 3.1 illustrates all of the components used in the flow control experiments, the bellmouth, inlet diffuser, sensor ring, actuators duct, instrument can and throttle plug. Of these components, all are modeled as acoustic ducts (with Mach number correction) except for the throttle plug, which is modeled as a throttle. Like the actual experimental setup, the model components are interchangeable, allowing for any experimental configuration to be modeled. A MATLAB code, listed in Appendix D, is used to evaluate the transmission matrix model of the experimental setup. Given the configuration of the components, the MATLAB code calculates the transfer function from the actuator flow to the AIP. The following section derives the equations and transfer function relationships used to create this acoustic transfer function. The parameters of interest within the acoustic model are the pressure response at the AIP, ψ_{AIP}, and the input velocity of the actuators, ϕ_I.

58
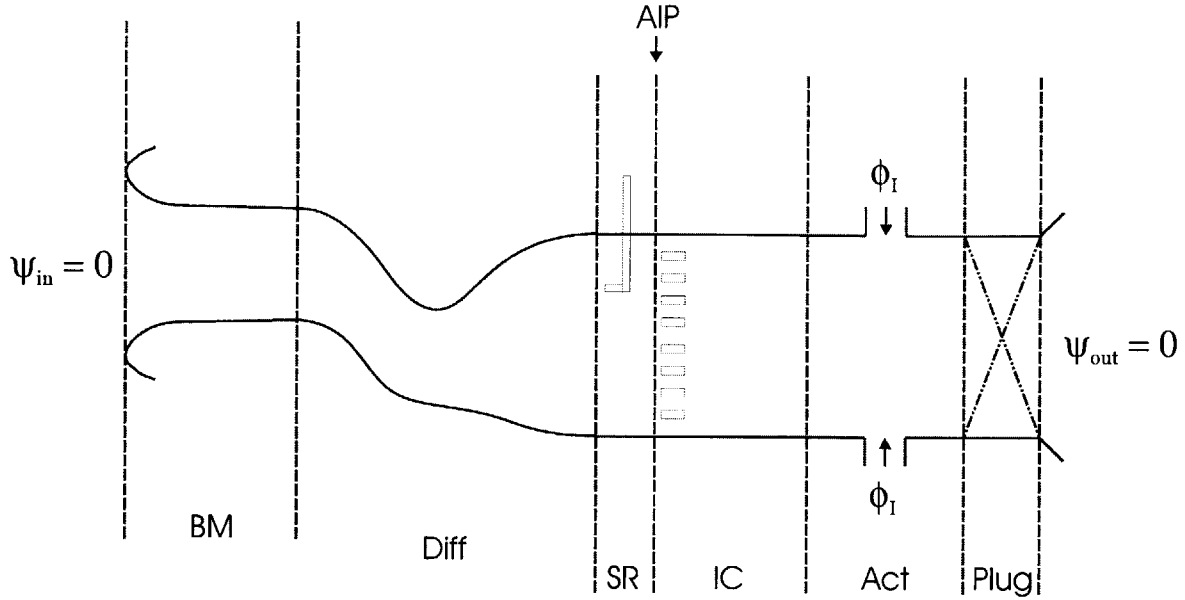
Figure 3.1 – Experiment Acoustic Model

3.3.1   AIP INJECTION TO PRESSURE TRANSFER FUNCTION

The AIP is the location of the unsteady pressure sensors in the experimental setup. Therefore, to best understand / predict the acoustical effects in the test section, the transfer function from the injectors to the AIP must be modeled.   Solving for this transfer function requires deriving two relationships within the duct flow.   The first is the relationship between the inlet and AIP flow properties. Following the form of equation 3.1, the transmission matrices of the inlet diffuser and the bellmouth define this relationship (see equation 3.3).   Equation 3.3 also defines a simplified representation of this relationship, where $V(j\omega) = T_{Diff}T_{BM}$.

$$\begin{Bmatrix} \psi_{AIP} \\ \phi_{AIP} \end{Bmatrix} = T_{Diff}T_{BM} \begin{Bmatrix} \psi_{in} \\ \phi_{in} \end{Bmatrix} = \begin{bmatrix} V_{11}(j\omega) & V_{12}(j\omega) \\ V_{21}(j\omega) & V_{22}(j\omega) \end{bmatrix} \begin{Bmatrix} \psi_{in} \\ \phi_{in} \end{Bmatrix}$$

(3.3)

The second relationship relates the exit and inlet flow properties.   This relationship includes the addition of injector mass flow at the center of the actuator duct.   To better represent the location of the injection, the actuator duct is divided into two transmission matrices where, $T_{Act} = T_{Act_1}T_{Act_2}$. Most mass addition occurs across an actuator disk between these tow ducts.   Equation 3.4 captures

59

this mass addition through continuity, where ϕ_I is the injector velocity, A_I is the area ratio of the injector to the actuator duct and the starred properties represent the flow entering the injection plane.

$$\left\{ \begin{array}{c} \psi_{Act} \\ \phi_{Act} \end{array} \right\} = \left\{ \begin{array}{c} \psi_{Act}^* \\ \phi_{Act}^* \end{array} \right\} + \left\{ \begin{array}{c} 0 \\ A_I \end{array} \right\} \phi_I$$

$$(3.4)$$

The flow paths to and from the injection plane are described by equations 3.5 and 3.6.

$$\left\{ \begin{array}{c} \psi_{out} \\ \phi_{out} \end{array} \right\} = T_{Plug} T_{Act_2} \left\{ \begin{array}{c} \psi_{Act} \\ \phi_{Act} \end{array} \right\}$$

$$(3.5)$$

$$\left\{ \begin{array}{c} \psi_{Act}^* \\ \phi_{Act}^* \end{array} \right\} = T_{Act_1} T_{IC} T_{Diff} T_{BM} \left\{ \begin{array}{c} \psi_{in} \\ \phi_{in} \end{array} \right\}$$

$$(3.6)$$

Substitution of equations 3.6 and 3.4 into equation 3.5 yields a relationship between the exit and inlet flow properties. As expected, this relationship is dependent on the injection flow velocity. Equation 3.7 is simplified by performing the transmission matrix multiplications thus, reducing the equation to the form shown in equation 3.8. The combined transmission matrices, T and U, are functions of frequency.

$$\left\{ \begin{array}{c} \psi_{out} \\ \phi_{out} \end{array} \right\} = T_{Plug} T_{Act_2} \left(T_{Act_1} T_{IC} T_{Diff} T_{BM} \left\{ \begin{array}{c} \psi_{in} \\ \phi_{in} \end{array} \right\} + \left\{ \begin{array}{c} 0 \\ A_I \end{array} \right\} \phi_I \right)$$

$$(3.7)$$

$$\left\{ \begin{array}{c} \psi_{out} \\ \phi_{out} \end{array} \right\} = \left[\begin{array}{cc} T_{11}(j\omega) & T_{12}(j\omega) \\ T_{21}(j\omega) & T_{22}(j\omega) \end{array} \right] \left\{ \begin{array}{c} \psi_{in} \\ \phi_{in} \end{array} \right\} + \left\{ \begin{array}{c} U_1(j\omega) \\ U_2(j\omega) \end{array} \right\} \phi_I$$

$$(3.8)$$

To calculate the transfer function from the injector velocity to AIP pressure, two boundary conditions are required. The inlet and exit of the experimental system are infinite pressure plenums at atmospheric pressure. Therefore, it is assumed that the pressure perturbations at the inlet and exit are zero ($\psi_{in} = \psi_{out} = 0$). Given these boundary conditions, solving the four equations in 3.3 and 3.8 yields the following transfer function between AIP pressure and injection flow.

$$\frac{\psi_{AIP}}{\phi_I} = \frac{-V_{12}(j\omega) \cdot U_1(j\omega)}{T_{12}(j\omega)}$$

(3.9)

Figure 3.2 shows the transfer function over the applicable actuator frequency bandwidth used in feedback control experiments. This result provides valuable knowledge of the acoustic behavior in the experimental setup. The accuracy of this model is partially verified by the experimental transfer functions discussed in Section 4.5. Figure 4.14 and Figure 4.15 show the experimental transfer functions from the actuator command voltage to the AIP total pressure measurements. A comparison of these figures to the results of the acoustic model demonstrates some consistency between the theoretical and experimental results. For example, the model predicts a zero in the transfer function at approximately *190 Hz*. This zero coincides with a large dip in the experimental transfer functions. Other features of the acoustic model results do not agree with the experimental transfer functions. In general, damping of the acoustic resonance is much higher in the experimental setup; this is probably due to losses generated by the separated flow [29]. In addition, the experimental transfer functions do not seem to include a pole near *70 Hz*, as shown in Figure 3.2. This discrepancy, along with others, may be due to the low order of the acoustic model. The 1-D model only has the capability of capturing axial perturbations, whereas, the pressure response at the AIP depends on axial, radial and circumferential perturbations. This limitation can be overcome by developing more complex 2-D or 3-D models of the inlet acoustic. However, for this research, only the development of a 1-D model was feasible.
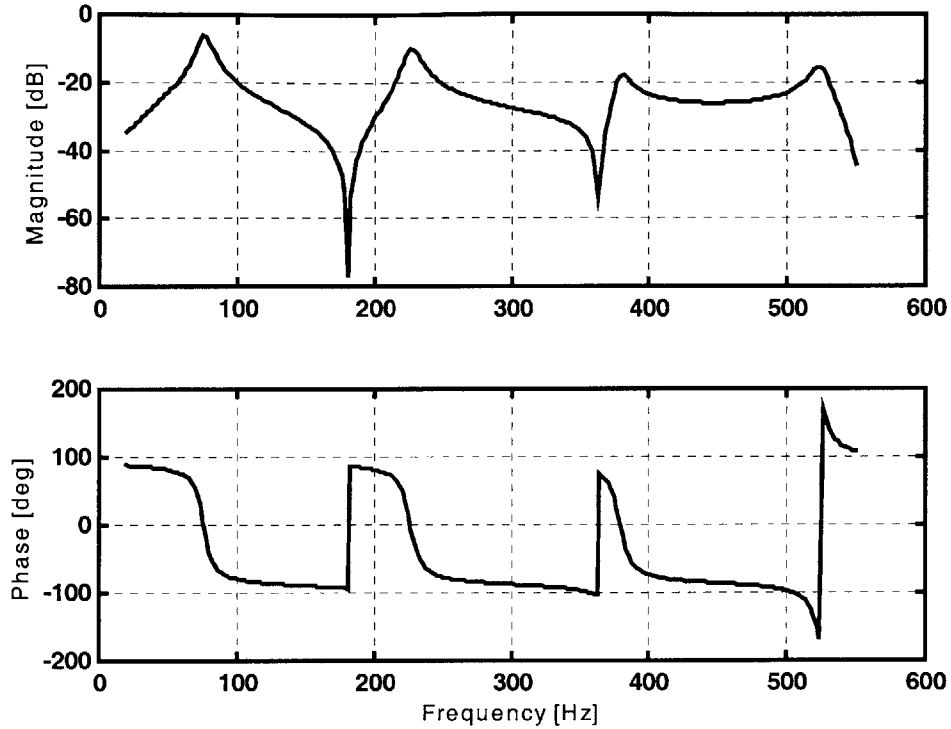
Figure 3.2 - Actuator Injection to AIP Pressure Transfer Function $\left(\dfrac{\psi_{AIP}}{\phi_I} \right)$

3.4   COMPRESSOR EMULATION

The purpose of compressor emulation is to mimic the flow conditions through the UCAV propulsion system. Since the experimental system does not include a compressor, it is proposed to use the actuated injectors to simulate the impedance of the compressor. Therefore, emulating the compressor involves matching impedance of the experimental test section at the AIP to the impedance of a compression system. To perform the compressor emulation the impedances of both the experimental test section and compression system must be calculated. Section 3.4.1 derives the theoretical impedance at the AIP in the experimental test section. Sections 3.4.2 and 3.4.3 derive the theoretical impedance of the compression system. The impedance derivations for both the experimental test section and compression system include actuated injection flow, ϕ_I. The output of the compressor emulation is a feedback transfer function that takes AIP pressure and prescribes the injection velocity

in the experimental setup. To implement this closed-loop emulation, static pressure measurements at the AIP are fed back to the actuators via this transfer function.

3.4.1   IMPEDANCE OF THE EXPERIMENTAL SETUP

To emulate the impedance of a compression system it is necessary to understand how the impedance of the experimental setup changes with the injection mass flow, ϕ_I. The following analysis applies to the experimental configuration used to perform feedback control experiments, see Table 2.1. In this configuration the actuator duct is located directly downstream of the AIP, as shown in Figure 3.1, and the IC is not included.   Equation 3.10 relates the throttle exit flow properties to the AIP flow properties (similar to equation 3.7, except without the IC transmission matrix).   Note that A_I is the ratio of injector area to the duct area.

$$\begin{Bmatrix} \psi_{out} \\ \phi_{out} \end{Bmatrix} = T_{Plug}T_{Act_2}\left(T_{Act_1}T_{IC}\begin{Bmatrix} \psi_{AIP} \\ \phi_{AIP} \end{Bmatrix} + \begin{Bmatrix} 0 \\ A_I \end{Bmatrix}\phi_I \right)$$

(3.10)

The goal of the analysis is to calculate the impedance at the AIP; therefore, equation 3.10 is inverted to isolate the AIP flow properties.

$$\begin{Bmatrix} \psi_{AIP} \\ \phi_{AIP} \end{Bmatrix} = T_{IC}^{-1}T_{Act}^{-1}T_{Plug}^{-1}\begin{Bmatrix} \psi_{out} \\ \phi_{out} \end{Bmatrix} - T_{IC}^{-1}T_{Act_1}^{-1}\begin{Bmatrix} 0 \\ A_I \end{Bmatrix}\phi_I$$

(3.11)

To simplify equation 3.11, the results of the linear algebra matrix multiplications are rewritten as: $T_{IC}^{-1}T_{Act_1}^{-1}\begin{Bmatrix} 0 \\ A_I \end{Bmatrix} = \begin{Bmatrix} E_1 \\ E_2 \end{Bmatrix}$ and $T_{IC}^{-1}T_{Act}^{-1}T_{Plug}^{-1} = \begin{bmatrix} D_{11} & D_{12} \\ D_{21} & D_{22} \end{bmatrix}$. Solving for the flow impedance at the AIP requires knowledge of the exit pressure boundary condition and the transfer function that will be applied from the injectors to AIP pressure.   Since the flow exits into an infinite plenum it is assumed that the exit pressure perturbation is equal to zero ($\psi_{out} = 0$).   Given this boundary condition, the impedance with injection is determined by solving the two equations in equation 3.11 for the three unknowns ϕ_{out}, ψ_{AIP}, and ϕ_{AIP}.

63

$$Z_{D_{inj}} = \frac{\psi_{AIP}}{\phi_{AIP}} = \frac{Z_D}{\left[1-\left(Z_D E_2 - E_1\right)\left(\dfrac{\phi_1}{\psi_{AIP}}\right)\right]}$$

(3.12)

As shown in equation 3.12, $Z_D = \dfrac{D_{12}}{D_{22}}$ is the system impedance at the AIP without injection.

3.4.2   COMPRESSOR IMPEDANCE WITHOUT INJECTION

The lumped compression system model [13], shown in Figure 3.3, consists of four sections: an inlet duct (1-2), a compressor with injectors (2-3), a lumped plenum (3-4), and a throttle (4-5). The reference plane for emulating the compressor is the AIP. Similar to Section 3.4.1, a transmission matrix approach is used to determine the pressure and velocity relationships between the throttle exit and the AIP. With no injection upstream of the compressor, the impedance of the system is found by combining the transmission matrices for the throttle, plenum and compressor.

$$\begin{Bmatrix} \psi_5 \\ \phi_5 \end{Bmatrix} = T_{45} T_{34} T_{23} \begin{Bmatrix} \psi_2 \\ \phi_2 \end{Bmatrix}$$

(3.13)
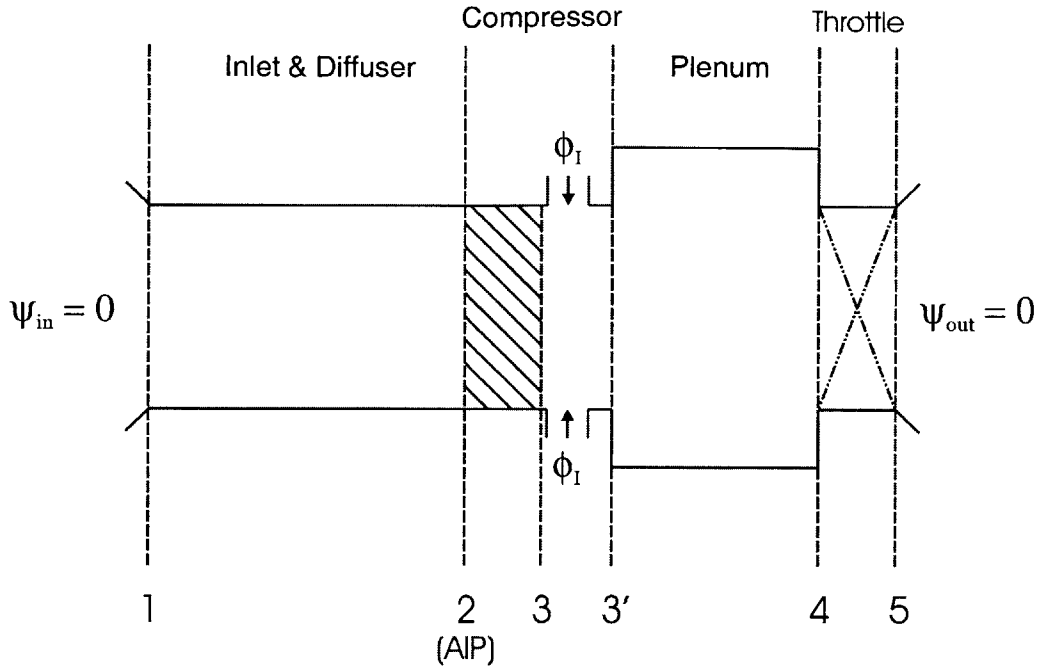
Figure 3.3 – Lumped Compressor Model

Inverting equation 3.13 and applying the exit flow boundary condition allows for the direct solution of the AIP impedance. Equation 3.14 includes a simplified representation of the transmission matrix multiplications, $B(j\omega)$.

$$\begin{Bmatrix} \psi_2 \\ \phi_2 \end{Bmatrix} = T_{23}^{-1} T_{34}^{-1} T_{45}^{-1} \begin{Bmatrix} \psi_5 \\ \phi_5 \end{Bmatrix} = \begin{bmatrix} B_{11}(j\omega) & B_{12}(j\omega) \\ B_{21}(j\omega) & B_{22}(j\omega) \end{bmatrix} \begin{Bmatrix} \psi_5 \\ \phi_5 \end{Bmatrix}$$

(3.14)

The throttle exit boundary, $\psi_5 = 0$, assumes a "pressure release" boundary to the atmosphere [14]. Thus, when solving the system in equation 3.14, the equations for ψ_2 and ϕ_2 reduce to functions of ϕ_5 only. To determine the impedance, simply divide the two equations.

$$Z_C = \frac{\psi_2}{\phi_2} = \frac{B_{12}(j\omega)}{B_{22}(j\omega)}$$

(3.15)

65

3.4.3　COMPRESSOR IMPEDANCE WITH INJECTION

When injection is introduced at the compressor face, as is the case for active control of stall or surge, determining the impedance of the compression system becomes more complicated. The solution to this problem requires an additional piece of information about the system, the compressor face injection transfer function $\left(\dfrac{\phi_I}{\psi_2}\right)$. Solving for the AIP impedance requires knowing the relationship between the flow at station 5 and station 2. The derivation of equation 3.16 is similar to the derivation of equation 3.7.

$$\begin{Bmatrix} \psi_5 \\ \phi_5 \end{Bmatrix} = T_{45}T_{34}\left(T_{23}\begin{Bmatrix} \psi_2 \\ \phi_2 \end{Bmatrix} + \begin{Bmatrix} 0 \\ A_I \end{Bmatrix}\phi_I \right)$$

(3.16)

Inverting equation 3.16 isolates the flow characteristics at station 2, allowing the AIP impedance to be solved. Notice that the B matrix in equation 3.17 is identical to the one used in Section 3.4.2.

$$\begin{Bmatrix} \psi_2 \\ \phi_2 \end{Bmatrix} = T_{23}^{-1}T_{34}^{-1}T_{45}^{-1}\begin{Bmatrix} \psi_5 \\ \phi_5 \end{Bmatrix} - T_{23}^{-1}\begin{Bmatrix} 0 \\ A_C \end{Bmatrix}\phi_I = \begin{bmatrix} B_{11}(j\omega) & B_{12}(j\omega) \\ B_{21}(j\omega) & B_{22}(j\omega) \end{bmatrix}\begin{Bmatrix} \psi_5 \\ \phi_5 \end{Bmatrix} - \begin{Bmatrix} C_1(j\omega) \\ C_2(j\omega) \end{Bmatrix}\phi_I$$

(3.17)

Solving the system of two equations in 3.12, given the boundary condition ($\psi_5 = 0$), leads to an expression for the compression system impedance with injection.

$$Z_{C_{INJ}} = \frac{\psi_2}{\phi_2} = \frac{B_{12}}{B_{22}} + \left(\frac{B_{12}C_2}{B_{22}} - C_1 \right)\left(\frac{\phi_I}{\phi_2} \right) = \frac{Z_C}{\left[1 - \left(Z_C C_2 - C_1 \right)\left(\dfrac{\phi_I}{\psi_2} \right) \right]}$$

(3.18)

Notice that if the injection transfer function is zero, equation 3.18 reduces to equation 3.15, the compression system impedance without injection.

66

3.4.4 TRANSFER FUNCTION FOR COMPRESSOR EMULATION

The purpose of compressor emulation is to simulate the impedance of the compression system in the experimental setup. Thus, the solution to the emulation problem is the transfer function from the AIP pressure to the injection velocity that equates the impedances of the compression and experimental systems. Setting the expression for AIP impedance in the experimental setup, equation 3.12, equal to the compressor impedance, equation 3.18, gives rise to an equation in terms of the AIP pressure to injection transfer function. Equation 3.19 allows for solving this transfer function directly. The results of the compressor emulation are shown in Figure 3.4. In determining this particular transfer function the compressor impedance without injection (Section 3.4.2) is used.

$$\frac{\phi_I}{\psi_{AIP}} = \frac{Z_{C_{inj}} - Z_D}{Z_{C_{inj}}\left(Z_D E_2 - E_1\right)}$$

(3.19)
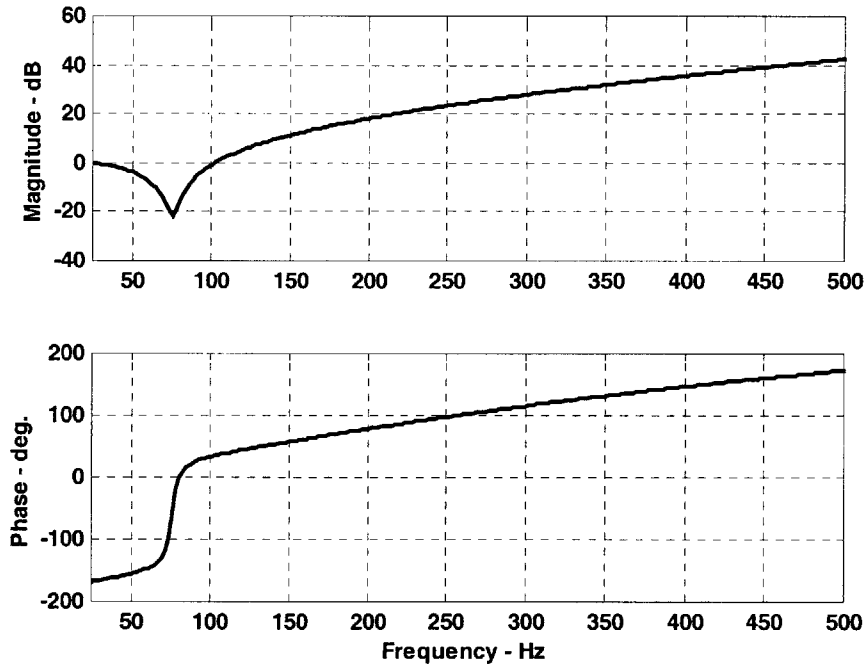
Figure 3.4 – Compressor Emulation Transfer Function $\left(\dfrac{\phi_I}{\psi_{AIP}}\right)$

4 INLET FLOW CHARACTERIZATION

The initial goals of the MIT experiments were validating the experimental setup and gaining understanding of the UCAV inlet flow physics. Before attempting feedback control in the UCAV inlet, it was first necessary to define the cause of and quantify AIP pressure loss and distortion and to understand the effect of downstream actuation. This chapter addresses the experiments and results that aided in preparing for feedback control experiments.

In the absence of a detailed model of the fluid flow in the inlet, the best method for understanding flow separation in the UCAV inlet is by performing flow visualization experiments. Section 4.1 describes the flow visualization technique and the results of the flow visualization experiments. Validating the experimental setup requires repeating the Northrop Grumman experimental results for pressure recovery and comparing MIT's AIP pressure profile to the Northrop CFD solution. Section 4.2 discusses the initial pressure recovery experiments, as well as the effects of actuation on pressure recovery. Section 4.4 focuses on characterizing the unsteadiness at the compressor face. This section describes the creation of a series of bulk total pressure parameters used to characterize the AIP distortion. The last two sections of this chapter discuss the link between the actuators and the sensors in the experimental setup. Section 4.4 lists detailed transfer function data, with modeled fits, while Section 4.5 investigates the cause of the time delays in the experimental setup.

4.1 FLOW VISUALIZATION

Since the AIP pressure deficit (see Figure 4.5) is a result of flow separation from the top surface of the UCAV inlet, the motivation of the flow visualization experiments is to understand the physics of the flow at the separation point. The decision to conduct the flow visualization first among all the UCAV experiments was twofold. The results of the flow visualization aided in determining the best locations for the four separation point hot-film sensors used in subsequent experiments. Second, surface flow visualization experiments using silicone oil are messy. Therefore, it is necessary to schedule the flow visualization experiments before installing the unsteady IC or sensor ring.

69

The flow visualization method consists of applying black, viscous silicon oil to the top and bottom surfaces of the inlet. After applying the oil, the inlet is quickly re-assembled into the experimental setup to ensure evenly distributed oil coverage. The flow visualization experiment requires raising the mass flow through the inlet as quickly as possible to ensure that the oil does not dry before reaching the desired test condition. Similarly, it is important to allow all the oil to dry at the desired mass flow before ending the experiment. Otherwise, the visualization becomes distorted by the characteristics of lower mass flows during compressor shutdown.

The flow visualization results discussed in this section apply to a mass flow of *3.6 lb/s*. At this mass flow, the highest possible for the Northrop Grumman throttle plug, the inlet flow characteristics are the most pronounced. Figure 4.2 shows both halves of the inlet after the flow visualization. The top half, on the right, contains the separated region of the flow; and the direction of the flow is from left to right. This region of separation behaves exactly like the textbook flow reversal (owl-face) shown in Figure 4.1. As shown in this figure, the flow reversal produces twin vortices in the re-circulation zone [9]. The dark line of oil, indicating a line of flow stagnation, lies at the edge of a narrow rectangular cross-section, after which the inlet diffuses into the circular section.
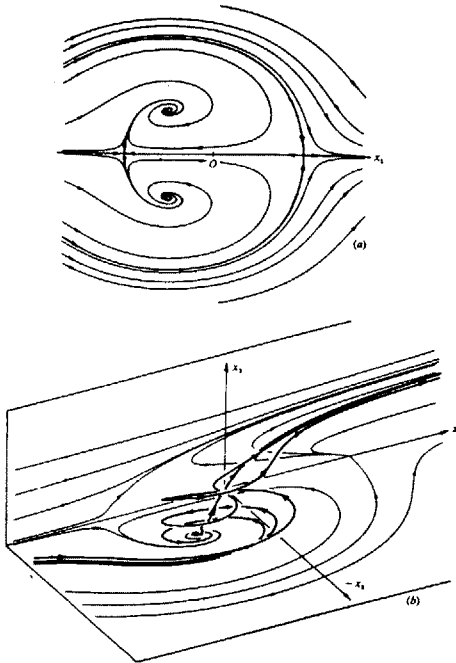
Figure 4.1 – Textbook Owl-Face Separation
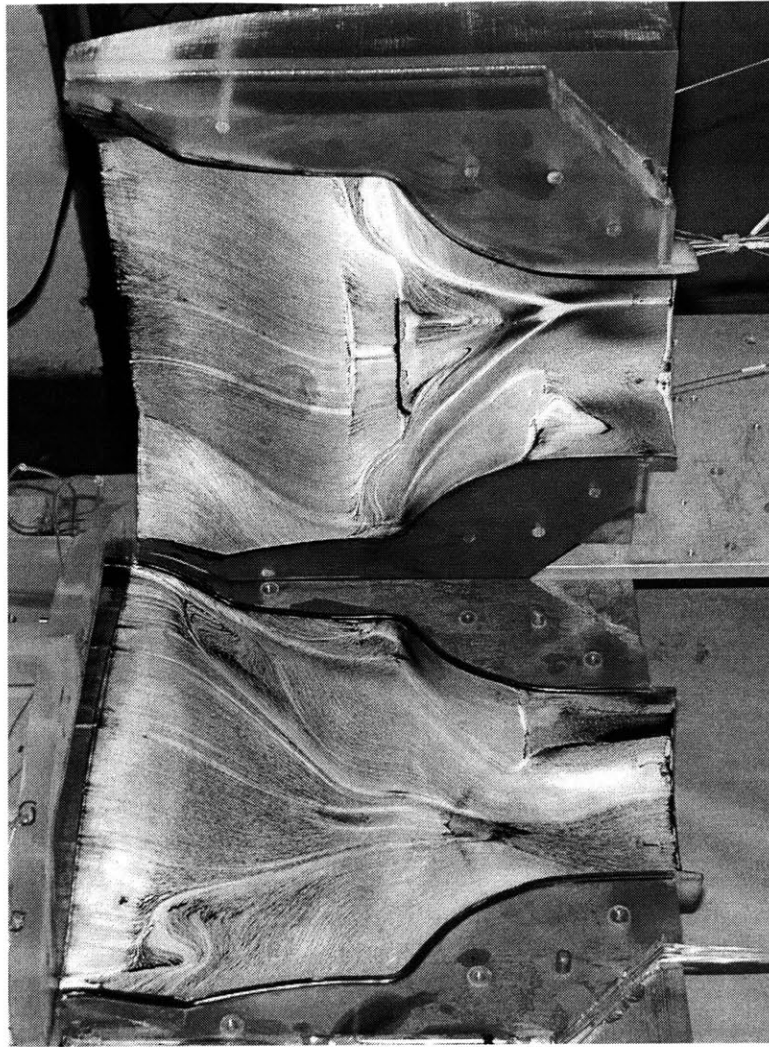
Figure 4.2 – Flow Visualization (Both Halves)

Figure 4.3, created by Michael Brear [9], shows the separated region of the top inlet surface in detail (the flow is from top to bottom in Figure 4.3 and Figure 4.4). The lines superimposed onto Figure 4.3 describe the general characteristics of the flow path. Roughly speaking, the change in inlet area profile, from a long thin rectangular section to a circular section, drives the airflow towards the center-plane of the inlet. This flow impingement at the center of the inlet coupled with the steep slope associated with the curvature of the inlet causes the flow to separate. The separation creates a triangular region of low pressure (see Figure 4.3). The thick black line of oil, characterizes the size of the low-pressure region. The low-pressure region causes flow in the triangular region to reverse direction. The reversed flow meets the forward flow at the edge defined by the dark line of oil. At this edge the reversed flow lifts off the surface and rejoins the core airflow. This description of the

airflow in the separated region corresponds to the textbook "owl-face" flow reversal shown in Figure 4.1. The low-pressure vortices associated with the "owl-face" separation convect downstream and account for the pressure deficit at the top of the AIP. It is postulated that the unsteadiness associated with these vortices correlates to unsteadiness at the AIP. Section 4.3 examines the validity of this postulation.
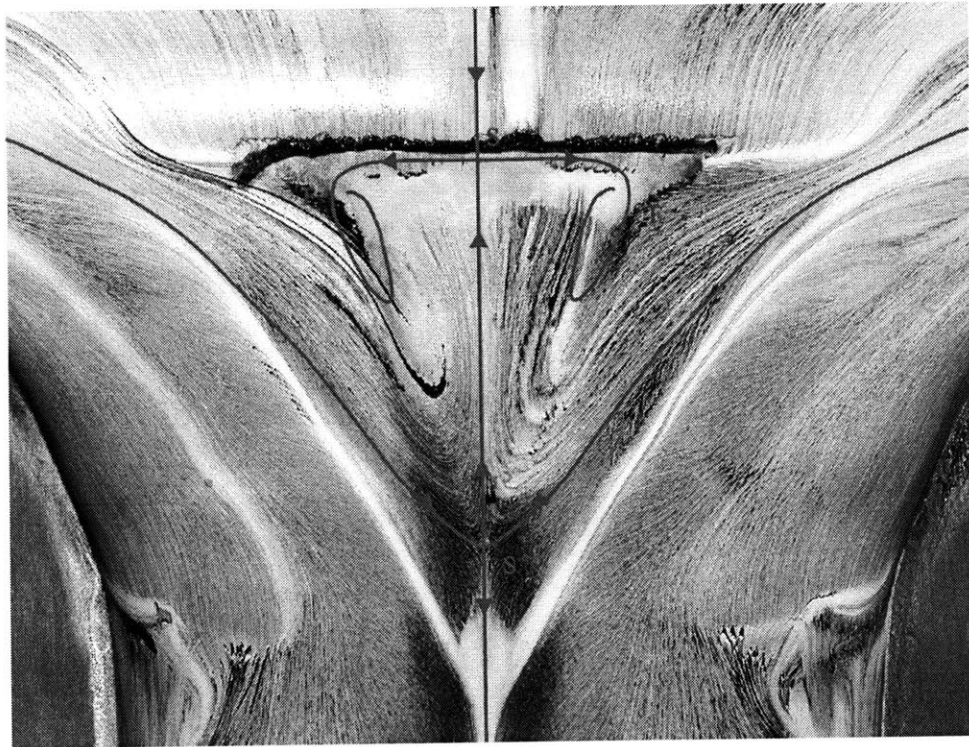
Figure 4.3 – Flow Direction in Flow Visualization Field

These flow visualization results provide significant insight into the nature of the UCAV inlet separation. However, for the purpose of conducting experiments that relate the separation to downstream pressure at the AIP, a means of quantifying inlet separation is required. As discussed in Section 2.2.1.3, hot-film sensors quantify separation by measuring time varying shear stress levels on the inlet surface. In order to capture the unsteady behavior of the inlet separation, the placement of the hot-film sensors is crucial. The results of the flow visualization provide the best guide to placing each sensor. The objective of sensor placement is to find locations that represent areas of highly unsteady activity in the separated region, and define the border of the separated region. By identifying locations of this type and placing sensors there, information about the size and stability of the separated region is obtained. Figure 4.4 identifies the locations of the original four hot-film

sensors based on the flow visualization results. The two "X's" along the centerline aim to capture the stability of the separated flow, while the outer "X's" aim to identify the boundary of the flow reversal. Figure 2.7 shoes the actual placement locations of the hot-film sensors.
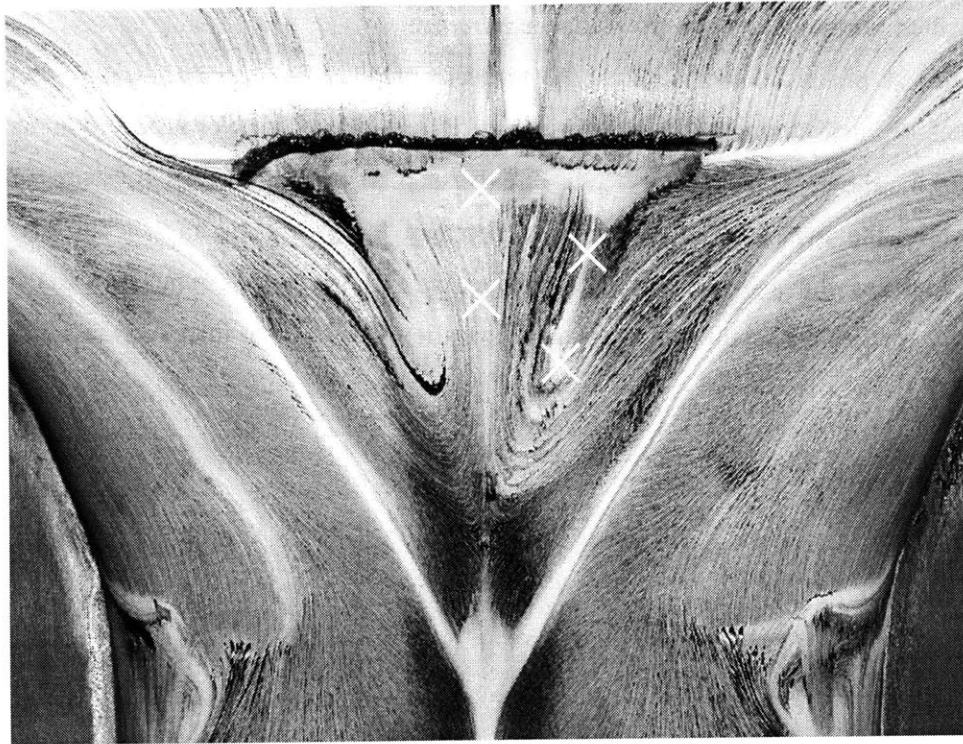
Figure 4.4 – Hot-film Placement in Flow Visualization Field

4.2   EXAMINATION OF INLET PRESSURE RECOVERY

One of the motivations for active control of separation and is to improve the total pressure recovery at the AIP. Based on the correlation between inlet separation and total pressure at the AIP, it is concluded that losses due to separation cause a large low-pressure region located in the top quadrant of the AIP. Therefore, suppression of inlet separation via downstream actuation should increase total pressure in the upper AIP region, thus improving the total pressure recovery at the AIP.

Before it is possible to test if downstream actuation improves pressure recovery, it is necessary conduct experiments that characterize the AIP pressure recovery in the UCAV inlet without actuation. These experiments also serve as an opportunity to validate MIT's experimental setup. There are two means of validating the experimental setup, comparing MIT's results for the AIP total pressure profile

to the Northrop Grumman CFD solutions, and examining the pressure recovery versus inlet mass flow relationship for both Northrop Grumman's and MIT's experimental results.

Creating the total pressure profiles requires measuring the total pressure at each of the forty IC probes, then normalizing each pressure measurement by the stagnation pressure. Figure 4.5 is the MATLAB graphical interpretation of the pressure profile based on the location and magnitude of each pressure measurement. A comparison of Figure 4.5 to the Northrop Grumman CFD results, Figure 4.6, shows consistency between experimental and predicted pressure profiles. Most importantly, the size, location and relative depth of the pressure deficit in the MIT experimental results matches the pressure deficit predicted by the Northrop Grumman CFD analysis. This similarity verifies the relationship between separation from the top inlet surface and loss of pressure at the AIP.
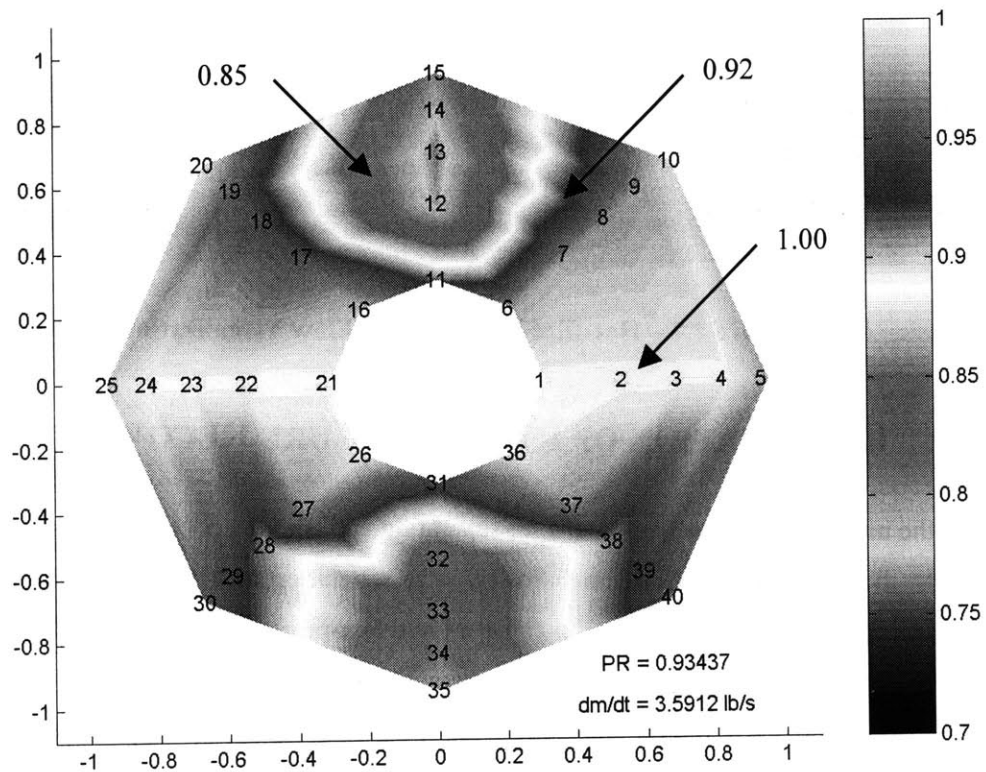
Figure 4.5 – AIP Total Pressure Profile, MIT Experiment
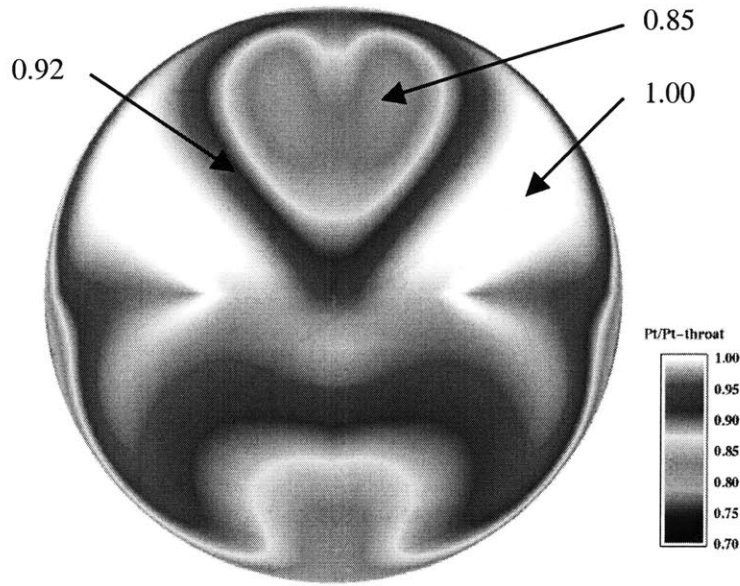
Figure 4.6 – AIP Total Pressure Profile, Northrop Grumman CFD

The second method for validating the experimental setup is the examination of the relationship between inlet mass flow and AIP pressure recovery. As discussed in Section 2.2.1.2, the design of the instrument can layout enables simple calculation of AIP total pressure recovery. Because each probe represents an equal area section of the duct, the AIP pressure recovery is the average of the forty total pressure probes divided by the stagnation pressure.

$$PR = \frac{\sum_{i=1}^{40} P_i}{40 \cdot P_\infty}$$

(4.1)

Figure 4.7 describes the relationship between mass flow and AIP pressure recovery over the mass flow range used in these experiments. As expected, the pressure recovery decreases rapidly with increased mass flow. For comparison, this figure also includes the results of a similar experiment performed at Northrop Grumman. The similarities between the MIT and Northrop Grumman results validate the MIT experimental setup of the UCAV inlet.

75
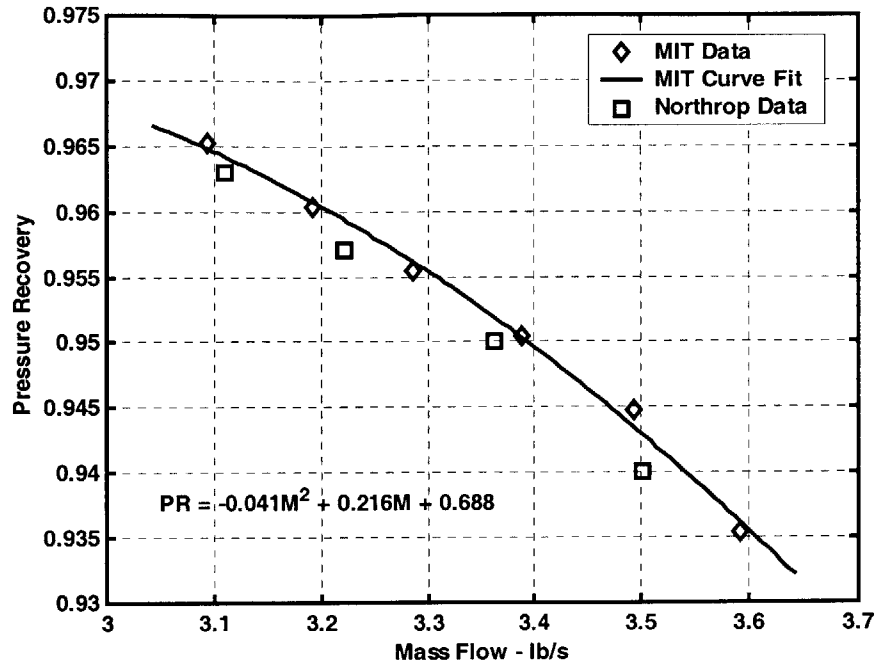
Figure 4.7 – AIP Pressure Recovery as a Function of Mass Flow

4.2.1 THE EFFECTS OF CONSTANT ACTUATION ON PRESSURE RECOVERY

As mentioned earlier, one of the motivations for flow control in the UCAV vehicle is to improve pressure recovery at the AIP. Suppression of separation losses via downstream actuation is a postulated mechanism for improving the pressure recovery. Research by Kwong and Dowling [23] demonstrates the effectiveness that steady wall injection has on the separation boundary layer. However, the research by Kwong and Dowling pertains to injection schemes located at the separation point. The MIT experiments attempt to demonstrate the same suppression of separation loses using compressor face actuation rather than separation point actuation. The simplest test in determining if downstream actuation suppresses separation is to measure pressure recovery for various constant actuation frequencies. This is an open-loop experiment performed with the aim of reducing separation via a non-linear acoustic interaction within the boundary layer. The goal of this experiment is to identify a frequency (or set of frequencies) that causes a noticeable change in pressure recovery. For this experiment the actuator supply pressure is *40 psi* and the actuator command signal is an *8 V* peak-to-peak sinusoid, both maximum conditions for actuation. Also, the location of the actuator duct is downstream of the IC. The optimal location of the actuator duct is

76

directly upstream of the IC, but the impingement from the injectors causes blockage thus distorting the total pressure measurements.

Unfortunately, as seen in Figure 4.8, there are no frequencies that increase (or decrease) the pressure recovery by an appreciable amount. The *0.5%* differences in pressure recovery can be accounted for by measurement error. Based on *3.2 lb/s* results, it is tentatively concluded that there is no acoustic frequency that couples into the separation physics. However, these results do not eliminate the possibility of separation suppression via closed-loop feedback control. Unfortunately, given the experimental setup at MIT, closed loop control experiments with the IC in place were unsuccessful. With the actuator duct located downstream of the IC (injectors *10.5 in.* from the AIP), the actively controlled actuators had no appreciable affect on the AIP total pressure measurements. This could be due to the additional time delay associated with the propagation of the acoustic waves through the IC. Section 4.6 contains an analysis of these time delays, and discusses their effects on feedback control. Other explanations such as, rake impedance or variations in IC duct geometry could influence the effectiveness of feedback control using the IC. Unfortunately, these are only postulations as to the problem, and the cause of this phenomenon is still unknown.
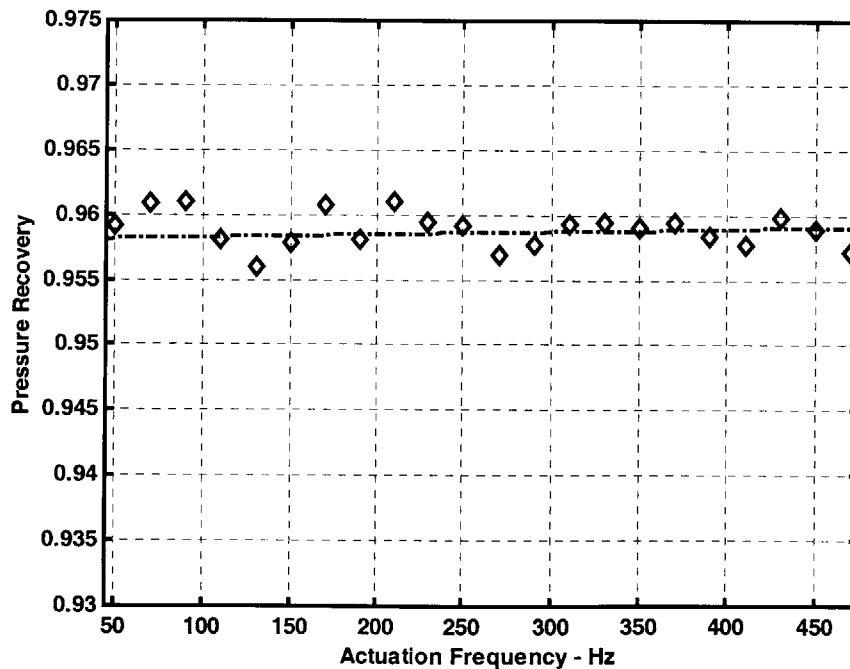
Figure 4.8 – AIP Pressure Recovery as a Function of Actuation Frequency (~3.2 lb/s)

77

4.3   CHARACTERIZATION OF UNSTEADINESS

One of the most important experiments in this chapter was performed to study the relationship between unsteady measurements at the separation point and at the AIP. The goal of this experiment is to determine if there is link between separation point and AIP unsteadiness. The experiment was performed at a mass flow of *3.1 lb/s* without any blowing from the actuators. Twelve seconds of data at *20 kHz* were recorded for the hot-film and the three total pressure probes located in positions 13, 23 and 83 of Figure 2.5.

From this data set, the cross-correlation spectral analysis for each combination of these four probes was performed.   The outputs of these cross-correlation analyses are transfer function plots with coherence, and cross-correlation plots.   Figure 4.9 - Figure 4.12 show the coherence and time lag results of four of the six possible cross-correlation analyses. The unsteady response of probe 23 has no correlation to either the hot-film, probe 13 or probe 83. Figure 4.9 illustrates the lack of coherence in the transfer function from the hot-film to probe 23.   The low coherence is the result of low unsteadiness levels at the top-center region of the AIP. The absence of unsteadiness at probe 23 is consistent with the previous understanding of the pressure deficit in the upper quadrant of the AIP. The unsteadiness associated with the pressure deficit is concentrated around the edge of the deficit, while the center of the deficit experiences lower levels of unsteadiness.   The unsteadiness concentrated at the left and right sides of the pressure deficit is attributed to a lateral oscillation of the deficit.   However, the cause of the oscillations needed to be determined.   The spectral analysis between probes 13 and 83 illuminates a characteristic frequency of oscillation for the deficit.   Figure 4.12 shows the coherence and cross-correlation results between probes 13 and 83.   This transfer function illustrates a high coherence at low frequencies and at *500 Hz*.   The high correlation at low frequencies might be due to bulk acoustic modes in the inlet.   It is believed that the activity at *500 Hz* is a result of a characteristic shedding frequency at the separation point.

It is postulated that the lateral oscillation of the pressure deficit is the result of vortices that convect downstream and collide with the AIP. The frequency at which these vortices shed is assumed to be *500 Hz* because of the coherence levels in the hot-film to AIP transfer functions (see Figure 4.10 and Figure 4.11). In both cases, the coherence at *500 Hz* exceeds *0.5* (which is high considering the noise levels of the system) and the transfer functions show slight peaks. This confirms the existence of a *500 Hz* shedding phenomenon from the separation point to the AIP. An examination of the cross-

correlation versus lag time plots indicates that time delay from events at the separation point to the AIP is slightly less than *1.00 ms*. This time delay corresponds to the calculated convection time from separation point to the AIP in Section 4.6 (*0.75 ms.*). The peak cross-correlation of probe 13 is negative and the cross-correlation of probe 83 is positive.

Based on the correlation of the hot-film and total pressure unsteadiness, two theories were postulated to explain the motion of the pressure deficit. The first involves an oscillatory side-to-side motion of the separated core flow as it travels from the separated region to the AIP. The second theory is that alternating vortices shed from the separation point and arrive at the left and right sides of the AIP. To determine which of these conjectures is more descriptive of the actual system, movies of the unsteady AIP total pressure were generated. If the first theory were true, then one would expect to see the size of the pressure deficit remain constant as it oscillates across the AIP center-plane. However, the movies indicate that the pressure deficit expands and contracts as it shifts from the left to right sides of the AIP center-plane. The expansion and contraction of the deficit supports the theory that the deficit is the result of alternating vortices shedding from the separations point.

Characterization of unsteadiness between the hot-film and AIP sensors is necessary to determine the feasibility of feed-forward control in the experimental test section. The coherence levels shown in Figure 4.10 and Figure 4.11 also demonstrate that it is possible to construct a transfer function from the separation point to the AIP. These transfer functions are crucial for the development of a feed-forward control law, discussed in Section 5.3. Feed-forward control uses a reference sensor located upstream to predict the unsteadiness at a downstream position. Then, based on the reference signal, the controller attempts to reduce another independent measurement downstream. In these experiments, feed-forward control involves using the hot-film sensors to predict and reduce the unsteadiness at the AIP. Without adequate hot-film to AIP transfer functions feed-forward control is impossible.
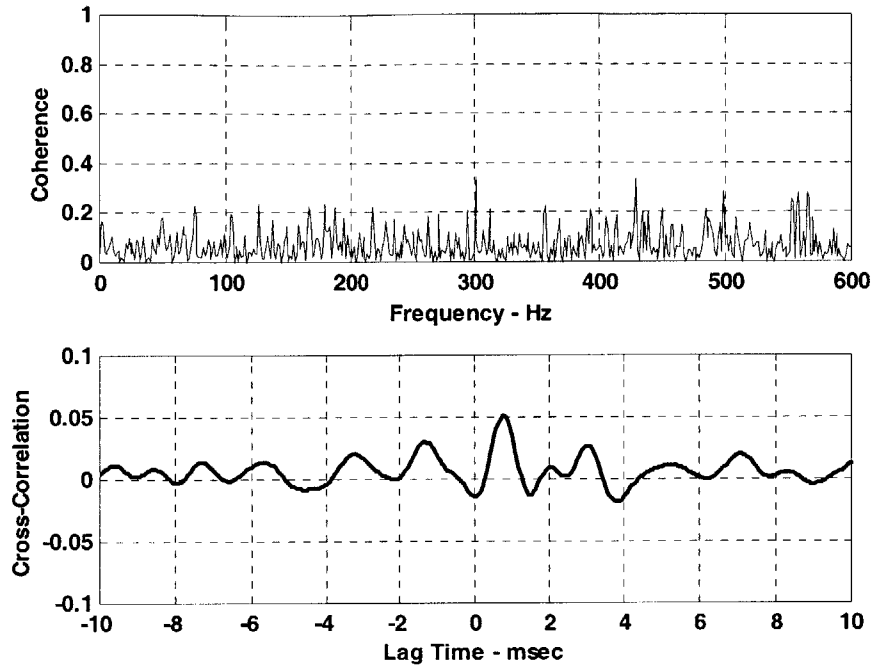
Figure 4.9 – Characterization of Coherence and Cross-Correlation Between Hot-film Measurements and AIP Total Pressure Probe 23
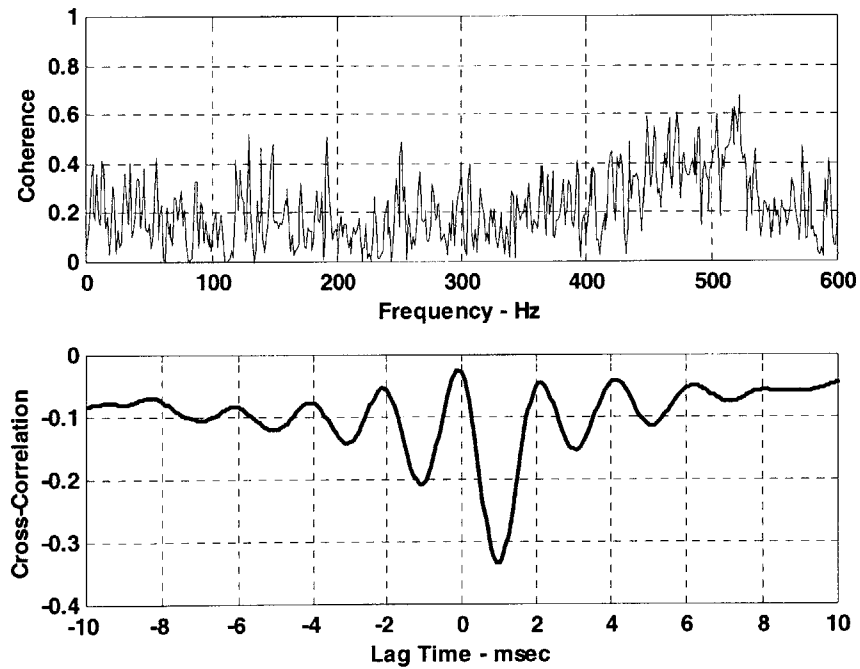
Figure 4.10 – Characterization Coherence and Cross-Correlation Between Hot-film Measurements and AIP Total Pressure Probe 13
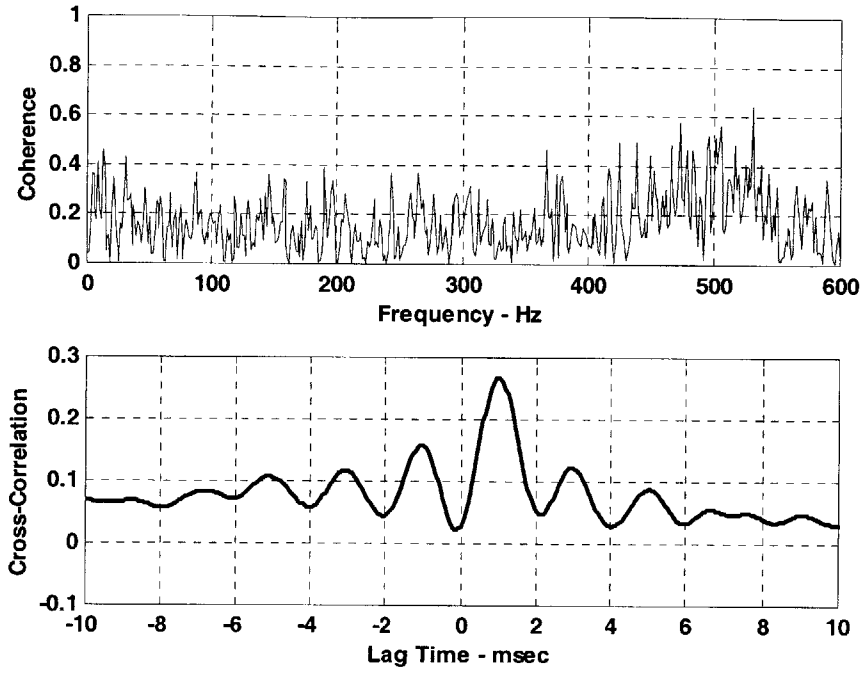
Figure 4.11 – Characterization of Coherence and Cross-Correlation Between Hot-film
Measurements and AIP Total Pressure Probe 83
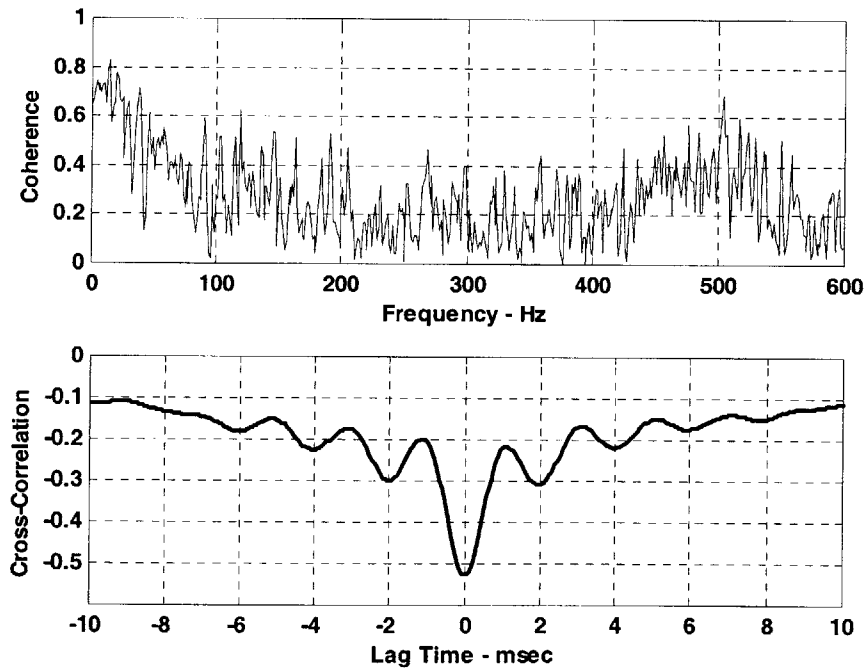
Figure 4.12 – Characterization of Coherence and Cross-Correlation Between AIP Total Pressure
Probe 13 and AIP Total Pressure Probe 83

4.4 DEVELOPMENT OF BULK PARAMETERS

Along with improving pressure recovery, the goal of implementing flow control in the UCAV design is reduction of distortion unsteadiness at the AIP. The region where the distortion is highest is characterized by a pressure deficit located at the top-center of the AIP (see Figure 4.5). The criterion for improving AIP distortion is reduction of the unsteadiness associated with the pressure deficit. The unsteadiness associated with the pressure deficit was illuminated by a series of animated movies depicting the AIP pressure profile over time. These movies[6], which look identical to Figure 4.5 except animated, illustrate that the pressure deficit both expands/contracts and oscillates left and right over time. These movements, especially changes in size, can have negative effects on the compressor stability and stall margins. For more information pertaining to the effects of inlet distortion on compressor performance refer to AIR-1419: Inlet Total-Pressure-Distortion Considerations for Gas-Turbine Engines [21]. Thus, the motivation for using feedback flow control (Chapter 5) to reduce flow unsteadiness is to improve compressor performance.

Active control of the AIP unsteadiness first requires characterizing the distortion. The most accurate means of measuring unsteadiness at the AIP are unsteady total pressure sensors. The unsteady IC gives the most complete description of the AIP total pressure. The IC is equipped with 40 probes capable of gathering a complete set of unsteady data. The IC was crucial in generating the unsteady movies used to identify the unsteadiness associated with the pressure deficit. However, in order to develop a control law that is simple enough to implement it is necessary to reduce the multiple unsteady total pressure measurements into a few bulk parameters that best characterize the AIP distortion. The bulk parameter approach aides the implementation of feedback control experiments by reducing the system from a multiple input/output (MIMO) system to a simplified single input/output (SISO) system. The bulk parameters chosen for the feedback control experiments derive from ARP-1420 [12] calculations and are linear combinations of the AIP total pressure measurements.

Based on the movements of the pressure deficit in the AIP movies, the bulk parameters were chosen to describe circumferential unsteadiness (i.e. expansion/contraction circumferentially). To perform

---

[6] Dr. Jim Paduano maintains the unsteady AIP movies. For obvious reasons they cannot be included in this body of work.

the circumferential calculations it is necessary to choose a radial ring of probes or combination of rings to characterize the circumferential distortion. The first set of bulk parameters were based on measurements from the unsteady IC. This set aided in identifying the character of the bulk parameters without feedback control. Initially, the bulk parameters were calculated from the entire set of pressure measurements per ARP-1420 [12].

The first bulk parameter is the extent of the distortion, Θ. The extent, described by equation 4.2 and Figure 4.13, is the angular portion of the distortion in which the total pressure is less than the average circumferential pressure. Figure 4.13 shows the graphical basis for determining θ_2 and θ_1 based on the average total pressure of each rake. The units for the extent are degrees or radians.

$$\Theta = \theta_2 - \theta_1$$

(4.2)

The second bulk parameter is the magnitude of the pressure deficit, A. The definition of this parameter, equation 4.3, is area of the deficit under the total average pressure in the angular range of the extent as defined in Figure 4.13.

$$A = \int_{\theta_1}^{\theta_2} [P_{AVG} - P(\theta)]d\theta$$

(4.3)

The last bulk parameter defines the centroidal location of the pressure deficit, Λ. This parameter is determined by calculating the pressure weighted angular average over the upper half of the AIP. Due to symmetry at the AIP, this parameter should oscillate about the vertical centerline of the AIP ($90°$).

$$\Lambda = \frac{\int_0^\pi \theta \cdot P(\theta)d\theta}{\int_0^\pi P(\theta)d\theta}$$

(4.4)

83
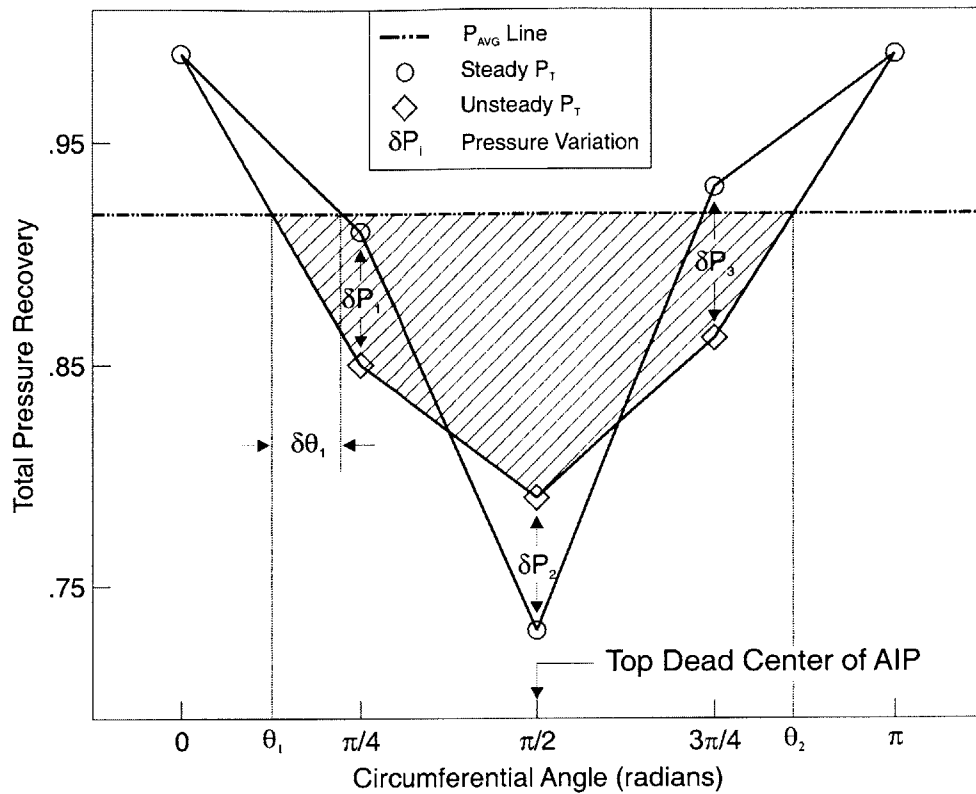
Figure 4.13 – ARP-1420 Distortion Characterization

The ultimate goal of creating the bulk parameters is to identify a quantity worth reducing via feedback control. Unfortunately, due to the length of the unsteady IC, which displaces the actuators too far downstream of the AIP to have an appreciable effect, a new approach for characterizing the AIP bulk parameters is necessary. During the experiments involving the unsteady IC, many probe combinations were tested to identify the optimal locations for the probes required to describe the character of the pressure deficit unsteadiness. In general, the probes with the highest RMS values were chosen. Based on these experiments, the optimal locations for the probes are the three middle rings of rakes 1, 2, and 8 (see Figure 2.5). From these findings, it was deduced that the bulk parameters can be calculated by locating three probes in the approximate positions described above. This experimental configuration is made possible by replacing the unsteady IC with the sensor ring. The three probes mounted in the sensor ring are located in the approximate locations of probes 13, 23 and 83 in Figure 2.5.

The only difference between the IC and sensor ring configurations is that the IC has the capability of measuring both steady and unsteady total pressure simultaneously, while the sensor ring probes only measure unsteady total pressure. Because the unsteady transducers in both the IC and sensor ring

84

have high drift rates they are A/C coupled during the experiments. Since the IC is equipped with steady pressure probes, the D/C portion of total pressure is recovered by adding the steady pressure measurements to the A/C coupled data. However, the sensor ring does not have this capability. Therefore, the steady pressure of the sensor ring probe locations is estimated based on previous experiments. This discrepancy does not affect the definitions of the bulk parameters, however, it does affect the method in which they are calculated. For the sensor ring configuration, the technique of linearizing the bulk parameters is applied to remove the dependency on the steady pressure. This technique requires the derivation of constant coefficient multipliers for each unsteady pressure measurement. Each bulk parameter then becomes the summation of these coefficients multiplied by the appropriate unsteady pressure measurement. The derivation of the linearized bulk parameters is discussed in depth in Appendix C.

4.5 TRANSFER FUNCTIONS

This section describes the experimental creation of transfer functions from the actuators to the sensors within the MIT experimental setup. The sensors include the hot-films and the AIP total pressure transducers. The measurements from the AIP total pressure transducers constitute the bulk parameters. These transfer functions serve two purposes. First, they aid in understanding the acoustic properties of the experimental setup. Most importantly, though, they enable the creation of feedback control laws designed to reduce unsteadiness.

The experimental procedure for generating transfer functions is to record actuator and sensor data for various constant frequency excitation signals. The set of constant frequencies used to create these transfer functions ranges from *50 Hz* to *490 Hz* in *20 Hz* intervals. The actuator pressure and command voltage for these experiments are set at the maximum conditions of *40 psi* and *8 V* peak to peak, respectively. Once the data for each frequency is taken, then creation of the transfer function involves only data reduction. MATLAB is used to perform spectral analysis of an input (actuator command voltage) and output (hot-film or bulk parameter) signal. The spectral analysis returns the transfer function from input to output over the entire frequency range. The spectral analysis also returns the coherence level at each frequency. To build a transfer function over the desired actuator range, it is necessary to extract the transfer function data from each constant actuation frequency data set whose coherence is greater than *0.5*. Therefore, the total transfer function is the concatenation of

every point in each individual transfer function whose coherence meets this requirement. Table 4.1 is the legend used to identify the coherence of each experimental data point in the transfer functions.

Symbol	Coherence	Symbol	Coherence
+	0.50 – 0.55	✳	0.75 - 0.80
◁	0.55 - 0.60	Δ	0.80 - 0.85
▷	0.60 – 0.65	❏	0.85 - 0.90
×	0.65 – 0.70	O	0.90 - 0.95
*	0.70 - 0.75	◊	0.95 - 1.00

Table 4.1 – Coherence Level Symbols

The second task in characterizing the transfer functions is to create a model to fit each set of data points. The method used to fit the modeled transfer functions is a zero-pole-gain technique, which involves selecting the poles, zeros and gain of the transfer function. The equation that governs the modeled transfer function is equation 4.5, where z_i are the zeros, p_i are the poles, k is the gain, and τ is the time delay. Equation 4.5 describes the transfer function in the frequency domain, where $s = j\omega$.

$$G(s) = \frac{k \cdot \sum_i (s - z_i)}{\sum_i (s - p_i)} e^{-s\tau}$$

(4.5)

4.5.1 Transfer Function from Actuators to Bulk Parameters

The first set of experimental transfer functions (TF) relates the actuator command voltage to the bulk parameters (BP), extent and magnitude. Figure 4.14 shows the experimental data and model curve fit of the actuator to magnitude transfer function, and Table 4.2 lists the model parameters. Figure 4.15 shows the experimental data and model curve fit of the actuator to extent transfer function, and Table 4.3 lists the model parameters. Because the bulk parameters derive from the same AIP total pressure measurements, both the extent and magnitude transfer functions must have the same poles and time delay. However, the zeros for each transfer function can vary from extent to magnitude. Despite the flexibility in the zeros, both bulk parameters transfer functions contain a non-minimum phase zero at approximately *190 Hz*. This zero corresponds to the first zero predicted by the 1-D acoustic model derived in Chapter 3. Figure 3.2 shows the acoustic transfer function from the actuator injection

velocity to the AIP pressure. Although the bulk parameters are circumferential quantities and the acoustic model takes into account only axial perturbations, the similarity between the theoretical model and the experiment-based model indicates that there is some validity to the theoretical model.
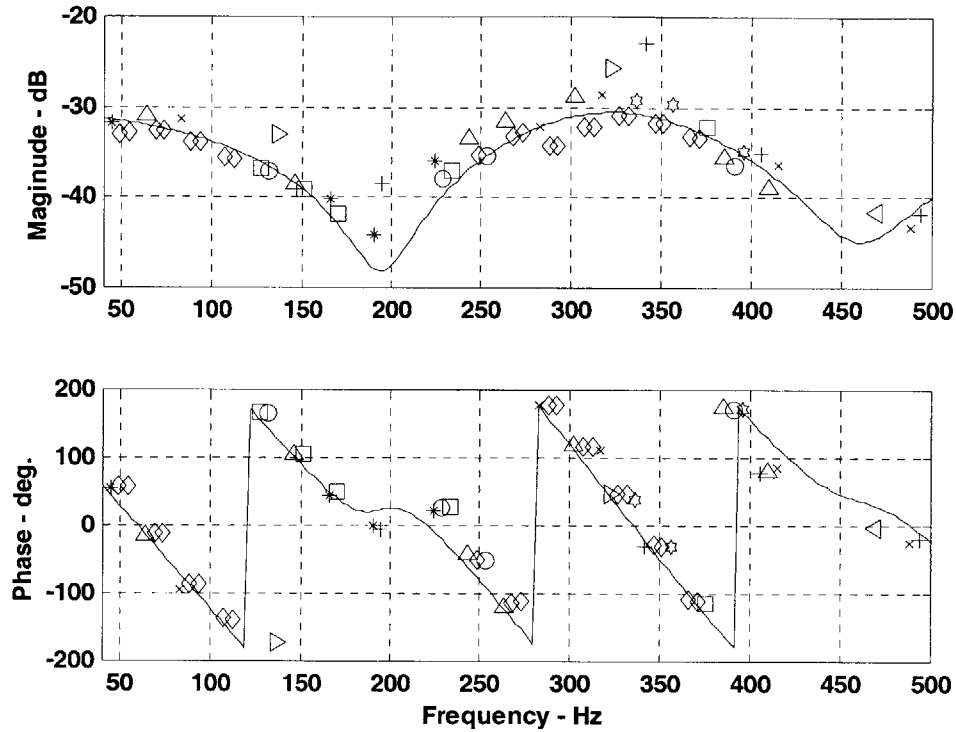
Figure 4.14 – Actuator Command Voltage to Magnitude BP (psi-rad/V) TF

Parameter	Value	Description
$G(s)$	N/A	Transfer Function
s	$j \cdot \omega$	Laplace Variable
p_1	-1571 rad/s [-250 Hz]	1st Zero
$p_{2,3}$	-565 ± j·2011 rad/s [-90 ± j·320 Hz]	Complex Zero Pair
$z_{1,2}$	-94 ± j·1225 rad/s [-15 ± j·195 Hz]	1st Complex Pole Pair
$z_{3,4}$	-157 ± j·2890 rad/s [-25 ± j·460 Hz]	2nd Complex Pole Pair
τ	7.750 ms.	Model Time Delay
k	-1.5475 x 10⁵	Gain

Table 4.2 – TF Parameters: Actuator Command Voltage to Magnitude BP
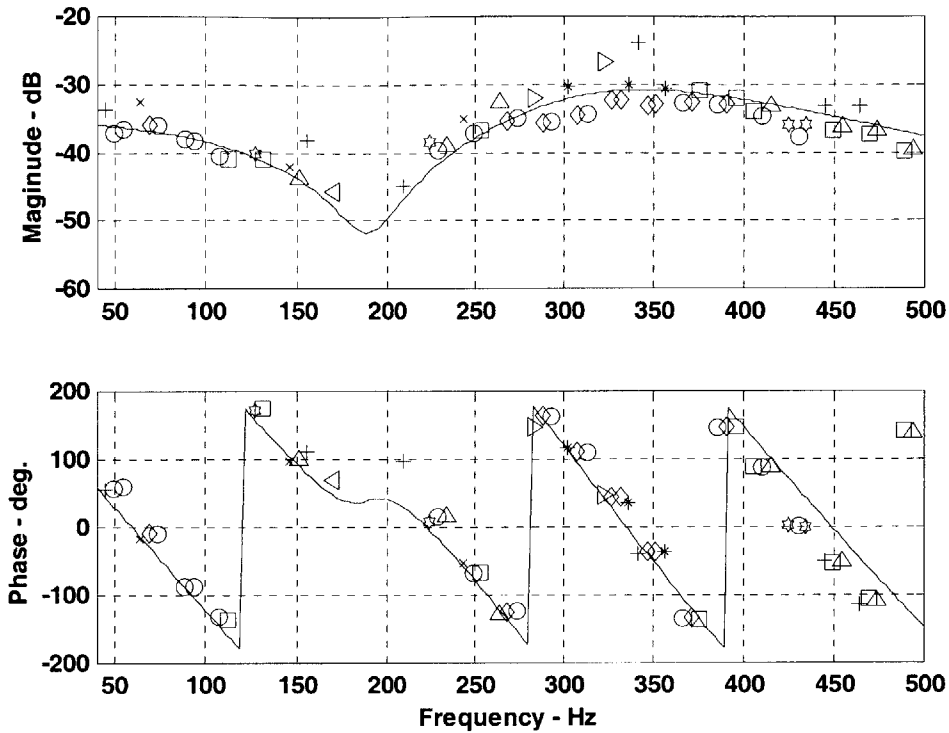
Figure 4.15 – Actuator Command Voltage to Extent BP (rad/V) TF

Parameter	Value	Description
$G(s)$	N/A	Transfer Function
s	$j \cdot \omega$	Laplace Variable
p_1	*-1571 rad/s [-250 Hz]*	1st Pole
$p_{2,3}$	*-565 ± j·2011j rad/s [-90 ± 320 Hz]*	Complex Pole Pair
$z_{1,2}$	*-94 ± j·1194j rad/s [-15 ± 190 Hz]*	1st Complex Zero Pair
$z_{3,4}$	*-440 ± j·4084j rad/s [-70 ± 650 Hz]*	2nd Complex Zero Pair
τ	*7.750 ms.*	Model Time Delay
k	*-4.7199 x 10^{-6}*	Gain

Table 4.3 – TF Parameters: Actuator Command Voltage to Extent BP

88

4.5.2   TRANSFER FUNCTION FROM HOT-FILM TO ACTUATORS

The second experimental transfer function relates the actuator command voltage to the hot-film sensor response. Figure 4.16 shows the experimental data and model curve fit of the actuator to hot-film transfer function, and Table 4.4 lists the model parameters. Because of the lower signal-to-noise ratio of the hot-film sensor, there are fewer data points in the low frequency range for the hot-film transfer function compared to the bulk parameters transfer functions. Also, the data points in the lower range are more scattered. The cause of both of these effects could be the increased distance between the hot-films and actuators compared to the AIP and actuators. The increased distance corresponds to an increase in the time delay (see Section 4.6). An Increase the time could reduce the coherence between the actuators and the sensors. This is a plausible explanation for the reduced coherence of experimental data points in the hot-film transfer function. However, this reduction could also indicate that the hot-film response is less correlated to the actuators than the bulk parameters.
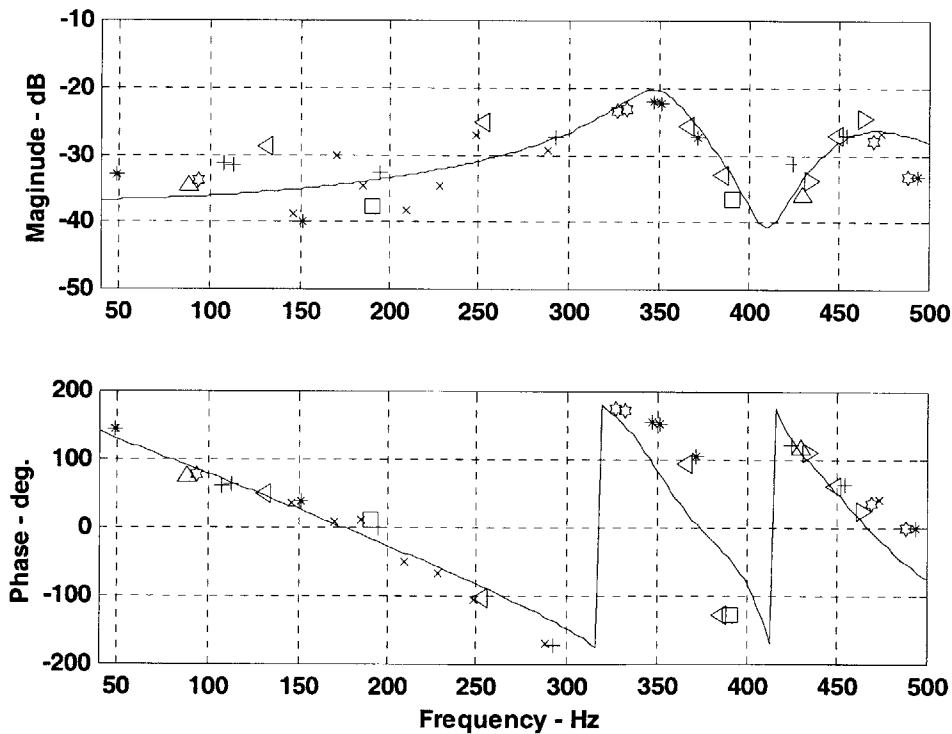
Figure 4.16 – Actuator Command Voltage to Hot-film (V/V) TF

Parameter	Value	Description
$G(s)$	N/A	Transfer Function
s	$j \cdot \omega$	Laplace Variable
z_1	-3143 rad/s [-500 Hz]	1st Zero
$z_{2,3}$	63 $\pm$ j·2576 rad/s [10 $\pm$ j·410 Hz]	Complex Zero Pair
$p_{1,2}$	-126 $\pm$ j·2199 rad/s [-20 $\pm$ j·350 Hz]	1st Complex Pole Pair
$p_{3,4}$	-220 $\pm$ j·2890 rad/s [-35 $\pm$ j·460 Hz]	2nd Complex Pole Pair
τ	3.000 ms.	Model Time Delay
k	-27.9165	Gain

Table 4.4 – TF Parameters: Actuator Command Voltage to Hot-film

4.6 TIME DELAY ANALYSIS

The transfer functions in Sections 4.3 and 4.5 include time delays in their models. These time delays are the summation of the time delays for the various different elements that comprise the total transfer function. The sources of times delay in MIT's experimental setup are; the actuator servo motor, the generation of the acoustic wave, the propagation time for an acoustic wave to travel a distance, the unsteady instrumentation and the data acquisition. For the actuator servomotor, acoustic wave propagation, instrumentation and the data acquisition, the time delays are known. However, the time delay associated with the injector generating an acoustic wave is not quantified. Table 4.5 lists all of the sources of time delay in the feedback control experimental setup.

Time Delay	Hot-film	AIP Bulk Parameter	Description
τ_{act}	0.150 ms	0.150 ms	Actuator Servo Motor Delay (see Table 2.4)
τ_{awg}	N/A	N/A	Acoustic Wave Generation Delay
τ_{prop}	1.416 ms, or 2.715 ms	0.737 ms, or 2.036 ms	Acoustic Wave Propagation Delay (see Table 4.6)
τ_{sensor}	~0.00 ms	0.272 ms	Delay in Sensor Ring Probe (see Table 4.6)
τ_{da}	0.050 ms	0.050 ms	Data Acquisition Time Delay (1 Sample @ 20 kHz)

Table 4.5 – Time Delays in the Feedback Control Experimental Setup

90

4.6.1 TIME DELAYS ASSOCIATED WITH ACOUSTIC WAVE SPEED

Parameter	Value	Description
M	0.6	Average Inlet Mach Number
L_1	6.35 cm	Distance from Actuator Injector Hole to Actuator Duct Flange
L_2	3.30 cm	Axial Length of Sensor Ring
L_3	20.32 cm	Axial Length of Instrument Can
L_4	8.90 cm	Distance from Hot-film to AIP
L_5	8.89 cm	Length of Sensor Ring Total Pressure Probe
γ	1.4	Ratio of Specific Heats
a_i	$a_0\sqrt{1-\dfrac{\gamma-1}{2}M^2} = 327$ m/s	Speed of Sound in Actuator Duct
$\bar{u}_U$	$a_i(1-M) = 131$ m/s	Upstream Acoustic Wave Velocity
$\bar{u}_D$	$a_i(1+M) = 523$ m/s	Downstream Acoustic Wave Velocity
$\hat{u}$	$a_iM = 192$ m/s	Uniform Flow Velocity in Inlet
τ_A	$\dfrac{L_1+L_2}{\bar{u}_U} = 0.737$ ms	Time Delay to from Actuator to AIP thru the Sensor Ring
τ_B	$\dfrac{L_1+L_3}{\bar{u}} = 2.036$ ms	Time Delay to from Actuator to AIP thru the Instrument Can
τ_C	$\dfrac{L_1+L_2+L_4}{\bar{u}_U} = 1.416$ ms	Time Delay to from Actuator to Hot-film thru the Sensor Ring
τ_D	$\dfrac{L_1+L_3+L_4}{\bar{u}_U} = 2.715$ ms	Time Delay to from Actuator to Hot-film thru the Instrument Can
τ_E	$\dfrac{L_4}{\hat{u}} = 0.464$ ms	Time Delay to from Hot-film to AIP
τ_F	$\dfrac{L_5}{a_i} = 0.272$ ms	Time Delay in the AIP Total Pressure Probes

Table 4.6 – Acoustic Wave Time Delay Analysis

In low Mach number flows the average flow velocity is much smaller than the speed of sound. As a result the time associated with an acoustic wave propagating over a certain distance is much smaller than convection for the flow to travel the same distance. However, for high Mach number experiments, such as the UCAV inlet, acoustic and convection time delays are the same order of magnitude. As seen in Table 4.6, the velocity of an acoustic wave traveling upstream in the inlet is a

function of both the speed of sound and the Mach number. As Mach number increases the acoustic wave speed decreases, and the time delay increases. Table 4.6 describes the calculation for the time delays associated with acoustic propagation and flow convection.

The results presented in Table 4.6 give useful insight into understanding the transfer functions and designing control laws. The first interesting result is the time delay from the hot-film to the AIP total pressure transducers. This delay (~ 0.75 ms.) is the combination of the convective time from the hot-films to the AIP, τ_E, and the time delay in the pressure probes, τ_F. This time delay matches the experimental results illustrated in the cross-correlation plots of Figure 4.10 and Figure 4.11. These cross-correlation plots show a time delay of approximately 1.00 ms.

The second interesting result from this analysis is the amount of time delay associated with the using the IC compared to using the sensor ring. The IC accounts for an additional 1.30 ms. of time delay in the transfer function from the actuators to the total pressure or hot-film sensors. This additional time delay when using the IC configuration is viewed as a possible cause for the ineffectiveness in implementing feedback control.

The most interesting result from this analysis is the implication of time delay on feed-forward control laws. Feed-forward control, discussed in Section 5.3, uses an upstream measure of the flow unsteadiness to predict the unsteadiness at the AIP. The control law uses this "predicted" quantity to try to reduce unsteadiness at the AIP. Using an upstream reference measurement usually allows for enough lead-time in the system to design a controller that cancels the unsteadiness downstream. However, the high Mach number of the UCAV inlet flow causes the convection time from the hot-films to the AIP to be less than the acoustic propagation time from the actuators to the AIP. As a result, the advantage of using feed-forward control is negated. However, this problem only appears in this experimental setup because the inlet is one-sixth-scale. In a full-scale inlet setup the convection time would increase by a factor of six (~2.80 ms.), while the acoustic propagation time would remain the same. Therefore, in a full-scale configuration, it may still be possible to use feed-forward control.

5 ACTIVE FLOW CONTROL

The goal of this research is to develop and test a series of control laws to actively control unsteadiness, induced by separation, in the UCAV inlet. The mechanism used to control unsteadiness is the generation of planar acoustic waves by four actuators located downstream of the inlet. The actuators create acoustic waves by modulating airflow through injectors over a frequency range of *50-500 Hz*. A description of the actuator dynamics and injection scheme is presented in Chapter 2.

In order to examine the effectiveness of feedback control at reducing separation-induced distortion, it is necessary to quantify the unsteadiness in the inlet. The two regions in the test section where unsteadiness is quantified are the separation point and the AIP. The means of measuring unsteadiness in the separated region of the inlet is hot-film sensors. These sensors, described in Section 2.2.1.3, capture the unsteadiness in flow velocity by measuring the time-varying shear stress at the inlet surface. The AIP unsteadiness is characterized by perturbations in the total pressure. Each location is equipped with multiple sensors, five hot-film sensors and up to forty total pressure probes, to best quantify the unsteady flow behavior. Chapter 4 discusses the series of experiments performed to characterize the unsteady airflow in each region.

Although multiple sensors exist at the separation point and AIP, to simplify the design of the control laws implemented in this chapter, the unsteadiness of each region is characterized by a single measurement. For the separated region, hot-film number 4 (see Figure 2.7) is chosen to quantify unsteadiness. Of all the hot-film responses, number 4 displayed the most consistent unsteady behavior during the inlet characterization experiments. As for the AIP, producing a single quantity that best describes the unsteady character of the distortion is a greater challenge. The approach used for the feedback control experiments involves linearly combining the total pressure measurements of several probes located in various radial and circumferential positions. This process of creating "bulk parameters" is discussed in Section 4.4. Identifying a single quantity to represent unsteadiness allows

for the implementation of single input single output (SISO) control laws. This class of control laws is the simplest to design and implement. The input quantity for the control laws is the measure of unsteadiness, either hot-film or AIP bulk parameter, while the output is the actuator command voltage. The goal of the SISO control laws is to minimize the unsteady quantity by driving the input of the system to zero.
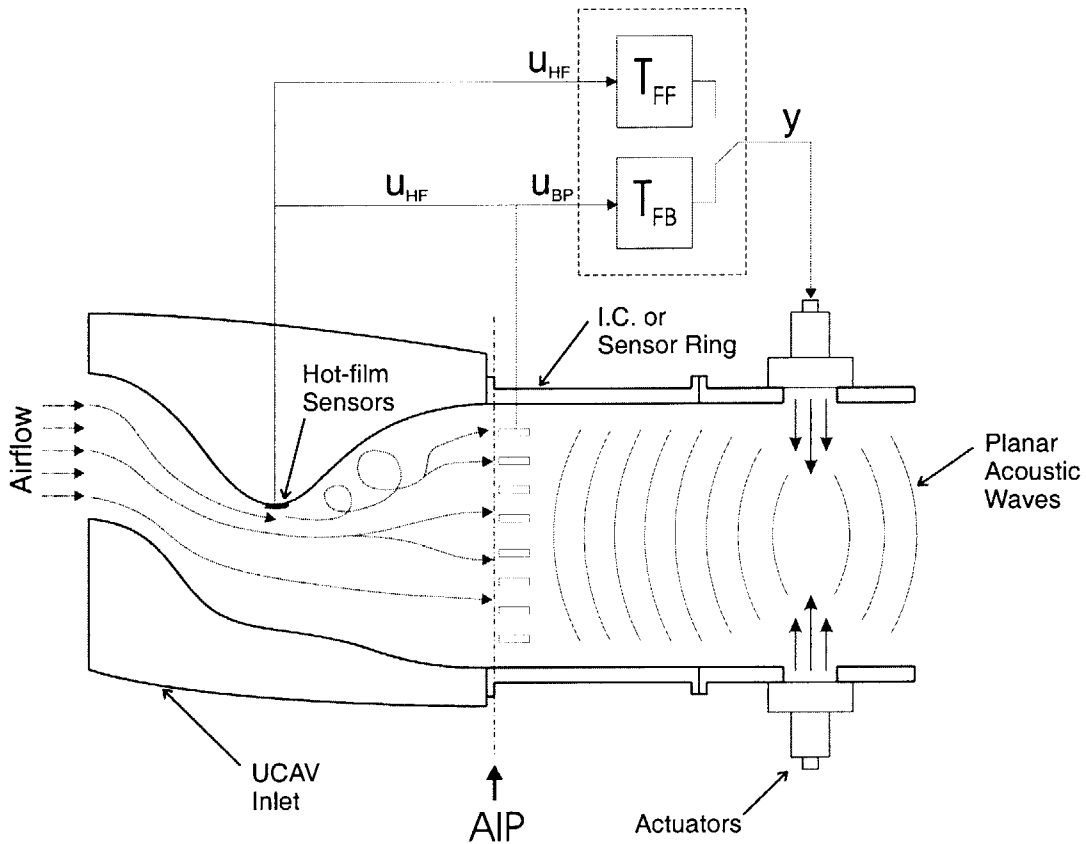
Figure 5.1 – Physical Description of Active Control

Figure 5.1 illustrates the physical setup of the active control experiments. The unsteady quantity, either u_{HF} or u_{BP}, is read by the control law, which is continuously executing on a DSP. A description of the hardware and software executing the discrete control law is presented in Section 2.5. The two control laws, T_{FB} and T_{FF}, represent feedback and feed-forward control, respectively. The design and implementation of these two control laws is discussed in the subsequent sections. The output of the control law, y, is then sent to the actuators to dictate the position of the actuator valve. This input to the actuators generates planar acoustic waves inside the actuator duct. These waves travel upstream

94

to the AIP and UCAV inlet, where they influence the unsteady flow behavior, and close the loop of the control system.

5.1   SINGLE FREQUENCY FEEDBACK CONTROL

The simplest experiment that demonstrates the effectiveness feedback control to reduce unsteadiness uses a single frequency resonator as the control law. The resonator acts as a narrow band filter to isolate the response of a desired frequency of the input signal. The output signal supplied to the actuators from the resonator is solely a function of the resonator frequency. Thus, single frequency control attempts to reduce the unsteadiness of the input quantity over a very narrow frequency band[7]. The goal of the single frequency control experiments is to determine whether downstream actuation is effective at reducing inlet flow unsteadiness. Broadband reduction of unsteadiness is only possible if narrow band reduction is successful.

5.1.1   RESONATOR FILTER DESIGN

The resonator filter is a second order transfer function with a lightly damped pole at the frequency of interest. Equation 5.1 describes the resonator transfer function in the continuous frequency domain where, $s = j\omega$.

$$H(s) = \frac{k}{s^2 + 2\xi\omega_0 s + \omega_0^2} e^{-s\tau}$$

(5.1)

The complex pole pair, $s_{1,2} = -\xi\omega_0 \pm j\omega_0\sqrt{1-\xi^2}$, characterizes the resonator pole, and τ represents the time delay of the filter. The purpose of the pure time delay is to add phase to the filter transfer function. The time delay, along with the resonator gain, damping ratio and resonant frequency,

---

[7] The range of the frequencies targeted by the resonator filter depends on the damping ratio of the resonator. For these experiments the frequency band is approximately 20-50 Hz.

constitute the parameters used to optimize the design of the resonator filter. This optimization is discussed in the experimental results (Section 5.1.2).

To implement the resonator filter in the experimental setup, the continuous filter, equation 5.1, is transformed into a discrete-time transfer function. This is accomplished by using the z-transform, equation 5.2, to transform the complex poles and gain of the continuous filter to discrete time. The time increment used to discretize the continuous system, T_s, corresponds to the sample frequency of the computer implementing the controller.

$$z = e^{-sT_s}$$

<div align="right">(5.2)</div>

The technique used to discretize the continuous filter is called "pole and zero mapping" [20]. As the name states, this technique involves mapping the poles and zeroes from the continuous to discrete time domain. Equation 5.3 yields the transformation of the discrete resonator poles.

$$z_{1,2} = e^{-\xi\omega_0 T_s}\left[\cos\left(\omega_0 T_s \sqrt{1-\xi^2}\right) \pm j\sin\left(\omega_0 T_s \sqrt{1-\xi^2}\right)\right]$$

<div align="right">(5.3)</div>

The transfer function that corresponds to the mapping technique is describes by equation 5.4. In this transfer function, the coefficients a_1 and a_2 are the negative sum and product of the discrete time poles, respectively. The discrete gain, k_z, is the product of the continuous gain and the discrete time increment, T_s. Equation 5.4 is given the notation $H'(z)$ rather than $H(z)$, the actual z-transform of equation 5.1, because $H'(z)$ does not include a transformation of the pure time delay, $e^{-s\tau}$. The pure time delay is incorporated into the discrete transfer function by adding discrete sample lags. Equation 5.7 describes how to add incremental lag to the discrete transfer function.

$$H'(z) = \frac{y(k)}{u(k)} = \frac{k_z\left(1-z^{-1}\right)}{1+a_1 z^{-1}+a_2 z^{-2}}$$

<div align="right">(5.4)</div>

Equation 5.4 is presented in a form such that the exponents of z are negative. This representation allows for the creation of the algorithm used to implement the discrete time transfer function. Equation 5.5 illustrates the relationship between the z-transform and discretized samples. In this equation, $x(n\text{-}m)$ represents the value of the signal that lags the current value, $X(z)$, by m time increments.

$$x(n-m) \overset{z}{\Leftrightarrow} X(z) \cdot z^{-m}$$

(5.5)

Applying equation 5.5 to equation 5.4 yields the relationship between the input and output signals in the sampled-data computer controller.

$$y(n) = k_z u(n) - k_z u(n-1) - a_1 y(n-1) - a_2 y(n-2)$$

(5.6)

One method for accounting for the time delay presented in equation 5.1 is to add an integer number of sample delays, l, to the input signal in equation 5.6. This method effectively adds time delay to the controller; however, this time delay is constrained to integer multiples of the sample time ($\tau_l = T_s \cdot l$).

$$y(n) = k_z u(n-l) - k_z u(n-1-l) - a_1 y(n-1) - a_2 y(n-2)$$

(5.7)

5.1.2   RESULTS OF EXPERIMENTAL CONTROL

The goal of the single frequency control experiments is to determine if feedback control using downstream actuation reduces flow unsteadiness. The experimental methodology employed is trial and error. The code used to implement the resonator filter is written such that the executable program prompts the experimental operator to input the gain, damping ratio, resonant frequency and time delay of the filter. This allows the operator to perform real-time modifications to the filter during an experiment, thus enabling optimization of the control law for each resonator frequency.

To verify the effectiveness of single frequency control, a matrix of nine experiments was performed. The matrix includes experiments on the three unsteady quantities, hot-film, extent and magnitude, for three resonator frequencies, *100, 200* and *300 Hz*. These frequencies were identified as interesting frequencies to study, based on results from the acoustic model and experimental transfer functions. For the bulk parameters, extent and magnitude, the transfer functions in Section 4.5.1 indicate that the actuators have little authority at *200 Hz*. Thus, it is valuable to study the effects of control at this frequency for the bulk parameters and hot-film. The experiments at *100 Hz* aim to study the effects of control at low actuation frequencies. Likewise, the 300 Hz experiments aim to study the effects at high actuation frequencies.

A summary of the results from the nine experiments is listed in Table 5.1, while Table 5.2 lists the resonator input parameters for each experiment. The results of these experiments verify the inability of the actuators to influence total pressure unsteadiness at *200 Hz*. Figure 5.2 - Figure 5.10 show RMS plots, with and without feedback control, for each of the nine experiments.

In addition to studying how the single frequency control law affects the unsteady input parameter, it is also beneficial to study the RMS response of the unsteady quantities that are not being fed back. For example, it is important to understand the effect that reducing separation unsteadiness has on AIP unsteadiness. These results help in understanding the link, if any, between controlling separation unsteadiness and subsequent AIP distortion levels. Figure 5.13 shows this link for the *300 Hz* resonant filter, and Figure 5.14 illustrates it for the *200 Hz* filter. In both cases, the extent and magnitude bulk parameters responded similarly, therefore, it is only necessary to present one set of results (magnitude). A plot of the *100 Hz* case is omitted from the results because the data appears to be spurious. The *200 Hz* case (Figure 5.14) illustrates no variation in AIP unsteadiness when the hot-film control law is active. This case was important in studying the coupled effects on the overall system dynamics when controlling separation point unsteadiness. Figure 5.7 shows a reduction in *200 Hz* RMS at the hot-film sensor, however this case results in no reduction of the AIP total pressure RMS. The conclusion drawn from these results is that the controller is only shown to be effective at locally reducing unsteadiness. This means that the actuation creates acoustic waves to cancel measured quantities at the sensor locations rather than altering how the separated vortices shed and propagate downstream. For the *300 Hz* case, the resonator design used to optimize reduction of hot-film unsteadiness has a detrimental affect on the bulk parameter unsteadiness. Sections 5.1.3 and Chapter 6 include further discussions of these results.

Control Parameter	Resonator Freq. (ω_0)		
	100 Hz	200 Hz	300 Hz
Magnitude	~75 % reduction of RMS at 100Hz. Notch ranges from 90 to 110 Hz. Large RMS spikes at 70 and 125 Hz.	No improvement.	~75 % reduction of RMS at 200Hz. Notch ranges from 290 to 320 Hz. Large RMS spikes at 265, 345, and 360 Hz.
Extent	~60 % reduction of RMS at 100Hz. Notch ranges from 95 to 105 Hz. Small RMS spikes at 75 and 125 Hz.	No improvement.	~80 % reduction of RMS at 200Hz. Notch ranges from 290 to 307 Hz. RMS spikes at 335 and 350 Hz.
Hot-film	RMS reduction over entire frequency range. Validity of these results is questionable.	~85 % reduction of RMS at 200Hz. Notch ranges from 195 to 205 Hz. Small RMS spikes at 115, 145, and 225 Hz.	~75 % reduction of RMS at 200Hz. Notch ranges from 290 to 312 Hz. Small RMS spikes at 250 Hz.

Table 5.1 – Summary of Results using Single Frequency Feedback Control

Figure	Parameter	Resonator Freq. (ω_0)	Damping Ratio (ξ)	Gain (K)	Time Delay (τ)	Phase ($360 \cdot \omega_0 \cdot \tau$)
Figure 5.2	Magnitude	100 Hz	0.01	8000	7.00 ms.	252°
Figure 5.3	Extent	100 Hz	0.01	5000	6.50 ms.	234°
Figure 5.4	Hot-film	100 Hz	0.01	2000	5.50 ms.	198°
Figure 5.5	Magnitude	200 Hz	0.01	6000	1.25 ms.	90°
Figure 5.6	Extent	200 Hz	0.01	6000	1.25 ms.	90°
Figure 5.7	Hot-film	200 Hz	0.01	2000	4.50 ms.	324°
Figure 5.8	Magnitude	300 Hz	0.01	8000	1.25 ms.	135°
Figure 5.9	Extent	300 Hz	0.01	8000	1.25 ms.	135°
Figure 5.10	Hot-film	300 Hz	0.01	2000	0.00 ms.	0°

Table 5.2 – Single Frequency Controller Input Parameters
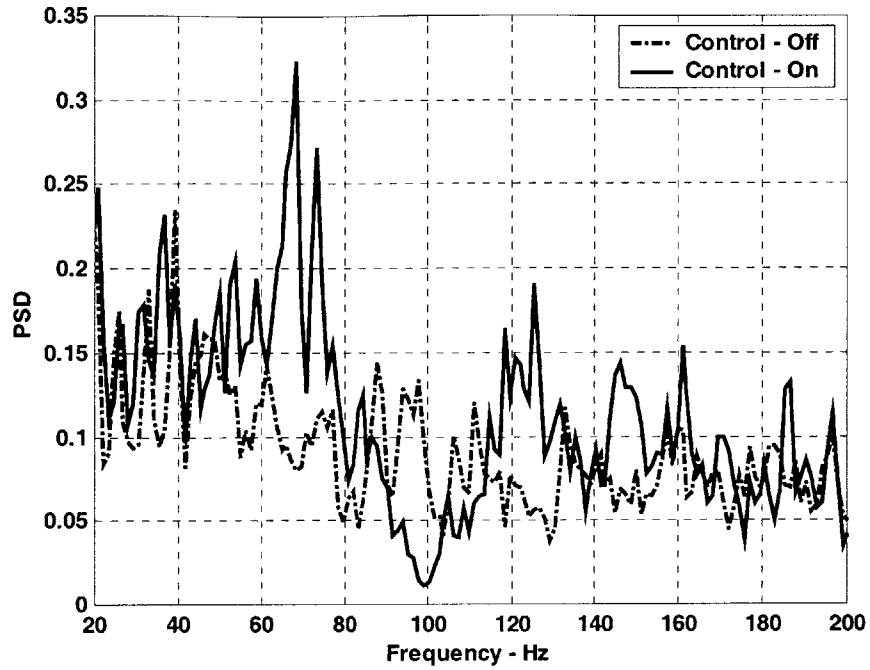
Figure 5.2 – Single Frequency (100 Hz) Feedback Control of Magnitude
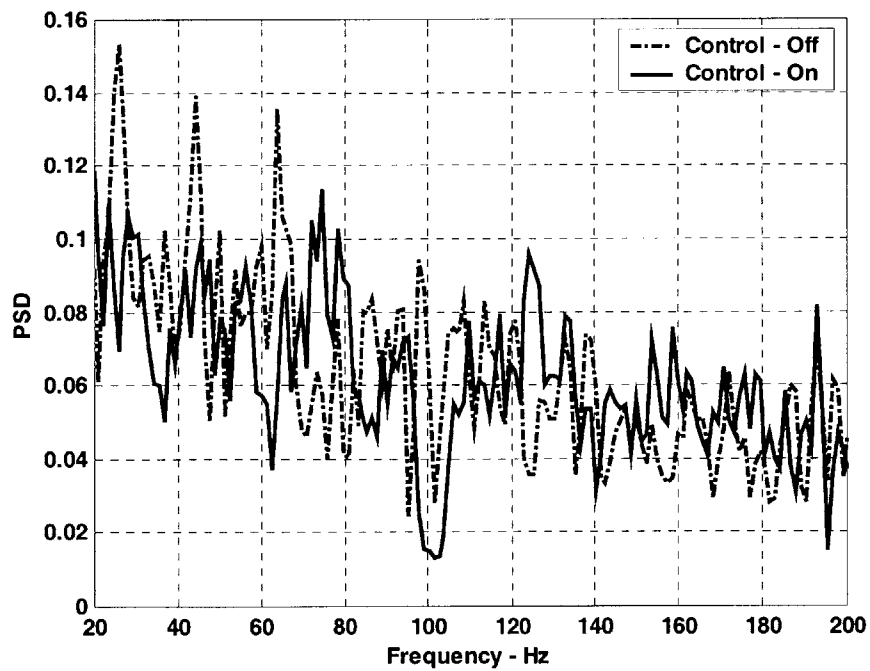
Figure 5.3 – Single Frequency (100 Hz) Feedback Control of Extent
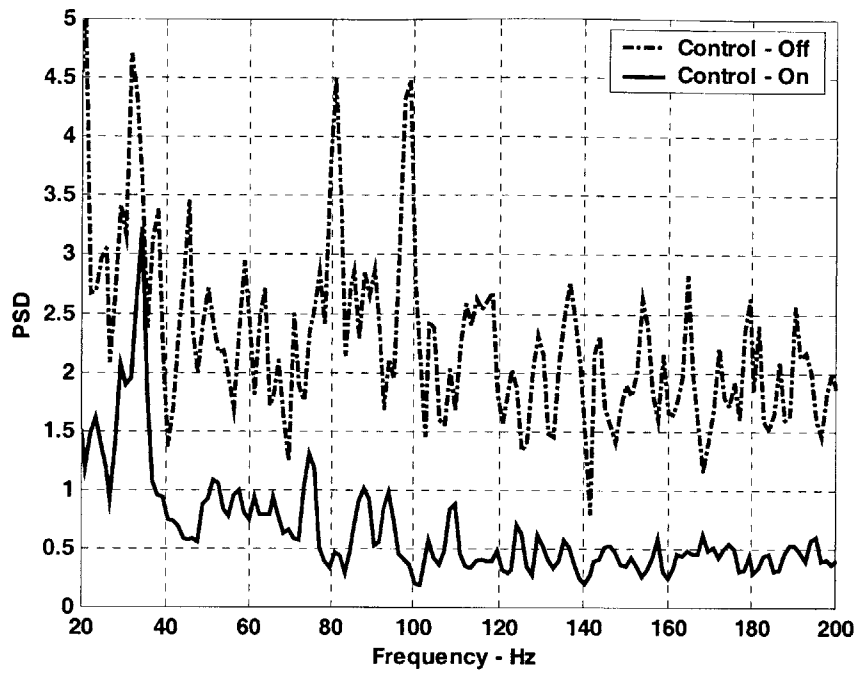
Figure 5.4 – Single Frequency (100 Hz) Feedback Control of Hot-film 4
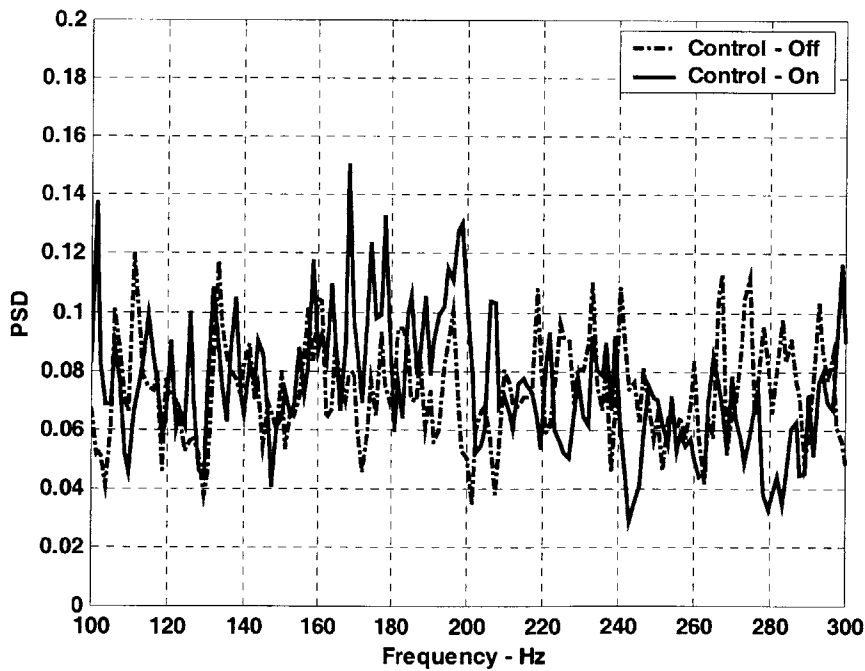
Figure 5.5 – Single Frequency (200 Hz) Feedback Control of Magnitude
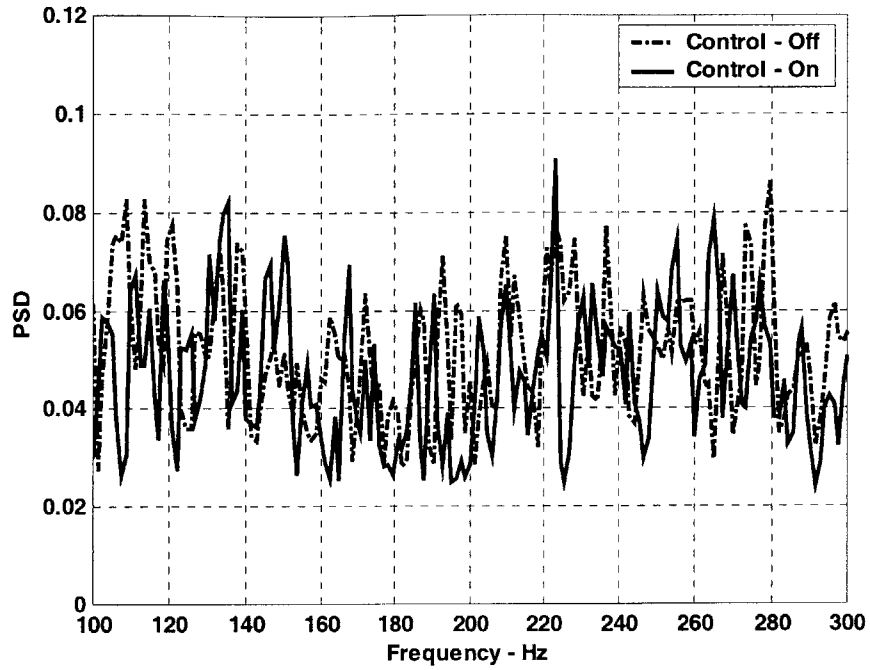
Figure 5.6 – Single Frequency (200 Hz) Feedback Control of Extent
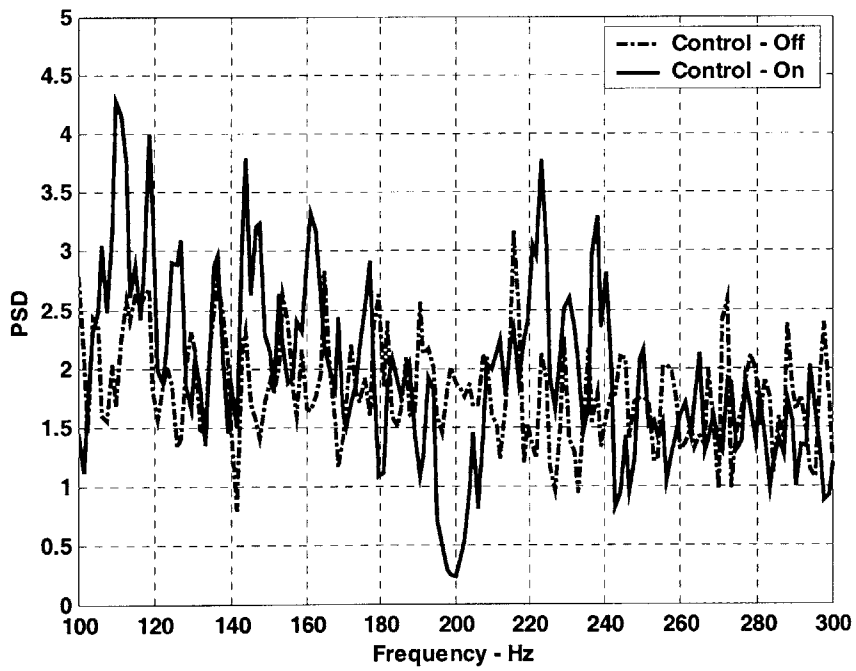
Figure 5.7 – Single Frequency (200 Hz) Feedback Control of Hot-film 4
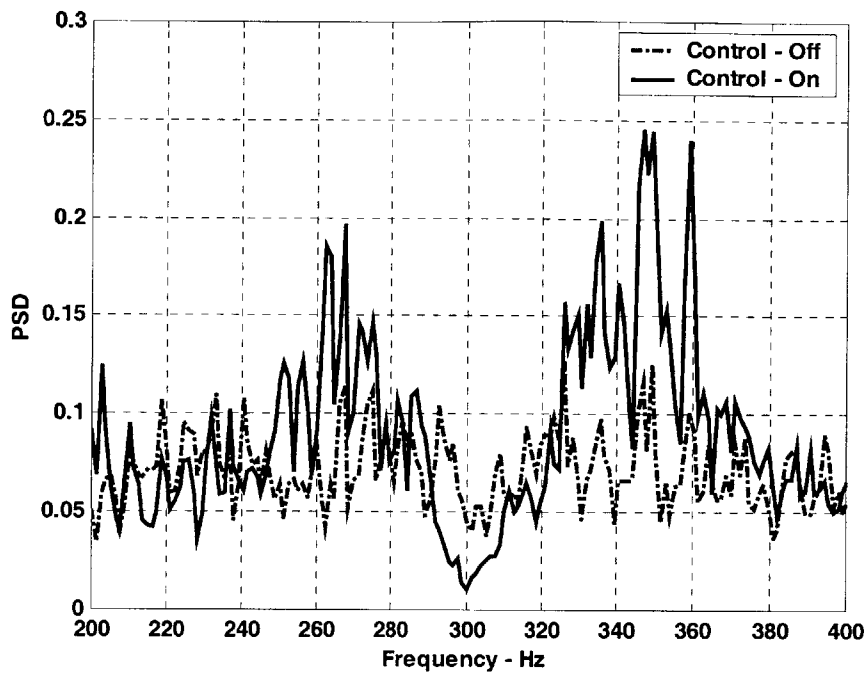
Figure 5.8 – Single Frequency (300 Hz) Feedback Control of Magnitude
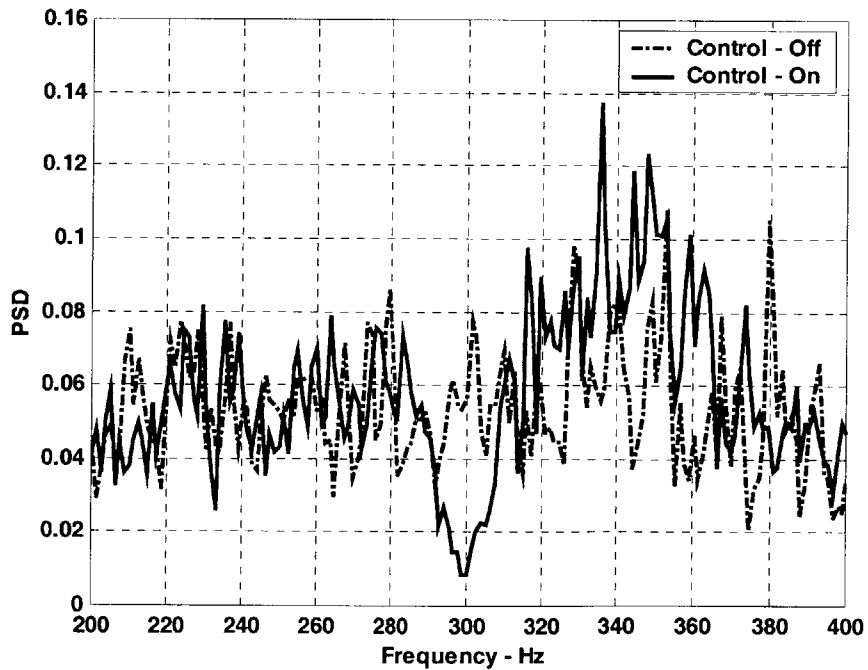
Figure 5.9 – Single Frequency (300 Hz) Feedback Control of Extent

103
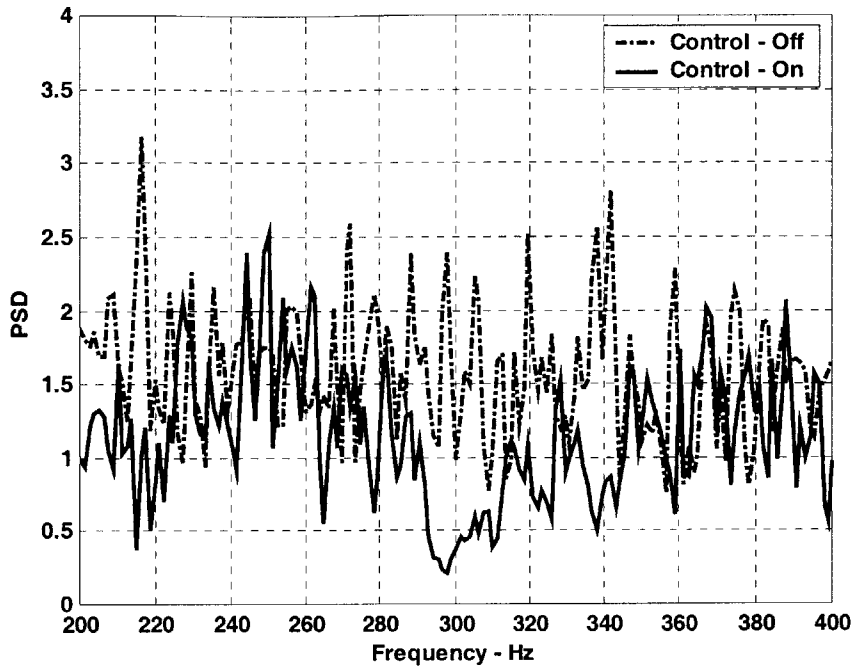
Figure 5.10 – Single Frequency (300 Hz) Feedback Control of Hot-film 4
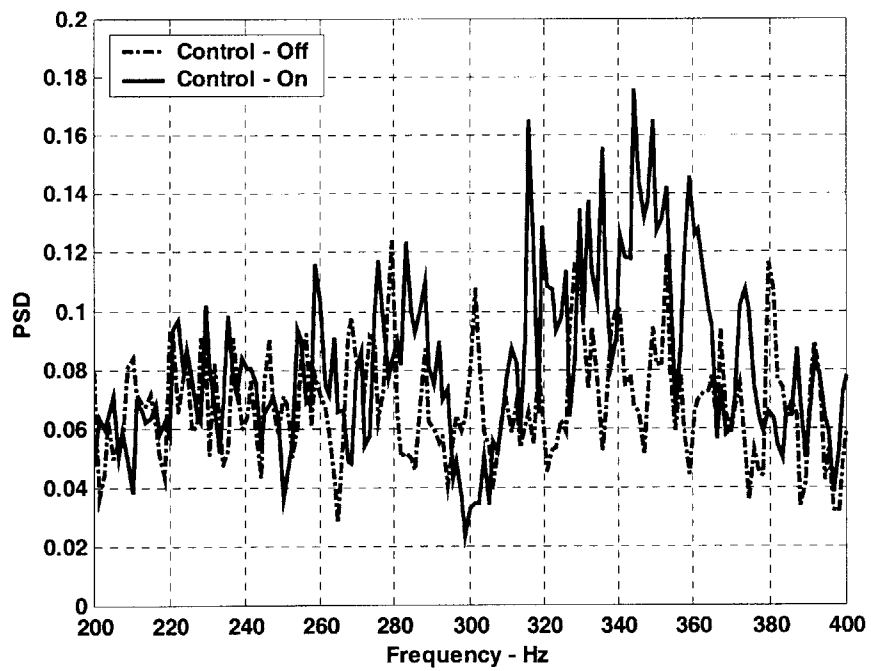
Figure 5.11 – Residual Effect on Magnitude by Reducing Extent (300 Hz)
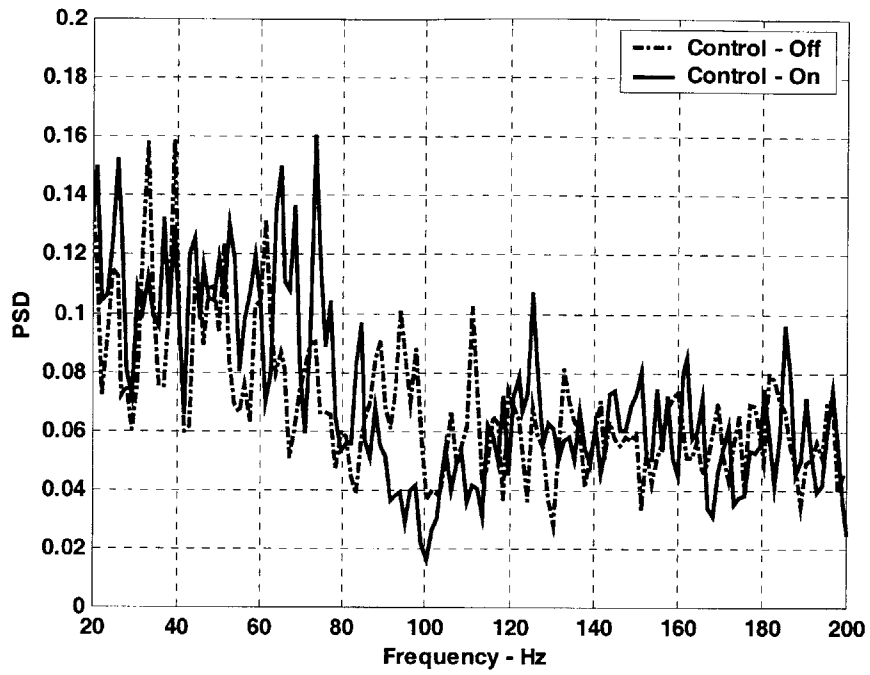
Figure 5.12 – Residual Effect on Extent by Reducing Magnitude (100 Hz)
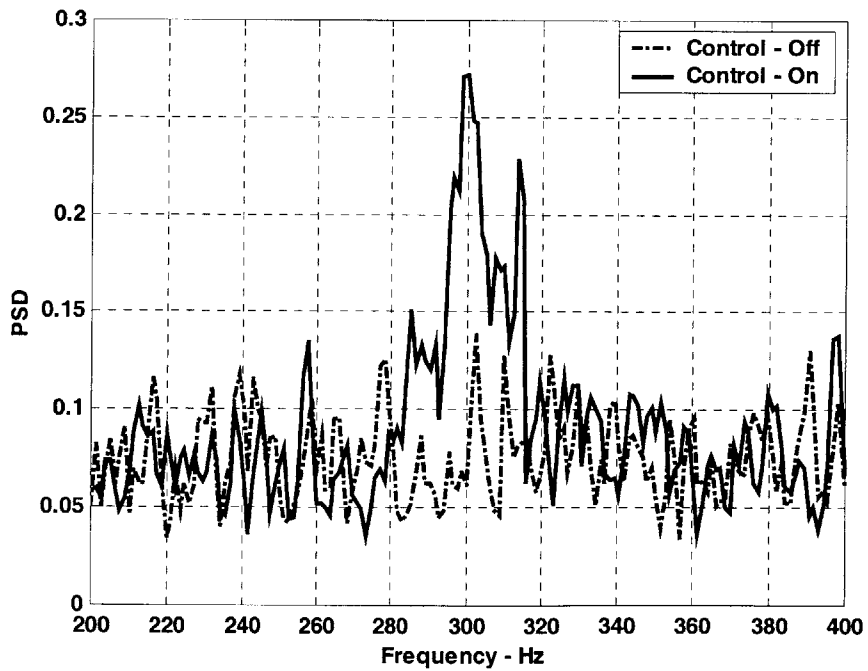
Figure 5.13 – Residual Effect on Magnitude by Reducing Hot-film 4 (300 Hz)

105
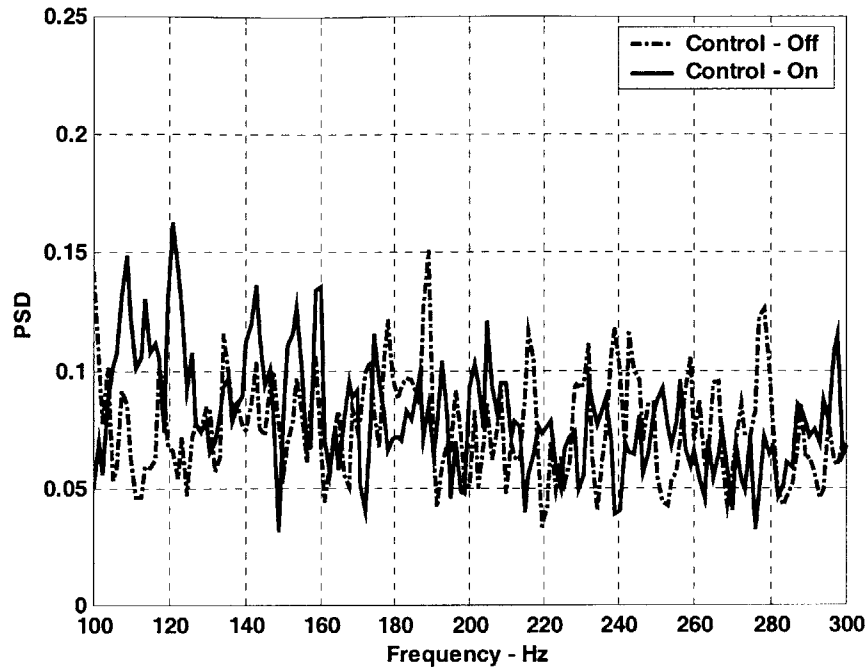
Figure 5.14 – Residual Effect on Magnitude by Reducing Hot-film 4 (200 Hz)

5.1.3 THEORETICAL CONTROL MODEL

To validate the experimental results found in the previous section, the feedback control system is modeled. Figure 5.15 describes this feedback control system, where G is the experimental plant transfer function, H is the discrete resonator filter, d represents the disturbance source and y is the unsteady measurement. Based on this control schematic, equation 5.8 represents the transfer function of the feedback system.

$$\frac{y}{d} = \frac{1}{1 + HG}$$

(5.8)

106
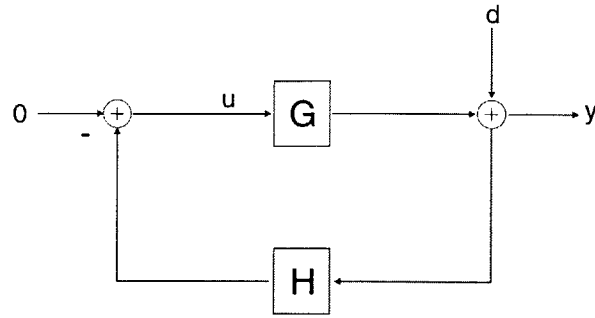
Figure 5.15 –Single Frequency Controller Schematic

Equation 5.9 relates the spectral densities of the disturbance and output. Calculating this spectral relationship requires the modeled transfer functions of both H and G, equations 5.4 and 4.5 respectively. Given these transfer functions and the assumption that the input power spectral density (PSD) is normalized white noise ($\mathcal{D}_{yy}(\omega) = 1$), a MATLAB code computes the power spectral density response for the feedback controller. Figure 5.16 - Figure 5.18 show the results of the theoretical spectral responses at conditions identical to the experiments discussed in Section 5.1.2.

$$\Phi_{yy} = \left\| \frac{1}{1+HG} \right\|^2 \Phi_{dd}$$

(5.9)

The results of the theoretical, single-frequency, feedback models show good agreement with the experimental results. In the *300 Hz* cases the theoretical models for the hot-film, magnitude and extent verify that the experimental inputs of Table 5.2 coincide with the near-optimal resonator designs. Of the *300 Hz* cases, only the results of the extent model predict a slight instability in the notch filter. This large spike at *380 Hz* (see Figure 5.18) indicates the possibility of an unstable controller. However, the large spike predicted by the theoretical model is not obvious in the experimental results (Figure 5.8). The conclusion of this comparison is that there is a slight discrepancy between the optimal experimental inputs and the theoretical model. Examining Figure 4.16 shows a lack of data points in the *300 Hz* region of the transfer function from the actuators to the hot-film. As a result, the accuracy of the transfer function at this frequency is questionable. This is a possible explanation for the slight discrepancy between the optimal experimental inputs and the theoretical model. The optimal theoretical model occurs at a phase of approximately *45°* rather than

107

the *135°* resulting from the experimental optimization. This discrepancy, while large, can be accounted for by error in the experimental transfer function or error in determining the optimal experimental control inputs.

The *200 Hz* resonator experiments provided the most interesting results because the bulk parameters did not respond to feedback control. Therefore, it is interesting to examine the results predicted by the theoretical model at this frequency, shown in Figure 5.17. The theoretical results for the hot-film indicate a large reduction in unsteadiness at *200 Hz* and a moderate increase in unsteadiness at higher frequencies. This result corresponds to the experimental data (Figure 5.7), except the model indicates a wider frequency range of reduction. In the *200 Hz* experiments performed on the bulk parameters, no reduction in unsteadiness is seen. However, the model results indicate that a slight reduction is possible. This discrepancy is explained by examining the actuator voltage to bulk parameter transfer functions (Figure 4.14 and Figure 4.15). There are no experimental data points in the *180-220 Hz* range, and although the transfer function model predicts a trough, the depth of this trough is unknown. As a result, an extremely high gain in the theoretical model may produce some reduction, whereas no reduction is feasible in the experiments. Since *200 Hz* single frequency control was ineffective at reducing unsteadiness in the bulk parameters, it was impossible to identify a set of optimal inputs for the experimental controller. As a result, the inputs for these cases, identified in Table 5.2, are probably not the optimal inputs. Thus, the *200 Hz* theoretical models of the bulk parameters are not expected to be optimal.

The results of the *100 Hz* theoretical model are very similar to the *300 Hz* results. The optimal models of extent and magnitude (see Figure 5.16) match the experimental inputs from Table 5.2. However, the experimental inputs of the hot-film controller do not correspond to the optimal theoretical model. This discrepancy is due to the spurious nature of the experimental hot-film data during the *100 Hz* control experiment. The experimental results for the hot-film, shown in Figure 5.4, are obviously incorrect. Therefore, the experimental inputs might not correspond to the optimal controller design. This explains the discrepancy between the alleged experimental optimum and the theoretical optimum. The theoretical model shown in Figure 5.16 is the theoretical optimum, with a phase of *72°* rather than *198°*.
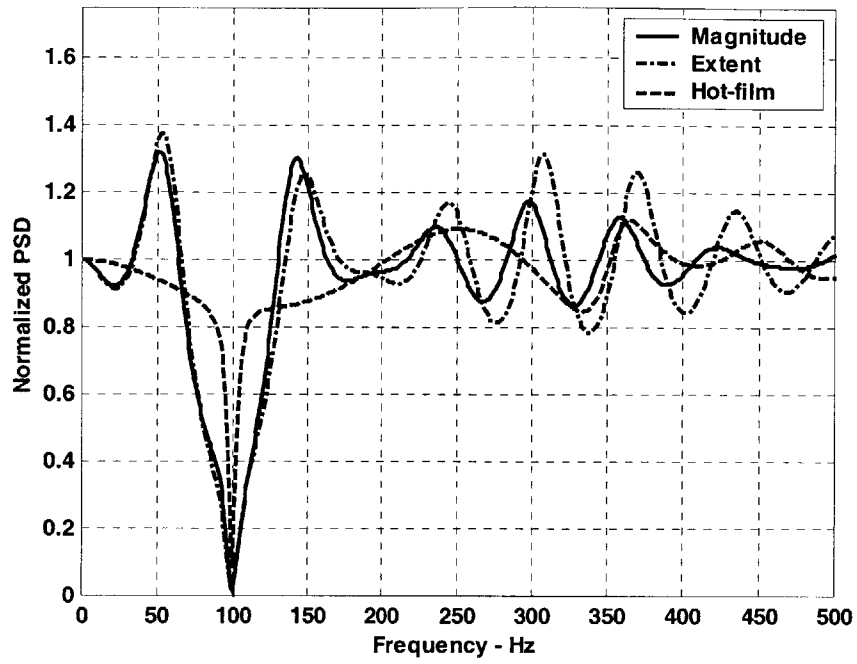
Figure 5.16 – Theoretical Feedback Control @ 100Hz
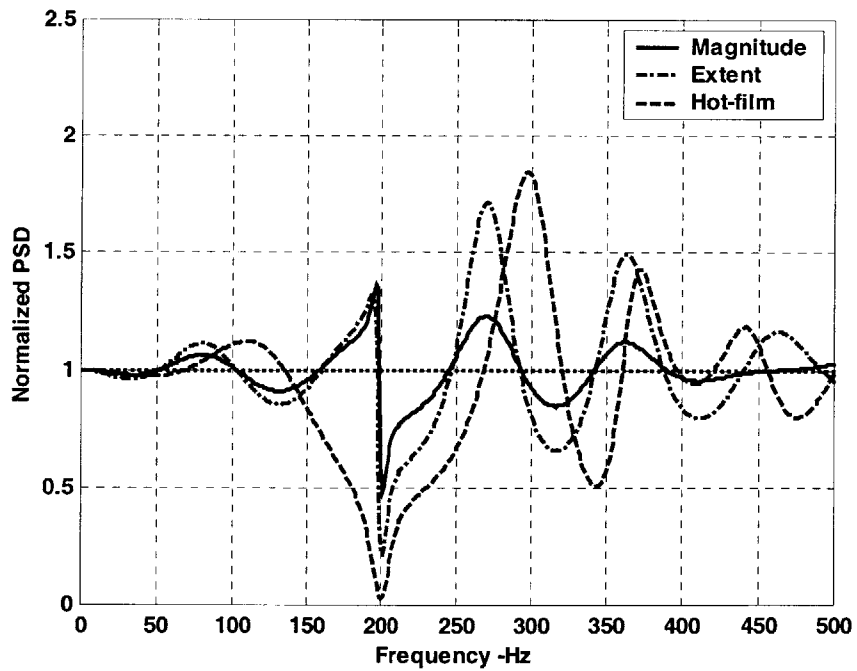
Figure 5.17 – Theoretical Feedback Control @ 200Hz

109
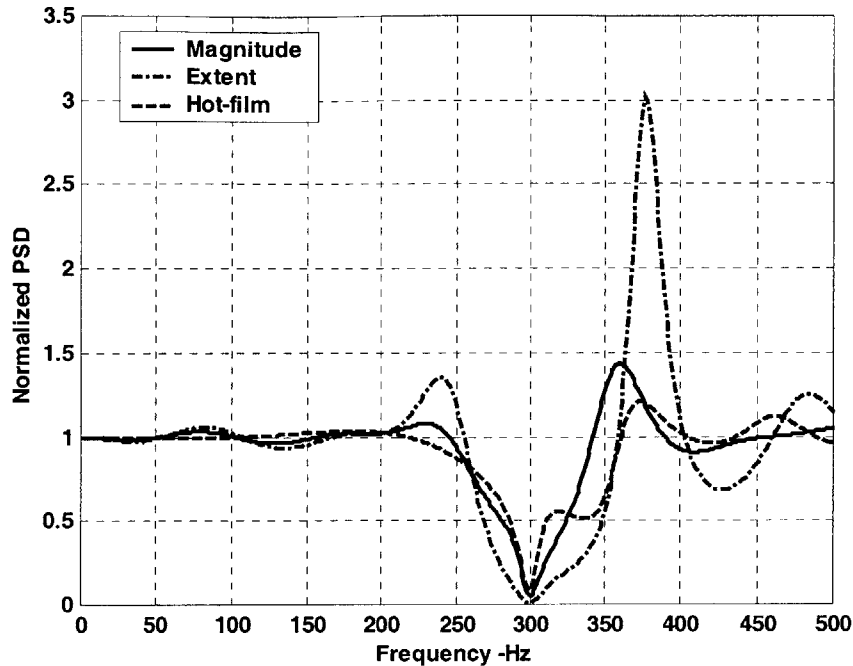
Figure 5.18 – Theoretical Feedback Control @ 300Hz

5.2 BROADBAND FREQUENCY FEEDBACK CONTROL

The results of the single frequency experiments demonstrate that reduction of unsteadiness is physically possible when controlling small frequency bands in the inlet. However, the goal of this research is to reduce unsteadiness across the broadband frequency range of the actuators (*50-500 Hz*). The single frequency experiments reduced unsteadiness for narrow frequency bands. A broadband controller could be constructed from the linear combination of many single frequency controllers spanning the broadband frequency range. The success of the single frequency tests and this concept of linearity across the frequency range, indicate that broadband reduction of unsteadiness in feasible. However, designing and potentially implementing a broadband controller depends heavily on the model of the plant dynamics, $G(s)$. The strong correlation of the theoretical single frequency feedback model with the experimental results indicates that these transfer functions, between the actuation and sensors, adequately describe the flow physics in the experimental setup. Given this confidence in the modeled plant transfer functions, an attempt is made to design a broadband feedback controller.

110

5.2.1   LQG COMPENSATOR DESIGN

The Linear Quadratic Guassian (LQG) method uses elements of a Linear Quadratic Regulator and a Kalman Filter to design the compensator transfer function [11]. Similar to the single frequency controller design, the feedback loop is described by Figure 5.19, where K is the LQG compensator.
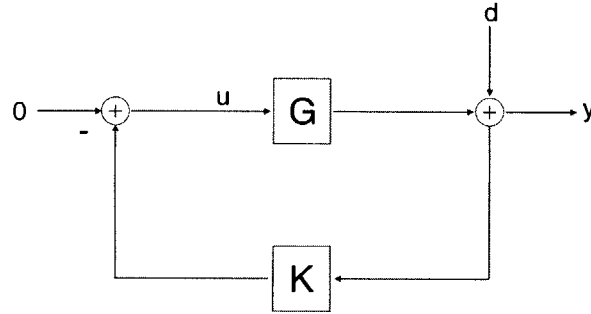
Figure 5.19 – LQG Feedback Controller Schematic

Based on the state-space representations of the plant transfer functions, $G(s)$, a MATLAB code computes the optimal LQG compensator. The only problem with using LQG methods to compute the compensator, $K(s)$, is the difficulty associated with incorporating the pure time delay of the plant dynamics into the state-space representation. To account for the time delay when designing the optimal LQR compensator, the time delay must be represented by a set of poles and zeros rather than by $e^{-s\tau}$. Equation 5.10 represents the Second Order Pade Approximation [22] of a pure time delay.

$$e^{-s\tau} \cong \frac{1 - \frac{\tau}{2}s + \frac{\tau^2}{12}s^2}{1 + \frac{\tau}{2}s + \frac{\tau^2}{12}s^2}$$

$$(5.10)$$

When applied to the plant transfer function, Section 4.5, the Pade approximation adds two poles, $-\frac{3}{\tau} \pm j\frac{\sqrt{3}}{\tau}$, and two zeros, $\frac{3}{\tau} \pm j\frac{\sqrt{3}}{\tau}$, to the transfer function. The Pade approximation works very well when representing small time delays (less than 2.00 ms). However, the approximation does a poor job of representing large time delays for frequencies greater than 100 Hz. This limitation

presented a problem in the design of the bulk parameter compensators because the times delays associated with these plant transfer function are large, ~7.75 ms.

The Pade approximation technique allows the use of MATLAB to calculate the compensator transfer functions. Figure 5.20 and Figure 5.21 display the results of the optimal LQG compensator design for each of the three unsteady quantities. Table 5.3 lists the properties of each compensator transfer function.
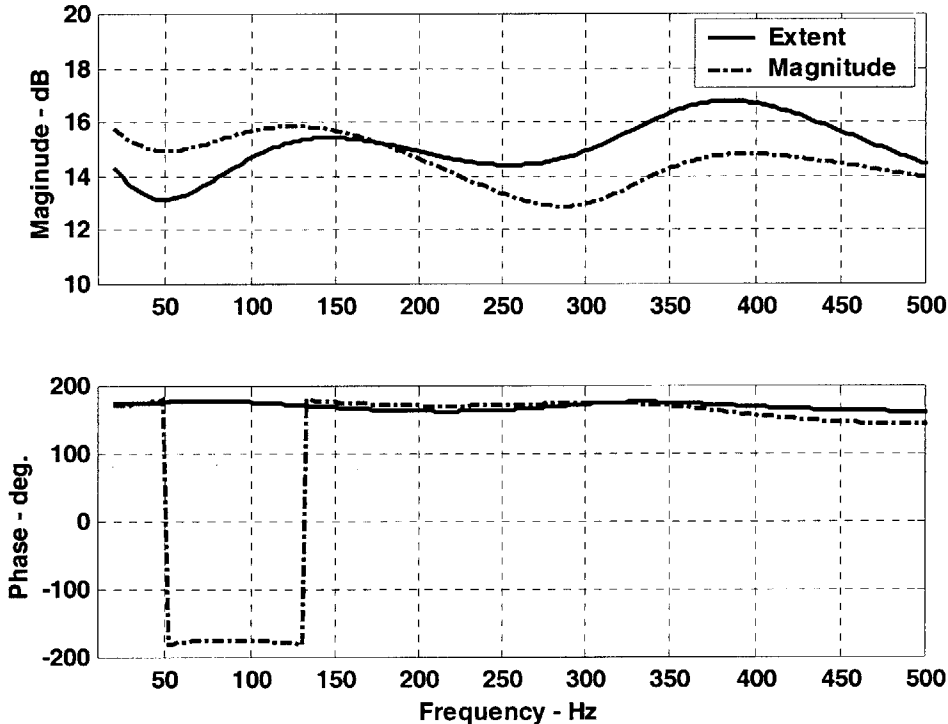
Figure 5.20 – LQG Compensator Transfer Functions for the Bulk Parameters

112
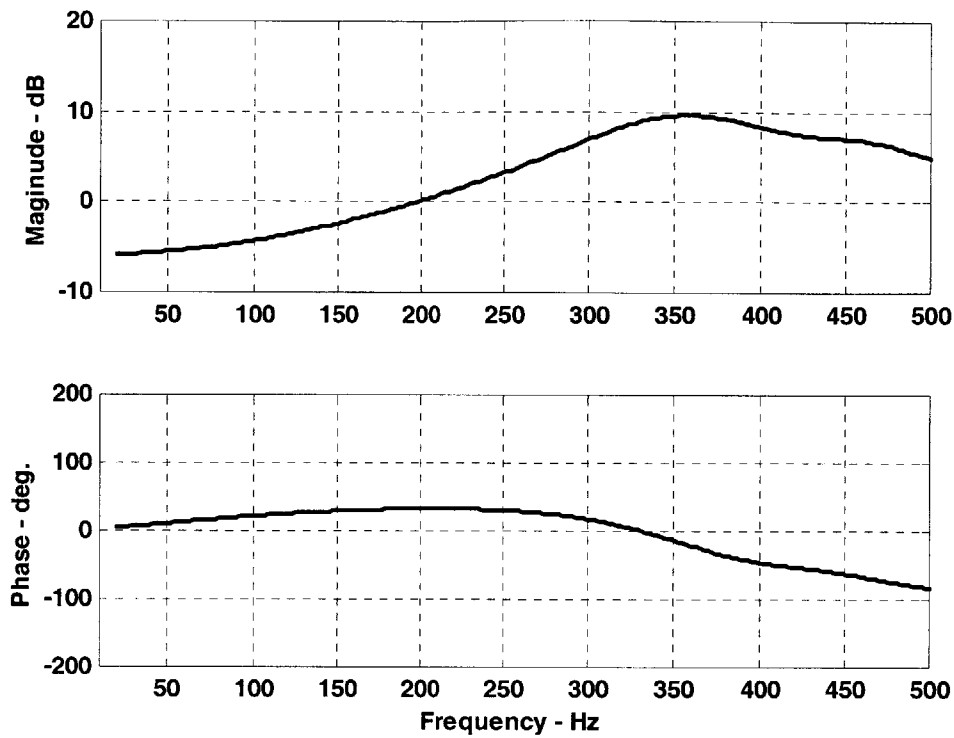
Figure 5.21 – LQG Compensator Transfer Function for the Hot-film

Parameters	Compensator Input		
	Magnitude	Extent	Hot-film
Zeros	-419 Hz, -73 ± j·307 Hz, -60 ± j·25 Hz.	-483 Hz, -125 ± j·312 Hz, -56 ± j·26 Hz.	-190 Hz, -159 ± j·92 Hz, -60 ± j·448 Hz.
Poles	-14,112 Hz, -37 Hz -83 ± j·338 Hz, -113 ± j·93 Hz.	-5,865 Hz, -30 Hz -87 ± j·369 Hz, -103 ± j·112 Hz.	-48 ± j·460 Hz, -63 ± j·352 Hz, -162 ± j·88 Hz.
Gain	-3.1474×10^5	-1.0276×10^5	2.2667×10^3

Table 5.3 – LQR Compensator Transfer Function Parameters

113

5.2.2   THEORETICAL CONTROL MODEL

The compensator transfer functions perform the same function as the resonator filter in the single frequency control experiments and analysis. Therefore, the same methodology, developed in Section 5.1.3, is applied to evaluate the compensators effect on broadband unsteadiness.

$$\Phi_{yy} = \left\| \frac{1}{1+KG} \right\|^2 \Phi_{dd}$$

(5.11)

Figure 2.2 shows the results from equation 5.11 for the optimal compensators of each of the unsteady parameters. The LQG compensators are effective at reducing the PSD of the unsteady parameters for certain frequency bands across the entire frequency range. However, each compensator also increases the PSD across some portions of the broadband. In general, none of the compensators is successful at reducing the total PSD across the broadband. The failure of the compensator design to reduce unsteadiness may stem from the plant dynamics of the experimental test section.
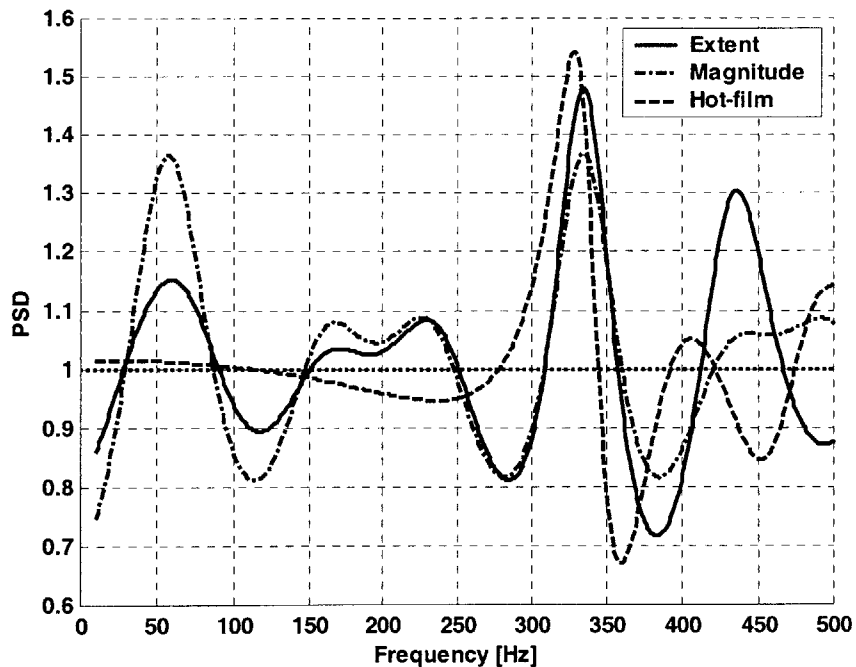
Figure 5.22 – Effects of Theoretical LQG Broadband Control

114

5.2.3   LQG EXPERIMENTAL RESULTS

There were two goals for the broadband control experiment. The first goal was to demonstrate that the experimental setup could implement a broadband control law. The second goal, contingent upon the success of the first goal, was to compare the experimental results of this control law to the theoretical model (Section 5.2.2). Since the theoretical model of the LQG controller predicts no overall reduction in magnitude unsteadiness, a new criterion must be developed to measure the success of the controller. Although the broadband RMS of the unsteadiness does not decrease in the theoretical model, unsteadiness in localized frequency bands either increase or decrease when the controller is active. Therefore, the spectra of the experimental results can be compared to the theoretical model to determine if the compensator was successfully implemented.
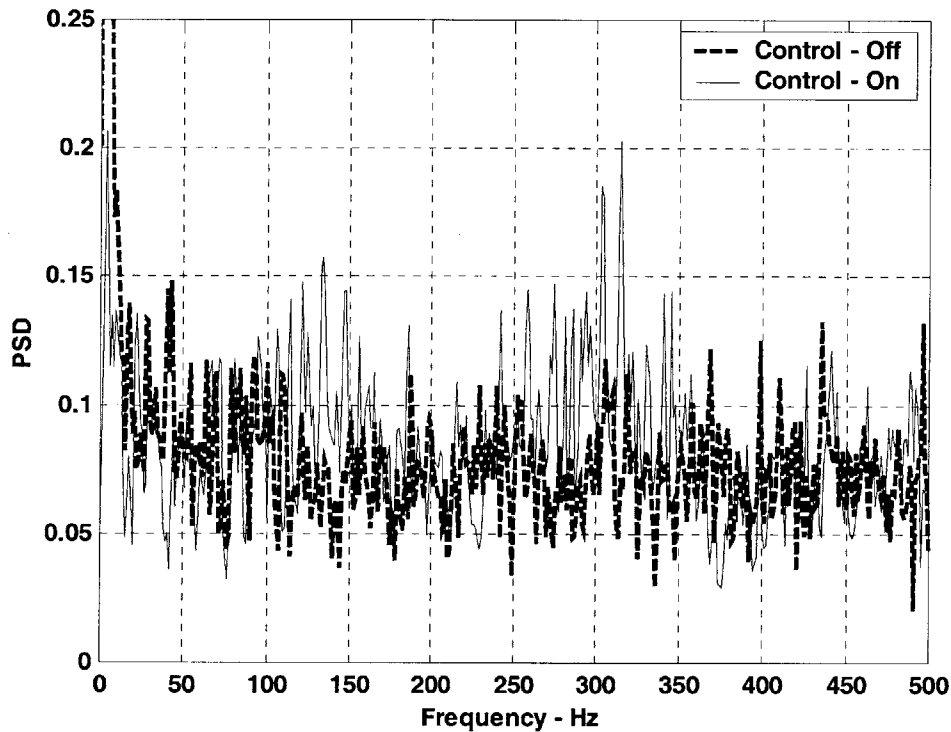
Figure 5.23 – Experimental Results of Broadband LQG Controller on Magnitude BP

The results of the broadband feedback control on the magnitude bulk parameter are shown in Figure 5.23. The experimental results show increases in the unsteadiness at *130, 320* and *500 Hz*. Two of these increases correspond to theoretical peaks in the theoretical model at *340* and *500 Hz*. The low frequency peak in the model occurs at *70 Hz*, which does not match the experimental results. The

115

experimental results also show a decrease in the unsteadiness at *380* and *230 Hz*. These dips correspond to theoretical troughs located at *370* and *270 Hz*. Although the experimental results do not perfectly match the theoretical results, the correlation between the two demonstrates that the LQG compensator was implemented successfully. This result indicates that broadband reduction of unsteadiness using downstream actuation is possible if an effective compensator can be designed.

5.3   FEED-FORWARD CONTROLLER DESIGN

This section describes an alternate form of flow control that may be useful in the UCAV inlet. The advantages of feed-forward control are: the measurement is not the quantity to be reduced, and locating the sensors upstream of the AIP builds some lead into the control system. Adding lead to the control system gives the actuators time to launch acoustic waves upstream to cancel the flow unsteadiness, induced by separation, before it reaches the AIP. The time delay analysis in Section 4.6 discusses the lead-time created by using a feed-forward controller. Figure 5.1 gives a physical description of how feed-forward control would be implemented in the test section. Figure 5.24 illustrates the feed-forward controller, with descriptions of each parameter located in Table 5.4. Similar to feedback control, the design of the feed-forward compensator gains, *K*, involve a closed loop system with the plant dynamics. The major difference between feed-forward and feedback control is transfer function from the hot-film to the AIP, *P*. This transfer function estimates the unsteadiness at the AIP; therefore the controller is designed to cancel this predicted unsteadiness.
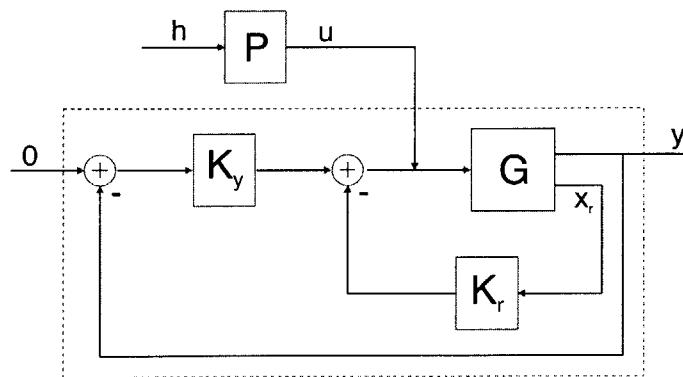
Figure 5.24 – Feed-forward Controller Schematic

Parameter	Description
P	Hot-film to Bulk Parameter Transfer Function
G	Bulk Parameter to Actuator Servo Motor Position Transfer Function
K_y	LQR Output Gain
K_r	LQR State Feedback Gains
h	Hot-film Signal
x_r	State Variables
u	Feed-forward Controller Input Signal (Bulk Parameter)
y	Feed-forward Controller Output Signal (Actuator Command Voltage)

Table 5.4 – Feed-forward Controller Nomenclature

There are two requirements that the experimental system must meet to enable feed-forward control. The first requirement is that the unsteadiness at the separation and AIP must be highly correlated. Under the current sensor configuration the correlation is strong (>0.50) but not sufficient for effective use of feed-forward control (>0.75). Section 4.3 describes the relationship between unsteadiness at the hot-film sensors and the total pressure transducers at the AIP. Although the relationships in that Section establish the correlation between separation point and AIP unsteadiness, the coherence levels in the transfer functions are too low to accurately predict AIP unsteadiness. Future instrumentation configurations at the separation point and AIP may produce higher coherence levels, however, the current experimental setup does not have these capabilities.

The second desirable feature for feed-forward control is that the reference measurement signal must be independent of the actuator signal. Otherwise, the measurement becomes part of a feedback loop and the advantages of feed-forward control are more difficult to realize. Unfortunately, in this experimental setup, a highly correlated transfer functions exists between the reference measurement (hot-film) and the actuators. This transfer function is described in Section 4.5.2. Since the experimental setup meets neither of these requirements, feed-forward control was not attempted.

6 CONCLUSIONS

The experiments discussed in this research represent an initial attempt at controlling inlet distortion via downstream actuation. Much of this research pertained to characterizing unsteadiness in the UCAV inlet. The results of this characterization provide useful knowledge about the relationship between separation and AIP unsteadiness as well as, a basis for applying feedback control to the system. The feedback control experiments are a first attempt at reducing unsteadiness in the UCAV inlet via downstream actuation. The results and conclusions from flow characterization and feedback control are summarized below.

6.1 CHARACTERIZATION OF UNSTEADY INLET FLOW

The first steps taken to characterize unsteadiness in the UCAV inlet were flow visualization experiments. The results of these experiments, shown in Section 4.1, illuminate a region of flow separation on the top surface where the inlet begins to transition from a rectangular to circular section. This separation matches the textbook "owl-face" flow pattern shown in Figure 4.1. This flow pattern is characterized by a region of flow reversal leading to the generation of twin vortices. Based of the flow visualization results it is postulated that the shedding of these vortices is the source of separation unsteadiness.

To quantify unsteadiness at the separation point, hot-film sensors were placed in this region. With hot-film sensors installed, a series of experiments were performed to characterize unsteadiness in the inlet. More specifically, these experiments aimed at determining if a correlation exists between separation point and AIP unsteadiness. The results of these experiments, discussed in Section 4.3, indicate good coherence between these locations near *500 Hz*. These findings establish the correlation between the separation point and AIP unsteadiness. Given this correlation, the goal shifted to identifying the relationship between the unsteadiness at these locations. Identifying a relationship requires good understanding of the AIP unsteadiness. A cross-correlation analysis between AIP pressure sensors, located at the right and left sides of the pressure deficit, revealed that

unsteadiness at these locations is also correlated near *500 Hz*. More importantly, this analysis revealed that the sensors are negatively correlated (see Figure 4.12). This result indicates that the pressure deficit oscillates about the vertical AIP center-plane.

Given the correlation of separation point to AIP unsteadiness and the negatively correlated AIP relationship, two explanations were postulated to describe the oscillation of the pressure deficit. The first states that the separated flow oscillates (snakes back and forth) as it convects downstream to the AIP. The second explanation states that twin vortices (characterized by owl-face separation) shed in a staggered manner such that vortices on the left alternate with vortices on the right. To determine which postulation (if any) best describes the separated flow, movies of the unsteady AIP total pressure were created. These movies illustrate that the pressure deficit expands and contracts (appears and disappears), as it moves from side to side. The motion of the deficit is also seen to be very "choppy" rather than "smooth". These observations support the second explanation of the oscillatory motion. For the first explanation to be true, one would expect to see the size of the pressure deficit remain constant as it smoothly oscillates across the center-plane. However, choppy movements and changing size support the idea that vortices of separated flow alternate in arriving at the left and right sides of the AIP.

Having identified the separation flow as a source of AIP unsteadiness, the focus of the research switched to controlling this unsteadiness. Before feedback control experiments could be performed, system identification was required. System identification consists of determining the transfer functions from the actuators to the various unsteady sensors (see Section 4.5). These transfer functions, primarily used to design feedback control laws, provide information about the ability of actuators to effect flow in the regions where the sensors are located. In these experiments, it was witnessed that no open-loop acoustic oscillations had any affect on pressure recovery. Despite this result, the system identification from the actuators to the hot-film and AIP sensors was successful in producing coherent transfer functions.

6.2   ACTIVE CONTROL OF FLOW UNSTEADINESS

Following the characterization of unsteadiness in the UCAV test section, a series of feedback control tests were performed to reduce unsteadiness in the inlet. The first set of experiments employed a single frequency resonator designed to reduce unsteadiness in narrow frequency bands. Not

120

surprisingly, the single frequency experiments demonstrate that feedback control is successful at reducing localized unsteadiness at the sensor locations (see Section 5.1). Local reduction is defined as the superposition of acoustic waves to cancel the measured quantity at a sensor location. Based on this description, it is not surprising that the actuators were successful at local reduction of unsteadiness. Of more interest to this research is how feedback control affects the coupled system dynamics between the separation point and the AIP. The results of these experiments were studied to determine if single-frequency feedback control effects either the unsteady vortex shedding or how these vortices propagate downstream. Unfortunately, these results do not indicate that feedback control of a single sensor reduces the unsteadiness associated with overall system dynamics. In fact, in some cases, the unsteadiness of the AIP sensors increase as the separation point unsteadiness is reduced (see Figure 5.13). More work is necessary to determine if feedback control can affect the overall system dynamics. The next section lists recommendations for improving the experimental setup that may lead to better understanding of the system dynamics and possibly a means for reducing the unsteadiness associated with these dynamics.

Despite the apparent lack of influence on the coupled system dynamics, the localized reduction of unsteadiness is beneficial in the context of absorbing unsteadiness at the compressor face. Local cancellation of unsteadiness may be sufficient at reducing unsteady blade loading in axial compressors. This benefit needs to be studied further, but it demonstrates the potential utility of feedback control to reduce unsteadiness in tactical aircraft inlets.

6.3   FUTURE WORK AND RECOMMENDATIONS

The results of the feedback control experiments demonstrate that it is feasible to reduce AIP distortion using downstream actuation. As a result, future work in this area of research is very promising. One avenue of future work is to explore the variables associated with the existing experimental setup. Many of the constraints that dictated the experimental conditions in this research were due to limitations in cost, time and equipment. These constraints led to simplifications in the experimental setup such as, the use of SISO control rather than MIMO control, the simplified design of the actuator injection duct, and the low quantity of unsteady sensors. Listed below are recommendations that address each of these limitations.

- Instead of using a SISO control system, convert to a MIMO system that uses each of the four actuators as an independent input. Increasing the number of inputs adds more degrees of freedom to reduce distortion. An interesting experiment using MIMO control would be to employ a single frequency controller on combinations of the unsteady measurements (hot-film, extent and magnitude) simultaneously. These experiments might aid in better understanding of the relationship between separation and AIP unsteadiness.

- Design and implement variations of the injection scheme. The actuator duct is designed to accommodate various injector duct geometries. The experiments in this thesis only test perpendicular injection towards the center of the duct. This scheme was designed to create 1-D acoustic waves. A simple, but potentially beneficial, change to the injection scheme is varying the injection angle.

- Improve the characterization of unsteadiness at the separation point. This might be possible by increasing the number of hot-film sensors in the separated region. Better characterization of the flow in the separated region is crucial for understanding the link between separation induced unsteadiness and AIP distortion.

- Redesign the probe locations in the sensor ring to concentrate on the upper region of the AIP. This region of the AIP is the location of the pressure deficit and it contains the highest concentration of unsteadiness. Therefore, it would be beneficial to locate as many sensors as possible in this region.

Future work may also provide answers to some of the questions that arose during the course of this research. One such question is the relationship between the frequency distribution of the unsteadiness and compressor stability. Improved characterization of the unsteadiness coupled with existing compressor stability models may lead to better a understanding of this relationship. Another question involves the relationship between the separation shedding frequency and mass flow. In this research, it was seen that the shedding frequency varies as the inlet mass flow increases, however, no strategy for characterizing this dependency has been formulated. Lastly, it may be beneficial to implement the compressor emulation control law developed in Chapter 3. Despite inaccuracies due to the simplicity of the 1-D acoustic model, it would be interesting to study the how emulation alters the AIP boundary condition.

APPENDIX A   OPERATIONAL PROCEDURES

A.1   EXPERIMENTAL PROCEDURE

Conducting a high Mach number experiment on the UCAV inlet requires the use of many systems, ranging from the De-Laval Compressor to the NASA Moog actuators. These systems require different timelines for start-up, and some systems are sequentially dependent on the activation of others. Because of the factors, the following operational checklist has been developed to ensure timely and proper start-up/shut-down of the experiment.

EXPERIMENT OPERATION CHECKLIST (Sequential Order):

Data Acquisition (2nd Floor Control):

___ Turn on Scani-valve, SDIU, and PC

___ Change directory to – E:/ZACK1

___ Enter SCANMANW to run AIP data acquisition (test run)

___ Turn on amplifiers (2310) and allow them to warm for 30 minutes, then complete the *I.C. Calibration Procedure (Section A.3)*

___ Record filter/gain settings in run book

___ Verify and record mapping from transducers to A/D panel

___ For 8 Channel Data Acquisition:

   Use shortcut to Record.exe on computer desktop

   Use Target 0, Module 0, A/D inputs 9-16

   Use active channel mask ff

___ For BDT Data Acquisition:

   Type MMADCAP at BDT computer "B" to start data acquisition program. (Seek assistance from Dr. Jerry Guenette to learn how to operate program.)

___ For Hot-film Data Acquisition

   1) Turn on Dantec amplifiers

   2) Set high-pass filter, low-pass filter and gain settings

   3) Note: DO NOT enable sensors until experiment is running

125

De-Laval Procedures 1:

___ Follow Section 1 of the De-Laval start-up instructions (these instructions should only include up to starting the De-Laval auxiliary oil pump)

___ Allow both the MG and Auxiliary Compressor oil pumps to warm up for at least 30 minutes

Oil Free Air (Basement Level 002):

___ Make sure both air supply valves in 2nd floor are closed before starting the oil free air compressor

___ Turn on Dryer located in the NW corner of basement

___ Turn on cooling water valve located on wall next to oil free air compressor in SE corner of basement

___ Sign the compressor logbook

___ Turn oil free compressor on (allow compressor to run 15 minutes before using air)

Mass Flow Plug Control (2nd Floor Control):

___ Turn on DC power supply located on floor next to Scani-valve (Adjust supply voltage to vary plug motor speed, suggested range is 12-20 V)

___ Turn on yellow multi-meter

___ Use plug control panel, next to monitor, to set plug in fully open condition (9.2 V)

Moog Control Panel (2nd Floor Control):

___ Make sure that the HV Power Command is set to DISABLE

___ Turn on 230A switch (located on column behind Moog tower)

___ Turn on Sorenson power switches

___ Turn on Main power switch

___ Verify that there is an external input command to channels 1, 2, 3, and 5 (actuators are ready for use, but do not enable them until the air supply is turned on or unless you are testing the actuator position)

Butterfly Valve (2nd Floor):

___ Set Butterfly valve position to 100 percent

___ Warn any persons in the valve room of the impending noise (advise the use of ear protection)

De-Laval Procedures 2:

___ Complete Sections 2 & 3 on the De-Laval start-up sheet (NOTE: before starting the compressor, make sure that the butterfly valve is at 100 percent open and the plug is at 9.2 V)

126

Final Start-up Procedures:

___ With compressor idling at 1000 RPM:

    ___ Open both air supply valves to the actuators

    ___ Set regulator to desired pressure

    ___ Enable actuators (if desired, check actuator position to verify good operation)

___ After 5 minutes of idling, increase compressor to desired speed (for choked flow, use 4300 RPM)

___ Close butterfly valve to 50 percent

___ Run SCANMANW to verify that plug is choked (NOTE: if compressor pressure ratio exceeds 2.65, then open butterfly valve by increments of 5 percent until ratio is below 2.60)

Shutdown Procedure:

___ Follow the start-up procedure, in reverse order, to properly shut down the system. Listed below are reminders of the critical shutdown procedures:

    ___ 1) While the compressor is operating at full speed, open plug to max position (9.2 V) and open butterfly valve to 100 percent. **CAUTION! If you reduce compressor speed before opening these inlets, then the building might blow up!**

    ___ 2) Before shutting off the supply air regulator, DISABLE the actuators.

    ___ 3) Allow compressor to idle at 1000 RPM for 5 minutes during shutdown

    ___ 4) Allow MG oil pump and compressor auxiliary pump to run for 30-60 minutes after final shut-down

    ___ 5) After closing the air supply regulator, close the two air supply valves, then open the regulator to bleed off the compressed air

A.2   DE-LAVAL OPERATING PROCEDURE

This section describes how to properly operate the turbomachinery involved in operating the De-Laval compressor for high Mach number inlet experiments. MIT facilities maintain the De-Laval compressor system, and the start-up procedure checklist is the responsibility of the GTL Lab Manager (currently William Ames).

For the scaled UCAV inlet, the desired mass flow ranges from *2.5-3.7 lb/s*. To choke the Northrop Grumman throttle plug the throttle pressure ratio must be greater than two. Achieving this throttle pressure ratio requires the compressor inlet pressure to be approximately *7.0 psi* or less. For the De-Laval compressor to achieve this compressor inlet pressure the compressor pressure ratio must be

approximately 2.5-2.6 (depending on the ambient conditions). The De-Laval compressor can operate at this pressure ratio range; however, the mass flow must be high enough to prevent surge. Figure A.1 shows the operating lines for various compressor speeds. The mass flow factor (MFF) is the corrected mass flow through the compressor. Given the ambient conditions during operation, conversion between actual mass flow and the mass flow factor is given by equation A.1.

$$\dot{m}_C = \frac{MFF \cdot P_{C_{IN}}}{2.665 \times 10^{-3} \sqrt{T_{C_{IN}}}}$$

(A.1)

At the normal operating condition of the experiment, see Figure A.1, the compressor mass flow is approximately 8.0 lb/s. Since the Northrop throttle range is between 2.5-3.7 lb/s a secondary inlet source is necessary to run the experiments. The alternate mass flow source is the butterfly valve located in the GE swirl test facilities cell. By closing the butterfly valve, the mass flow though the system decreases and the pressure ratio across the compressor increases. Table A.1 describes the important operating conditions during the high Mach number experiments. To properly achieve these operating conditions it is necessary to follow both the Experimental Procedures (Section A.1) and the De-Laval Start-up Procedures.
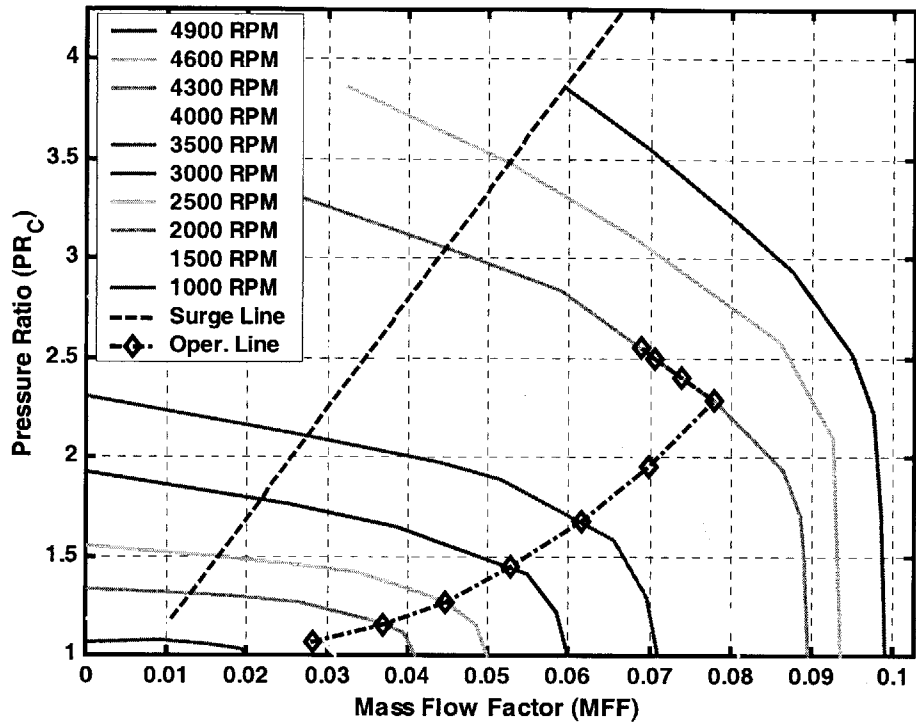
Figure A.1 – De-Laval Operating Chart

The diamonds in Figure A.1 represent the operating point measurements taken during the mapping of the De-Laval compressor. For a typical flow control experiment, the compressor is immediately brought up to full speed, *4300 RPM*, without stopping at the intermediate speeds.

Parameter	Value	Description
T_∞	~73 °F (533 °R)	Ambient Air Temperature
P_∞	~14.7 psi	Ambient Air Pressure
$T_{C_{IN}}$	60 - 75 °F	Compressor Inlet Temperature
$P_{C_{IN}}$	~7.00 psi	Compressor Inlet Pressure
$\dot{m}_C$	~8.0 lb/s	De-Laval Compressor Mass Flow
$\dot{m}_P$	2.5 - 3.7 lb/s	Throttle Plug Mass Flow
ω_C	4300 RPM	Compressor Angular Speed
PR_C	2.50 - 2.65	Compressor Pressure Ratio
$T_{C_{OUT}}$	280 - 300 °F	Compressor Exit Temperature

PR_P	2.05 - 2.15	Throttle Plug Pressure Ratio
T_{OIL}	125 °F MAX	De-Laval Oil Temperature
MFF	~0.070	Mass Flow Factor
I_C	1200 - 1300 A	Compressor Motor Current
V_C	400 – 410 V	Compressor Motor Voltage
β	50 - 55 %	Butterfly Valve Percentage Open

Table A.1 – De-Laval Compressor Operating Conditions during the Experiments

A.3   UNSTEADY CAN CALIBRATION PROCEDURE

This section describes how to properly calibrate the pressure transducers within the unsteady instrument can. Figure A.2 illustrates the setup used to calibrate the transducers. It is important to check the plumbing of the system before each calibration, especially the tubing that supplies the IC plenum and the tubing from the plenum to each transducer. Any pressure leak in the system will make accurate calibration impossible.
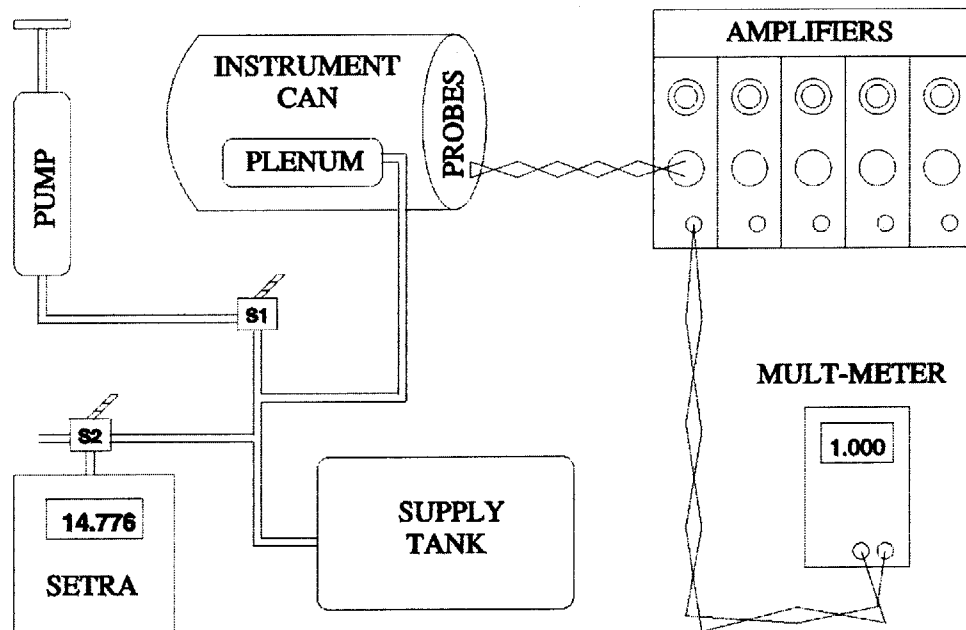
Figure A.2 – Unsteady I.C. Calibration Setup

DETAILED CALIBRATION PROCEDURE:

Pre-calibration Steps:

1) Turn on amplifiers to be used during experiment.

2) Record mapping from amplifier to transducer.

3) Set Gain multiplier to 100, and set filter to desired level.

4) Turn amplifier excitation on.

5) Allow amplifiers to "warm up" for 30 minutes before calibration. This ensures that the transducer bridge circuitry has reached thermal equilibrium. NOTE: it is advised to balance the amplifiers, using the auto-balance reset switch, periodically during "warm up".

6) Make sure AC Coupling is disabled.

Calibration Steps (time critical):

NOTE: Calibrate the transducers in groups of 5. This is recommended because the amplifiers drift and the back pressure plenum leaks slowly. Thus, calibrating in groups of 5 (corresponding to one instrument can rake at a time) reduces drift error.

7) Balance the amplifiers of interest using the auto-balance reset switch and the fine trim knob.

8) Attach the pressure supply tube to the Kulite plenum.

9) Open valve #1 (S1 in Figure A.2), and pump the supply tank to a pressure approximately 2 psi above atmospheric. Quickly close valve #1.

10) Use valve #2 (S2 in Figure A.2) to toggle between atmospheric and supply pressure.

11) Use valve #1 to bleed pressure from the supply tank. Bleed pressure until the supply pressure is exactly 1.00 psi greater than atmospheric. Make sure the pressure is stable (if pressure drops rapidly look for leaks in the system).

12) Once the supply pressure is fixed, plug the output from the amplifier of interest into a digital multi-meter.

13) Adjust the amplifier gain until the output voltage is exactly 1.000 V. Repeat this step for all 5 amplifiers in the group.

14) After all 5 transducers are calibrated; remove the pressure supply tube from the Kulite plenum located on the IC.

15) Repeat steps 7-14 for until each group of transducers is calibrated.

A.4   CONTROLLING THE THROTTLE PLUG

The Northrop Grumman throttle plug sets the mass flow through the UCAV inlet by varying the choked area in the throttle. The choked area varies by traversing a cone shaped plug axially along the throttle axis. Traversing the plug forward, towards the inlet, reduces the choked area, thus reducing the mass flow through the throttle. To traverse the plug, an external voltage must be supplied to the plug motor. Applying a positive voltage to the motor traverses the plug forward, while a negative voltage traverses the plug backwards. The plug position is a function of the output signal voltage from the plug when supplied with twelve volts across its sense circuit. Figure A.3 is a schematic of the throttle plug control system. The output signal from the plug is displayed on a digital multi-meter. The three-way switch in Figure A.3 controls the polarity of the motor voltage thus determining if the plug is to be opened or closed. Pressing the button next to the three-way switch performs the actual traversing of the plug. Changing the DC supply voltage to the plug motor may vary the speed at which the plug traverses. Lowering the motor voltage results in a decreased traversing speed.
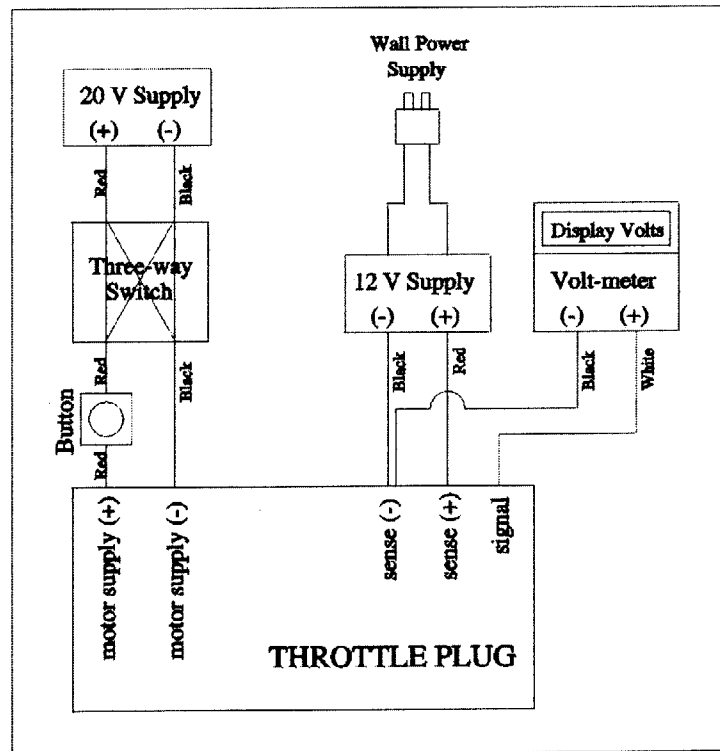
Figure A.3 – Throttle Plug Control System Schematic

APPENDIX B FABRICATION DRAWINGS

This appendix contains the drawings necessary to fabricate MIT's contribution to the scaled UCAV experimental rig. Of the parts designed at MIT, only the total pressure probes were fabricated in the GTL machine shop. The actuator duct and the sensor ring were outsourced to local machinists.
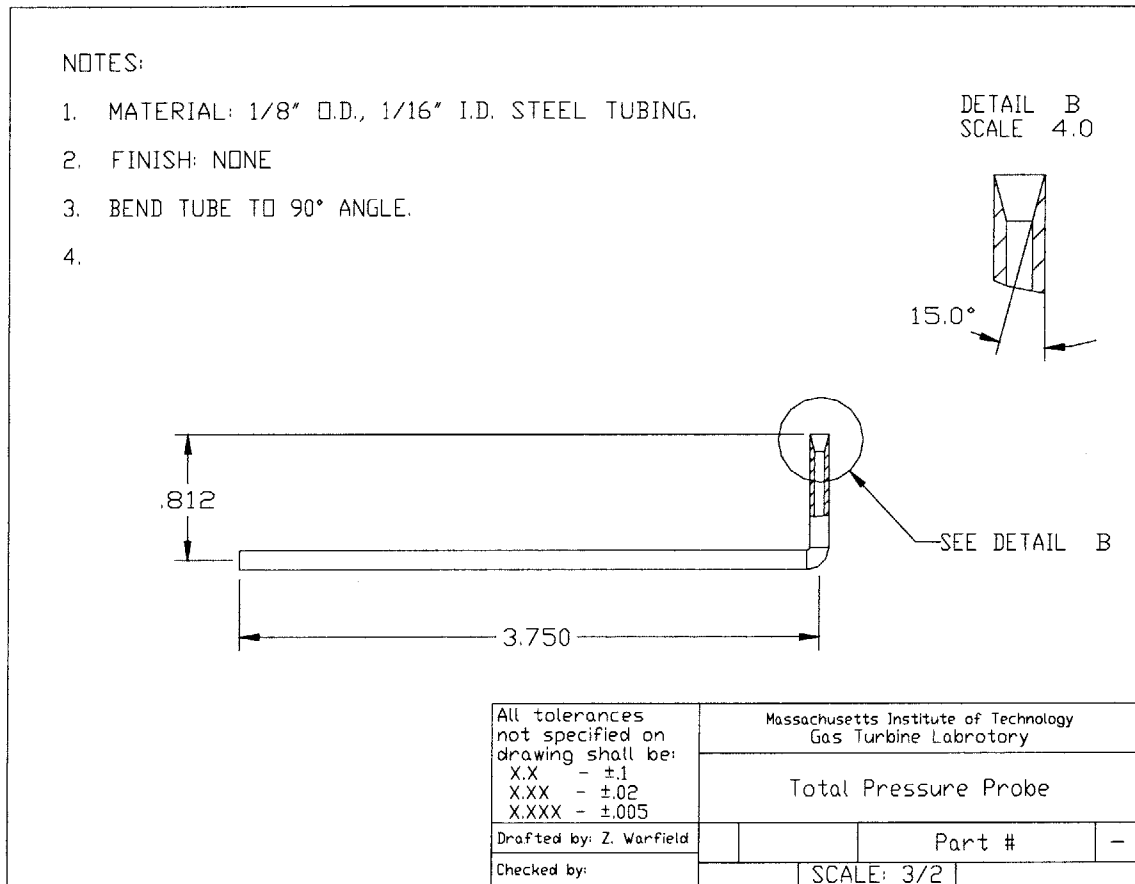
Figure B.1 – Total Pressure Probe Fabrication Drawing

Figure B.2 – Actuator Duct Fabrication Drawing (Sheet 1)

134
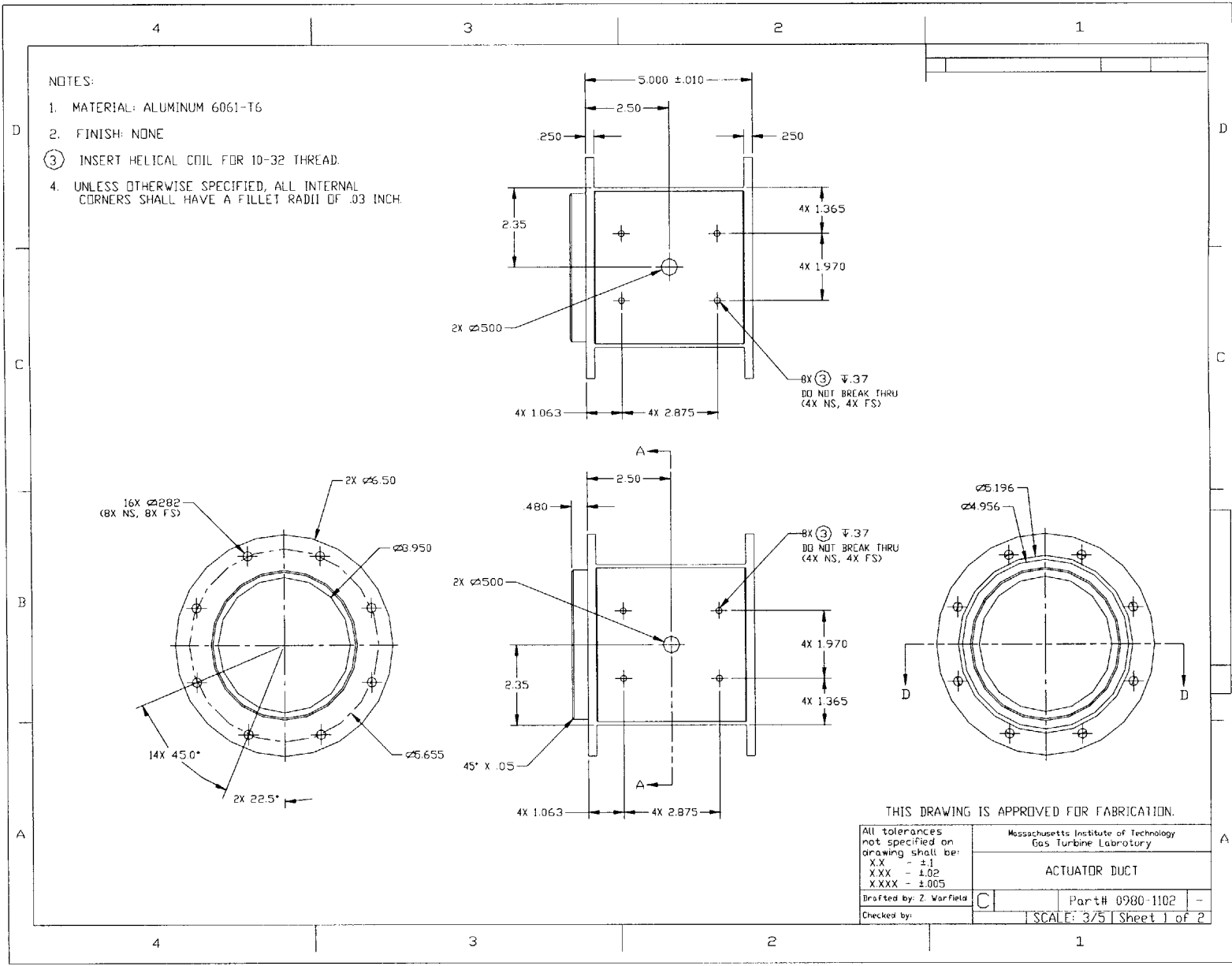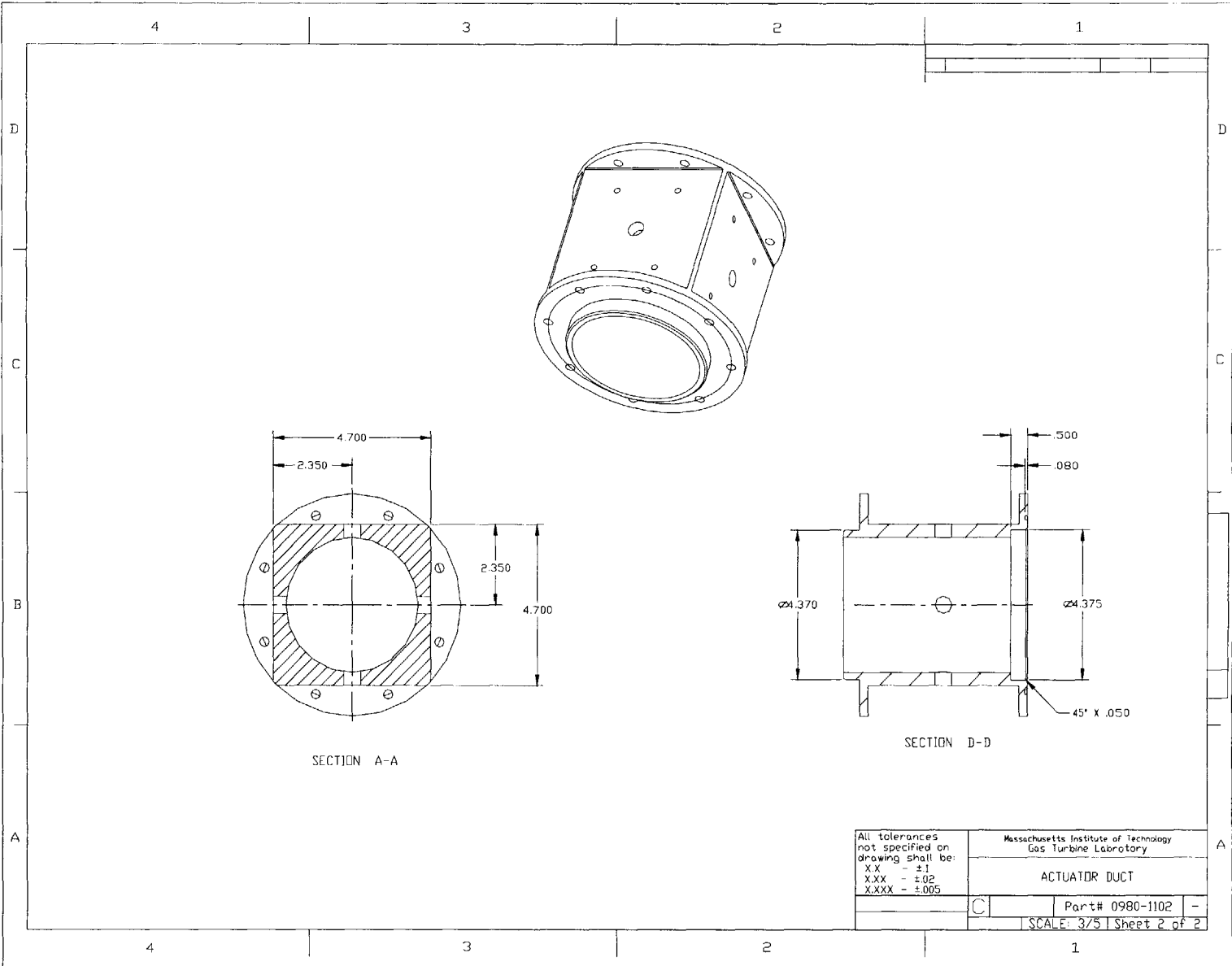
Figure B.3 – Actuator Duct Fabrication Drawing (Sheet 2)

135

SECTION A-A

4.700
2.350
2.350
4.700

SECTION D-D

.500
.080
Ø4.370
Ø4.375
45° X .050

Figure B.4 – Sensor Ring Fabrication Drawing

136

NOTES:

1. MATERIAL: ALUMINUM 6061-T6

2. FINISH: NONE

8X Ø.125 THRU
1/8 PIPE THREAD ▼.50

8X .900

A

8X 45.0°

Ø5.300

R.03 — 1.800 —

.080

.120

45° X .050

Ø3.950

Ø5.196

Ø4.370

Ø4.375

R.03

45° X .05

.480

.500

SECTION A-A

THIS DRAWING IS APPROVED FOR FABRICATION.

All tolerances
not specified on
drawing shall be:
X.X   = ±.1
X.XX = ±.02
X.XXX = ±.005

Massachusetts Institute of Technology
Gas Turbine Labrotory

SENSOR RING

Drafted by: Z Warfield   C   Part# 0980-1104   —

Checked by: SCALE: 1/1

APPENDIC C LINEARIZED BULK PARAMETERS
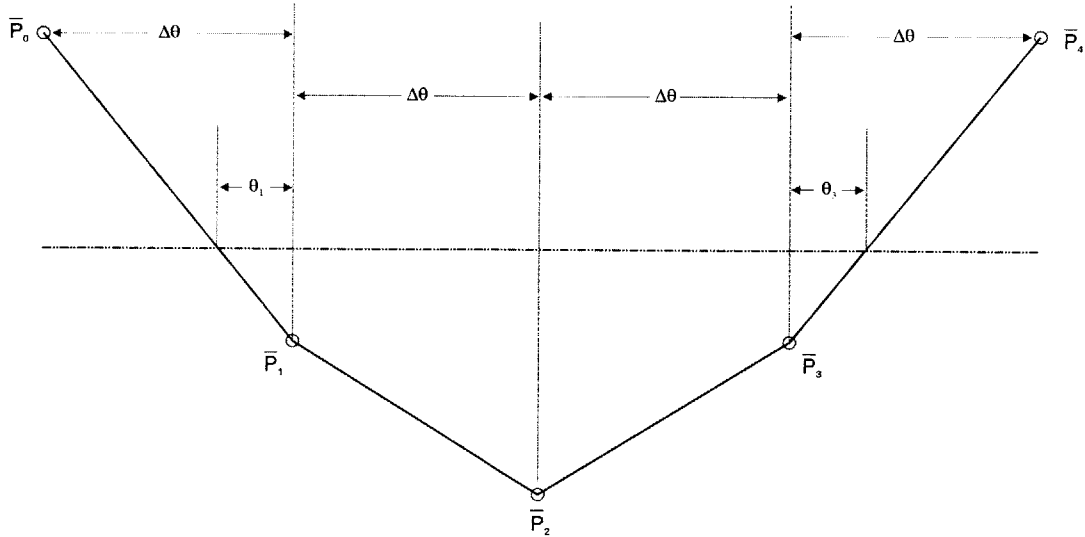
Figure C.1 – Linearized Bulk Parameter Schematic

The purpose of linearizing the bulk parameters is to formulate a series of constant coefficients such that each bulk parameter is linear sum of the unsteady pressure measurements multiplied by a set of coefficients. Equations C.1 and C.2 describe the linearized perturbations of extent, Θ, and magnitude, A, respectively.

$$\delta\Theta = \sum_{i=0}^{4} \alpha_i \cdot \delta P_i$$

(C.1)

$$\delta A = \sum_{i=0}^{4} \beta_i \cdot \delta P_i$$

(C.2)

137

To simplify the calculation of the bulk parameters, only five total pressure measurements are used. Each of these total pressure measurements is normalized about the mean value, P_{AVG}, as shown in equation C.3. This simplification does not affect the calculation of the coefficients because the average pressure is assumed to be constant over time. Equation C.3 defines the normalized total pressure for each of the five rakes.

$$\overline{P}_i = P_i - P_{AVG}$$

(C.3)

The total pressure probes used in the bulk parameter determination are evenly spaced circumferentially within the sensor ring at $45°$ intervals. The center probe, P_3, is located in the top center of the sensor ring $(90°)$. The remaining probes are located with respect to P_3 according to Figure C.1. As for radial location, each pressure probe is located at a radius of *1 1/16 inches*. This optimal radial location was chosen based on the unsteady results of experiments using the unsteady instrument can. Of these five total pressures only the inner three, P_1, P_2 and P_3, are time varying. The remaining two pressures, P_0 and P_4, serve as steady anchors to bound the unsteady pressures and allow for the calculation of extent and magnitude.

C.1 EXTENT

As seen in Figure C.1, the extent is defined as the angular span between the intersections of the average pressure line and the linear interpolations between the time varying total pressures. To maintain a linear relationship between extent and magnitude, it is assumed that P_1 and P_3 are less than P_{AVG} and the total pressure perturbations are small relative to the normalized pressures.

$$\Theta = 2\Delta\theta + \theta_1 + \theta_3$$

(C.4)

Given these assumptions, equation C.4 describes the extent, where $\Delta\theta$ is the constant angular increment between probes and θ_1 and θ_3 are the angular variations due to pressure perturbations.

$$\theta_1 = -\left(\frac{\overline{P_1}}{\overline{P_0} - \overline{P_1}}\right)\Delta\theta$$

<div align="right">(C.5)</div>

$$\theta_3 = -\left(\frac{\overline{P_3}}{\overline{P_4} - \overline{P_3}}\right)\Delta\theta$$

<div align="right">(C.6)</div>

Substituting equations C.5 and C.6 into equation C.4 and taking the derivative of extent with respect to the time varying pressures, P_1 and P_3, determines the perturbation in extent. Notice that the perturbation of extent does not depend on the perturbation of P_2. A comparison of equations C.7 and C.1 determines the linearized coefficients of extent, α_i (see Table C.1).

$$\delta\Theta = -\left(\frac{\Delta\theta \cdot \overline{P_0}}{\left(\overline{P_0} - \overline{P_1}\right)^2}\right)\delta P_1 - \left(\frac{\Delta\theta \cdot \left(\overline{P_4}\right)}{\left(\overline{P_4} - \overline{P_3}\right)^2}\right)\delta P_3$$

<div align="right">(C.7)</div>

C.2 MAGNITUDE

The magnitude bulk parameter, A, is defined as the area between the P_{AVG} line and the total pressure curve within the boundaries of the extent. From Figure C.1 the magnitude is found by using the formula for the area of a triangle on the outer sections and the area of a trapezoid for the inner two sections.

$$A = -\frac{\Delta\theta}{2}\left(\overline{P_1} + 2\overline{P_2} + \overline{P_3}\right) - \frac{1}{2}\theta_1\overline{P_1} - \frac{1}{2}\theta_3\overline{P_3}$$

<div align="right">(C.8)</div>

Substituting equations C.4 and C.5 into equation C.8 yields a formula for the magnitude that is dependent solely on the pressure variations.

$$A = -\frac{\Delta\theta}{2}\left(\overline{P_1} + 2\overline{P_2} + \overline{P_3}\right) + \frac{\Delta\theta\overline{P_1}^2}{2\left(\overline{P_0} - \overline{P_1}\right)} + \frac{\Delta\theta\overline{P_3}^2}{2\left(\overline{P_4} - \overline{P_3}\right)}$$

$$(\text{C.9})$$

Like extent, the perturbation in magnitude is found by taking the partial derivatives of magnitude with respect to P_1, P_2 and P_3. After reorganizing the terms, a comparison of equations C.10 and C.2 determines the linearized coefficients of magnitude, β_i (see Table C.1).

$$\delta A = -\frac{\Delta\theta}{2}\left(\delta P_1 + 2\delta P_2 + \delta P_3\right) + \delta P_1\Delta\theta\left(\frac{\overline{P_1}}{\left(\overline{P_0} - \overline{P_1}\right)} + \frac{\overline{P_1}^2}{2\left(\overline{P_0} - \overline{P_1}\right)^2}\right) + \delta P_3\Delta\theta\left(\frac{\overline{P_3}}{\left(\overline{P_4} - \overline{P_{31}}\right)} + \frac{\overline{P_3}^2}{2\left(\overline{P_4} - \overline{P_3}\right)^2}\right)$$

$$(\text{C.10})$$

Table C.1 lists the coefficients used in the linearized bulk parameter calculations. The values of absolute total pressure, P_i, were chosen based on previous steady pressure experiments to best classify the system. These pressures will vary depending on mass flow and experimental configuration; however, the relative effect on the coefficients is negligible.

i	P_i	$\overline{P_i}$	Bulk Parameter Coefficients	
			Extent - α_i	Magnitude - β_i
0	14.7 psi	0.7 psi	N/A	N/A
1	13.7 psi	-0.3 psi	$-\dfrac{\Delta\theta \cdot \overline{P_0}}{\left(\overline{P_0} - \overline{P_1}\right)^2} = -0.175\pi$	$\Delta\theta\left(\dfrac{\left(\overline{P_0}\,\overline{P_1} - 0.5\overline{P_1}^2\right)}{\left(\overline{P_0} - \overline{P_1}\right)^2} - \dfrac{1}{2}\right) = -0.189\pi$
2	13.2 psi	-0.8 psi	0	$-\Delta\theta = -0.250\pi$
3	13.7 psi	-0.3 psi	$-\dfrac{\Delta\theta \cdot \overline{P_4}}{\left(\overline{P_4} - \overline{P_3}\right)^2} = -0.175\pi$	$\Delta\theta\left(\dfrac{\left(\overline{P_4}\,\overline{P_3} - 0.5\overline{P_3}^2\right)}{\left(\overline{P_4} - \overline{P_3}\right)^2} - \dfrac{1}{2}\right) = -0.189\pi$
4	14.7 psi	0.7 psi	N/A	N/A

Table C.1 – Linearized Bulk Parameter Coefficients

C.3   TRIGONOMETRIC VERIFICATION OF EXTENT

To verify the derivation of the lineraized bulk parameters, the coefficients for extent were re-calculated using trigonometric techniques. Figure C.2 shows the relationship between a variation in the pressure, P_I, and the angular variation.
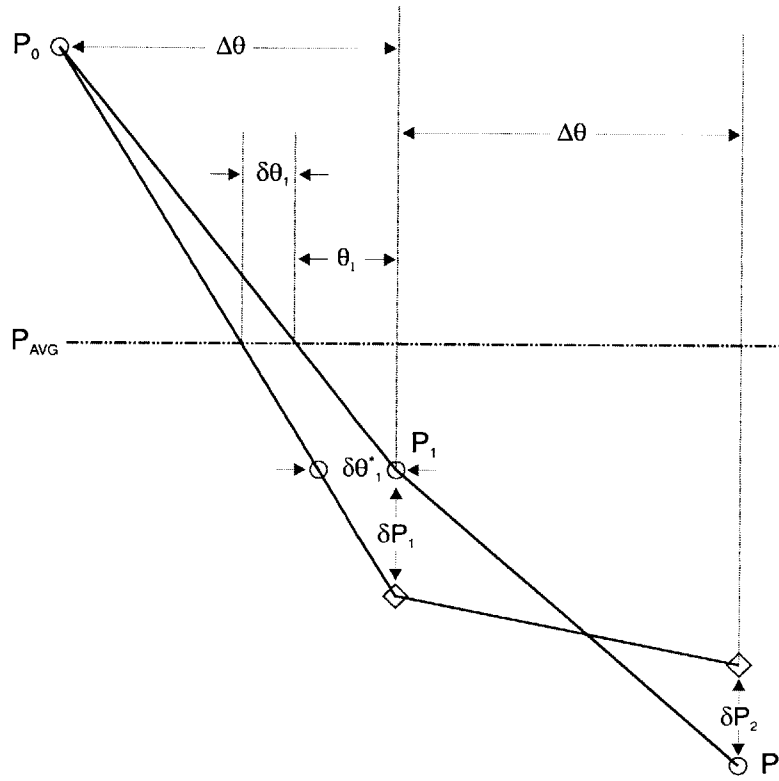
Figure C.2 – Trigonometric Extent Derivation

Assuming a small change in pressure, then by similar triangles equation C.11 describes the relationship between pressure variation, δP_I, and the angular variation at P_I, $\delta\theta_I{}^*$.

$$\frac{\delta\theta_1^*}{\delta P_1} \approx \frac{\Delta\theta}{\left(P_0 - P_1\right)}$$

<div align="right">(C.11)</div>

Once again similar triangles are used to relate the angular variation at P_1 to the angular variation at P_{AVG}, $\delta\theta_1$. Solving for $\delta\theta_1^*$ in equation C.11 and substituting into equation C.12 yield an expression for $\delta\theta_1$ in terms of the pressure variation.

$$\frac{\delta\theta_1}{\left(P_0 - P_{AVG}\right)} \approx \frac{\delta\theta_1^*}{\left(P_0 - P_1\right)}$$

(C.12)

$$\delta\theta_1 \approx \frac{\Delta\theta \cdot \left(P_0 - P_{AVG}\right)}{\left(P_0 - P_1\right)^2} \delta P_1$$

(C.13)

Equation C.13 is identical to the linearized coefficient α_1, in Table C.1. Thus the derivation of the bulk parameter coefficients is validated.

APPENDIX D   MATLAB CODES

D.1   1-D ACOUSTIC MODEL

```
%%%%%%%%%%%%%%%%%%%%%%%%%%%%%%%%%%%%%%%%%%%%%
% Continuous Acoustic Model of UCAV Inlet   %
% "exp_acoustic_model.m"
%                                           %
% -> Based on the Model of Brandon Gordon   %
% By: Zack Warfield                         %
%%%%%%%%%%%%%%%%%%%%%%%%%%%%%%%%%%%%%%%%%%%%%

close all
clear all

%%%%% Input Options %%%%
disp('   ');
resp1 = input('Fit Transfer Function? [y or n] ','s');
resp2 = input('Perform Compressor Emulation? [y or n] ','s');
disp('   ');

%%%%%%%%%%%%%%%%%%%%%%%%%
% Order of Module
% Type order of Modules
% in variable "ord"
%%%%%%%%%%%%%%%%%%%%%%%%%
bell = 1; diff = 2; s_ring = 3; i_c = 4; act = 5;
ord = [bell, diff, i_c, act];          % Order of components in model
[dist,order,probe,actuator,AIP,x] = duct_length(ord);

%%%%%%%%%%%%%%%%%%%%%%%%%
% Dicretize
% Each Model
%%%%%%%%%%%%%%%%%%%%%%%%%
rho_ref = 1.200;                  % Reference Air Density
a_ref = 340.3;                    % Reference Speed of SOund
L_ref = max(dist);                % Reference Length
Area_ref = 0.25*pi*(3.95/39.4)^2;     % Reference Area

%%%% Determine Properties for each Discretized Section %%%%
for (i = 1:length(x)-1)
    xmid = (x(i+1) + x(i))/2;
    L(i) = x(i+1) - x(i);
    [Area(i),M(i)] = exp_AM(order,xmid,dist);
    rho(i) = 1.0/(1+.2*M(i)^2)^3.5;        % Air Density [kg/m^3]
    a(i) = sqrt(1.0/(1+.2*M(i)^2));         % Speed of Sound [m/s]
    incr = i;
end
L = L/L_ref;    % Non-dimensionalize length

%%%%%%%%%%%%%%%%%%%%%%%%%%%%%%%%%%%%%%%%%%%%%%%%
%%% TRANSMISSION MATRIX OF ACOUSTIC SURGE %%%
%%%%%%%%%%%%%%%%%%%%%%%%%%%%%%%%%%%%%%%%%%%%%%%%

%%%%%%%%%% Air Injector Vector %%%%%%%%%%%%
Ainj = pi*(.5/39.4)^2        % Normalized Injector Area
phi_i = 0.20;                % Air Mass Flow at Plenum Inlet [lb/s]
phi_0 = 3.19;                % Mass flow throught system [lb/s]
Ay = phi_i/phi_0;
```

```
v0(1,1) = 0;
v0(2,1) = Ay;

%%%%% Throttle Plug Setion Parameters %%%%%
mT = 10.0;              % Throttle coefficient
rho_plug = rho(incr);
a_plug = a(incr);
Tplug = T_thrt(rho_plug,a_plug,mT);

%%%%%%% System Transmission Matrices %%%%%%%
n = 250;
wr = 2*pi*linspace(20,550,n);

T_inc = zeros(2,2,incr);
T = zeros(2,2);
V = zeros(2,2);

%%%%%%%%%%%%%%%%%%%%%%%%%%%%%%%%%%%%%%%%%%%%%
% Loop that performs the impedance and
% injection relationship for the experimental
% model.  The equations below follow the
% equations of Chapter 3.
%%%%%%%%%%%%%%%%%%%%%%%%%%%%%%%%%%%%%%%%%%%%%
for k = 1:n,
    w = (L_ref/a_ref)*wr(k);    % Non-dimensional frequency
    T = eye(2);
    U = eye(2);
    F = eye(2);
    for i = 1:incr
        T_i = T_acdm(w,rho(i),L(i),a(i),M(i));
        T_inc(:,:,i) = T_i(:,:);
        T = T*T_i;
        if (i < probe)
            V = T;
        end
        if (i >= actuator)
            U = U*T_i;
        end
        if (i >= AIP & i < actuator)
            F = F*T_i;
        end
    end

    % Calculate Probe to Actuator Transfer Functions
    T = Tplug*T;
    F = Tplug*F;
    Uh = Tplug*U;
    U = Tplug*U*v0;
    Vp = [1 1; 0 1]*V;
    gs(k) = -V(1,2)*U(1,1)/T(1,2);
    gt(k) = -Vp(1,2)*U(1,1)/T(1,2);

    % Calculate Impedence of Experiment from AIP to Exit
    D = inv(F)*inv(Uh);
    E = inv(F)*v0;
    Zd(k) = D(1,2)/D(2,2);
    Zd_mod(k) = (Zd(k)*E(2) - E(1));
end

g = [gs' gt'];
f = wr/(2*pi)';
phase = angle(gs)';
mag = abs(gs)';

%%%% Plot Ourput as Transfer Functions %%%%
figure(1)
g = subplot(211);
```

```
h = plot(f,20*log10(mag))
12 = ylabel('magnitude [dB]');
grid
set(g,'LineWidth',1.5,'FontWeight','demi','FontSize',12);
set(h,'LineWidth',1.5);
set(12,'Fontsize',11,'FontWeight','demi');
g = subplot(212);
h = plot(f,180/pi*(phase));
11 = xlabel('frequency [Hz]');
12 = ylabel('phase [deg]');
grid
set(g,'LineWidth',1.5,'FontWeight','demi','FontSize',12);
set(h,'LineWidth',1.5);
set(11,'Fontsize',11,'FontWeight','demi');
set(12,'Fontsize',11,'FontWeight','demi');

if (resp1 == 'y')
    %%%%%%%%%%%%%%%%%%%%%%%%%%%%%%%%%%%%%%%%%%%
    % Fit Transfer Function
    %%%%%%%%%%%%%%%%%%%%%%%%%%%%%%%%%%%%%%%%%%%
    [numgt,dengt] = invfreqs(gt,wr,10,12);
    [A,B,C,D] = tf2ss(numgt,dengt);
    sysgt = ss(A,B,C,D);
    sysgt = canon(sysgt,'modal');
    [At,Bt,Ct,Dt] = ssdata(sysgt);
    [B,A] = ss2tf(At,Bt,Ct,Dt);
    gtf = freqs(B,A,wr);

    g2 = [gt' gtf'];
    phase2 = angle(g2)';
    mag2 = abs(g2)';

    figure(2)
    subplot(211)
    plot(f,20*log10(mag2));
    title('Psi_4 / Phi_I Transfer Function for Acoustic Duct Model');
    ylabel('magnitude [dB]');
    legend('Real','Fitted')
    subplot(212)
    plot(f,180/pi*(phase2));
    xlabel('frequency [Hz]');
    ylabel('phase [deg]');
    legend('Real','Fitted')

    save GZ B A
end

if (resp2 == 'y')
    %%%%%%%%%%%%%%%%%%%%%%%%%%%%%%%%%%%%%%%%%%%
    % Perform Compressor Emulation
    %%%%%%%%%%%%%%%%%%%%%%%%%%%%%%%%%%%%%%%%%%%

    %%%%%%% Compressor Inputs for Emulation %%%%%%%%
    a1 = 340.00;              % Speed of Sound at Inlet [m/s]
    a2 = 488.00;              % Speed of Sound in Diffuser [m/s]
    a3 = 699.00;              % Speed of Sound in Plenum (assumed) [m/s]
    Vol = 0.01620;            % Volume of the Plenum [m^3]

    A2 = .25*pi*(3.95/39.4)^2;    % Plenum Exit Area [m^2]
    A1 = 3*A2;                    % Plenum Entrance Area [m^2]
    Aref = A1;                    % Area of Reference Plenum (inlet) [m^2]
    Ainj = 4*pi*(.25/39.4)^2;     % Area of the Injector Duct [m^2]

    mT = 10.0;                % Slope of Throttle Characteristic
    tau = 0.2;                % Compressor Delay [sec?]
    Lfactor = 1.5;            % Compressor Loss Factor
    mC = 2.0 - Lfactor;       % Slope of Compressor Characteristic
```

```
L1 = 0.5;                   % Effective Length of Inlet [m]
L2 = 0.35;                  % Effective Length of Diffuser [m]
Lplenum = 0.385;            % Effective Length of Plenum [m]

%%% TRANSMISSION MATRIX OF ACOUSTIC SURGE %%%

%%%%%%%%%% Reference Parameters %%%%%%%%%%%
L_ref = L1 + L2;
a_ref = a3;

%%%%%%%% Non-dimensional Parameters %%%%%%%%
Aplenum = Vol/Lplenum;      % Equivalent Area of Plenum [m^2]

%%%%%%%%%%%%%% Compressor 23 %%%%%%%%%%%%%%%%
rho_23 = 1.0;               % Assume rho_comp = rho_inlet
a_23 = a1/a_ref;            % Assume a_23 = a_12
mc_23 = mC;
dpsiC_dphiC = 1;
%%%%%%%%%%%%%%%% Plenum 34 %%%%%%%%%%%%%%%%%%
rho_34 = 8.0*a1^2/a3^2;     % Use Density Ratio Formula
L_34 = Lplenum/L_ref;
a_34 = a3/a_ref;
a0_34 = A1/Aplenum;
a1_34 = Aplenum/Aplenum;

%%%%%%%%%%%%%%% Throttle 45 %%%%%%%%%%%%%%%%%
rho_45 = rho_34;            % Assume rho_thrt = rho_plenum
a_45 = a3/a_ref;            % Assume a_thrt = a_plenum

%%%%%%% System Transmission Matrices %%%%%%%
for k=1:n,
    w = (L_ref/a_ref)*wr(k);        % Non-dimensional frequency
    phiC_psi2(k) = 0;

    T23 = T_comp(rho_23,a_23,mc_23);
    T34 = T_plen(w,rho_34,L_34,a_34,a0_34,a1_34);
    T45 = T_thrt(rho_45,a_45,mT);

    T23i = inv(T23);
    T34i = inv(T34);
    T45i = inv(T45);

    % Calculate Compressor Impedances
    v0 = [dpsiC_dphiC; Ay];
    C = T23i*v0;
    B = T23i*T34i*T45i;
    Zc(k) = B(1,2)/B(2,2);
    Zc_inj(k) = Zc(k)/(1-(Zc(k)*C(2)-C(1))*phiC_psi2(k));

    % Calculate Transfer Function for Compressor Emulation
    phiI_psiAIP(k) = (Zc_inj(k)-Zd(k))/(Zc_inj(k)*Zd_mod(k));
    Zd_inj(k) = Zd(k)/(1-Zd_mod(k)*phiI_psiAIP(k));
end

%%%% Plot TF for Compressor Emulation %%%%
phase3 = angle(phiI_psiAIP)';
mag3 = abs(phiI_psiAIP)'
figure(2)
subplot(211)
plot(f,20*log10(mag3));
title('Phi_I / Psi_{AIP} Transfer Function to Emulate Compressor');
ylabel('magnitude [dB]');
subplot(212)
plot(f,180/pi*(phase3));
xlabel('frequency [Hz]');
ylabel('phase [deg]');
end
```

```
%%%%%%%%%%%%%%%%%%%%%%%%%%%%%%%%%
% Function that empirically
% determines the area and
% Mach # for each component in
% the UCAV.
%%%%%%%%%%%%%%%%%%%%%%%%%%%%%%%%%
function [A,M] = exp_AM(order,x,dist)

newdist = [0,dist];
for i = 1:length(dist)
    if x > newdist(i)
        xmin = newdist(i);
        xmax = newdist(i+1);
        section = i;
    end
end

xdiff = xmax - xmin;
xnorm = x - xmin;
component = order(section);

switch component
case 1
    Ain = 36.0;
    Aout = 12.0;
    A = Aout + (Ain-Aout)*((xdiff-xnorm)/xdiff)^4;
    M = 0.15 + 0.4*((Ain-A)/(Ain-Aout))^1.5;
case 2
    Ain = 12.0;
    Amid = 10.45;
    Aout = (pi/4)*3.95^2;
    xmid = 4.5/39.4;
    if xnorm < xmid
        A = Ain + (Amid-Ain)*xnorm/xmid;
        M = 0.55 + 0.10*xnorm/xmid;
    else
        A = Amid + (Aout-Amid)*(xnorm-xmid)/(xdiff-xmid);
        M = 0.65 - 0.15*(xnorm-xmid)/(xdiff-xmid);
    end
case 3
    A = (pi/4)*3.95^2;
    M = 0.5;
case 4
    Ain = (pi/4)*3.95^2;
    Aout = (pi/4)*4.5^2;
    A = Ain + (Aout-Ain)*xnorm/xdiff;
    M = 0.5;
case 5
    A = (pi/4)*3.95^2;
    M = 0.5;
end

A = A/(39.4)^2;


%%%%%%%%%%%%%%%%%%%%%%%%%%%%%%%%%
% Function that detemines the
% loaction and length of each
% component in the UCAV setup.
%%%%%%%%%%%%%%%%%%%%%%%%%%%%%%%%%
function [dist,order,probe,actuator,AIP,x] = duct_dist(ord)

s = 0;
x = 0;
probe = 0;
actuator = 0;
for j = 1:length(ord);
    switch ord(j)
```

147

```
    case 1
        s = s + 13.0;
        dist(j) = s;
        order(j,1) = ord(j);
        nsec(j) = 10;
        x = [x linspace(13.0/nsec(j),dist(j),nsec(j))];
    case 2
        s = s + 12.0;
        dist(j) = s;
        order(j,1) = ord(j);
        nsec(j) = 8;
        x = [x linspace(dist(j-1)+4.5/nsec(j)*2,dist(j-1)+4.5,nsec(j)/2)];
        x = [x linspace(dist(j-1)+4.5+7.5/nsec(j)*2,dist(j),nsec(j)/2)];
        AIP = length(x);
    case 3
        s = s + 1.32;
        dist(j) = s;
        order(j,1) = ord(j);
        nsec(j) = 1;
        probe = length(x);
        x = [x dist(j)];
    case 4
        s = s + 8.0;
        dist(j) = s;
        order(j,1) = ord(j);
        nsec(j) = 2;
        probe = length(x);
        x = [x dist(j-1)+4.0 dist(j)];
    case 5
        s = s + 5.0;
        dist(j) = s;
        order(j,1) = ord(j);
        nsec(j) = 2;
        actuator = length(x) + 1;
        x = [x dist(j-1)+2.5 dist(j)];
    end
end
dist = dist/39.4;        % Convert from inches to meters
x = x/39.4;
```

REFERENCES

[1] Nelson, P.A. and Elliot, S.J. *Active Control of Sound*. Academic Press, San Diego, CA, 1992.

[2] Saad, M.A. *Compressible Fluid Flow*. Prentice-Hall Inc., Englewood Cliffs, New Jersey 1985.

[3] Dowling, A.P. *Sound and Sources of Sound*. Halsted Press: Jon Wiley and Sons, New York, NY, 1983.

[4] Berndt, R.G. *Actuation for Rotating Stall Control of High Speed Axial Compressors*. Ph.D. Thesis, Massachusetts Institute of Technology, 1995.

[5] Paduano, J.D. *Active Control of Rotating Stall Axial Compressors*. Ph.D. Thesis, Massachusetts Institute of Technology, 1991.

[6] Spakovszky, Z.S. *Active Control of Rotating Stall in a Transonic Compressor Stage with Inlet Distortion*. S.M. Thesis, Massachusetts Institute of Technology, 1999.

[7] Paduano, J.D., 2000-2001. Personal Communications.

[8] Guenette, G.R., 2000-2001. Personal Communications.

[9] Brear, M., 2001. Personal Communications.

[10] Weigl, H.J. *Active Stabilization of Rotating Stall and Surge in a Transonic Single Stage Axial Compressor*. Ph.D. Thesis, Massachusetts Institute of Technology, 1997.

[11] Belanger, P.R. *Control Engineering: A Modern Approach*. Saunders College Publishing. Philadelphia, PA. 1995.

[12] SAE Committee S-16. *ARP-1420: Gas Turbine Engine Inlet Flow Distortion Guidelines*. 1977.

[13] Gordon, B.W. "Dynamic Modeling of an Axi-Centrifugal Helicopter Inlet".

[14] Nelson, E.B., Paduano, J.D. and Epstein, A.H. "Active Stabilization of Surge in an Axi-Centrifugal Turboshaft Engine". ASME. 1999.

[15] MacMartin, D., 2001. Personal Communications.

[16] Longley, J.P. "A Review of Non-Steady Flow Models for Compressor Stability." ASME. 1993.

[17] Kalamuck, K.M. *A Theory for the Performance of Hot-film Shear Stress Probes*. Ph.D. Thesis, Massachusetts Institute of technology, 1983.

[18] Tao of Systems Integration, Inc. "Multi-Element Surface Hot-Film Sensors: General Information and Catalog", 2000.

[19] Sievers, L.A. and Von Flotow, A.H. "Comparison and Extensions of Methods for Cancellation of Periodic Noise", *IEEE Transactions on Signal Processing*, vol. ASSP-40, no. 10, Oct. 1992.

[20] Forsythe, W. and Goodall, R.M. *Digital Control*. McGraw-Hill Inc., New York, 1991.

[21] SAE Committee S-16. *AIR-1419: Inlet Total-Pressure-Distortion Considerations for Gas-Turbine Engines*. 1983.

[22] Paduano, J.D. "Using Matlab to Study Time-Delay Approximations". *Lecture Notes from MIT Course 16.357*, 1998.

[23] Kwong, A.H.M. and Dowling, A.P. "Active Boundary-Layer Control in Diffusers". *AIAA Journal*. Vol. 32, Dec. 1994.

[24] Paduano, J.D. "1-D Distributed Systems – Modeling for Control", *Lecture Notes*.

[25] Cho, D.L. "Active Control of Engine Inlet Separation". *Internal Report, MIT Department of Aeronautics and Astronautics*, 1992.

[26] Hamstra, J.W., Miller, D.N, Traux, P.P., Anderson, B.A. and Wendt, B.J. "Active Inlet Flow Control Technology Demonstration". 22nd International Congress of the Aeronautical Sciences: *ICAS-2000-6.11.2*, 2000.

[27] Gad-el-Hak, M. and Bushnell, D.M. "Separation Control: Review". *Journal of Fluids Engineering*. Vol. 113, 2000.

[28] McCormick, D.C. "Boundary Layer Separation Control with Directed Synthetic Jets". *American Institute of Aeronautics and Astronautics: AIAA 2000-0519*. 1999.

[29] Verma, A., 2001. Personal Communications.